Black silicon based materials for photoelectrochemical nitrogen reduction

Muataz Al-Agele

معتز عدنان علي

School of chemistry Faculty of science

Monash University

Clayton Victoria

Australia

Mayyadah, Aiman and Rami …thank you

Muataz Al-Agele, MSc, BSc.

Black silicon based materials for photoelectrochemical nitrogen reduction

A thesis submitted to fulfil the requirements of the degree Doctor of Philosophy,

Research Supervisors: Prof. Douglas R MacFarlane

Dr. Xinyi Zhang

Green Chemical Futures, 13 Rainforest Walk, Monash University Clayton, Melbourne VIC 3800 Australia

Copyright notice

Declaration

In accordance with Monash University thesis Regulations 17. Doctor of Philosophy, the following declarations are made: This thesis contains no material which has been accepted for the award of any other degree or diploma at any university or equivalent institution and that, to the best of my knowledge and belief, this thesis contains no material previously published or written by another person, except where due reference is made in the text of the thesis.

Publications during enrolment, first Author

Ali, M., et al., Nanostructured photoelectrochemical solar cell for nitrogen reduction using plasmon-enhanced black silicon. Nat Commun, 2016. 7.

Publications during enrolment as secondary author

- Zhou, F., et al., Electro-synthesis of ammonia from nitrogen at ambient temperature and pressure in ionic liquids. Energy & Environmental Science, 2017. 10(12): p. 2516-2520.
- Li, H., et al., Sulfated Carbon Quantum Dots as Efficient Visible ‐ Light Switchable Acid Catalysts for Room ‐ Temperature Ring ‐ Opening Reactions. Angewandte Chemie International Edition, 2015. 54(29): p. 8420-8424.
- Zhang, X., et al., UV/ozone-assisted low temperature preparation of mesoporous TiO 2 with tunable phase composition and enhanced solar light photocatalytic activity. Journal of Materials Chemistry A, 2014. 2(44): p. 18791-18795.

Thesis including published works, General Declaration

This thesis includes original paper published in peer reviewed journal. The core theme of the thesis is photoelectrochemical nitrogen reduction on silicon based materials. The ideas, development, and writing up of the paper in the thesis were the principal responsibility of myself, the candidate, working within the School of Chemistry, Faculty of Science, Monash University, under the supervision of Prof. Douglas Robert MacFarlane and Dr. Xinyi Zhang.

The inclusion of co-authors reflects the fact that the work came from active collaboration between researchers and acknowledges input into team-based research. In chapter three my contribution to the work involved the following:

Thesis Chapter	**Publication Title**	**Status**	**Nature and % of student contribution**	**Co-author name(s) Nature and % of Co-author's contribution**	Co-authors**, Monash student**
3	Nanostructured photoelectrochemical solar cell for nitrogen reduction using plasmon-enhanced black silicon	*published*	*85%.* designed, and performed the experiments, interpretation of data, prepared the manuscript	Fengling Zhou, help with quantum efficiency exp. 2%	*NO*
				Kun Chen and Laure Bourgeois, help with electronic microscopic analysis 2%	*Yes, No*
				Christopher Kotzur, help in high pressure experiment 2%	*Yes*
				Changlong Xiao, help with data 2%	*yes*
				Xinyi Zhang, and Douglas R. MacFarlane, help in design, interpretation of data, and preparing the manuscript 7%	*No*

I have / have not renumbered sections of submitted or published papers in order to generate a consistent presentation within the thesis.

Student name: Muataz Al-Agele

Student signature: **Date:**

I hereby certify that the above declaration correctly reflects the nature and extent of the student's and co-authors' contributions to this work. In instances where I am not the responsible author I have consulted with the responsible author to agree on the respective contributions of the authors.

Main Supervisor name: Douglas R. MacFarlane

Main Supervisor signature: **Date:**

ACKNOWLEDGEMENTS

Most enormous gratitude is for my devoted supervisor, Prof. Douglas R MacFarlane, for the efficient and generous support throughout this journey. I feel nothing less than grateful for a great deal of patience and academic advice. I especially appreciate all the show up talking that put everything back on the track whenever I felt lost. It has been a great professional learning experience, and I am truly inspired.

I would also like to thank Dr. Xinyi Zhang, for valuable support, I learned a great deal of perseverance and continuous hard work spirit form you. Special thanks to Dr. Gary Annat, Peter Newman, Dr. Haitao Lee, Dr. Fengling Zhou, Christopher Kotzur, Dr. Kun Chen, Dr. Changlong Xiao and a lot of you whom I couldn't mention you all, who have been great support and friendship all along.

My love and ultimate gratitude go to my family; Mayyadah, Aiman, Rami, mother and father for being that strong, and pushing me through in the hard times. I am indebted to you all; those occasions that I couldn't be the husband, father, or son, you all deserved. You all were a key contributor in making this achievement possible, thank you all. I Love you all.

I would also like to give my best thanks to all my friends, especially Dr. Mustafa Abdulla, your company and immense support have made the difference, and a smile in difficult times. Those who have been there when needed, have been patient and inspired me all along.

Most importantly, I am grateful for the patience that God has empowered my family with and me. For the light at the end of the tunnel, for the knowledge, thank God.

Muataz Al-Agele

ABSTACT

Global warming is a direct threat to all sorts of life on the planet, caused by the continued increase in greenhouse gas emissions since the beginning of the industrial age. Industrial ammonia production is responsible for a considerable amount of greenhouse gas emissions because it mainly adopts fossil fuel especially natural gas as an energy source.

This work is an endeavour to employ photocatalytic reaction to mimic the natural synthesis of ammonia, adopting only sunlight, water and nitrogen as reactants. Silicon as the semiconductor has been converted by dry-etching to black silicon (bSi) to escalate its abilities to absorb sunlight, and later decorated with gold nanoparticles (GNP) to enable a gold plasmonic effect. This produces a structure capable of carrying out dinitrogen photo-reduction to ammonia. This approach to preparing a decorated b-Si device and its capabilities are described In chapter two. An initial characterisation of the device involved a series of tests of rhodamine B degradation. The etched samples were superior compared to the reflective ones, and the performance of the gold-coated specimens was significantly improved compared to the un-coated. The results were related to the plasmonic effect and the substantial increase in light absorption in bSi compared to flat (reflective) silicon.

In chapter three, a specialised cell has been built to reduce nitrogen to ammonia. The working bSi+GNP device was back coated with Cr(III) as a sacrificial reductant. The cell achieved a remarkable production rate of 13.3 mg m^{-2} h^{-1}, at 2 suns illumination. Nitrogen diffusion in the electrolyte, is proved to be a limiting factor for the process; increasing pressure has a direct impact on the production rate up to 6 bar. Studying quantum efficiency

of the process using 50-nm-wide bandpass filters show a notable spike at 500 nm, which suggests that excitation of surface plasmons in the GNP particles provides an additional photo-excitation mechanism that contributes to the overall yield in this region of the spectrum. This chapter was published in *Nature Communications* in 2016.

In chapter four, optimisation of the working prototype was achieved by varying the wafer thickness, wafer conductivity, GNP coating thickness, pH and temperature. A specially designed incubator was built to minimise the effect of ambient temperature and light on the overall efficiency.

In chapter five, a catalyst study is described, introducing Ru (III) and Fe (III) as catalysts to the device, employing three methods to attach Ru (III) to the semiconductor surface: drop-casting, electroless deposition, and solution dispersion. Yields in the sample GNP/bSi/Cr/Ru with dispersed Ru (III) in electrolyte were almost double that of GNP/bSi/Cr showing a significant ability of Ru in catalysing the NRR. Further analysis showed the Ru(III) ability to form complexes with the generated ammonia increases the total ammonia yield. The thesis concludes with a Summary and Further Work in Chapter six.

TABLE OF CONTENTS

Chapter six: conclusions and future work

LIST OF FIGURES

Chapter three

Chapter Four

Chapter five

LIST OF ABBREVIATIONS

bSi	black silicon
GNP/bsi	Black silicon with gold coating
GNP/bSi/Cr	Black silicon with gold coating and chromium on the back
GNP/bSi/Cr/Ru	Black silicon with gold coating and chromium on the back+ electroless deposited Ru
NP	nanoparticles
GNP	gold nanoparticles
e^-,h^+	Electron hole pair
VB	Valence band
CB	conductive band
hv	light
Δ G	Gibbs energy

N_2^{-} (aq)	solvated nitrogen anions
NRR	nitrogen reduction reaction
OVs	oxygen vacancies
NVs	nitrogen vacancies
SVs	sulfur vacancies
LDH	layered double hydroxide
-qE	electrochemical potential
E°	Nernst potential
A/ D^{-}	redox couple, A: acceptor D^{-}:donor
E_f	Fermi level potential
E_{fe}	Fermi level potential(electron)
E_{fh}	Fermi level potential (hole)
$q\Phi_b$	the barrier height; energy extracted from separated electron/hole pair at the junction.
PCE	power conversion efficiency
SPR	Surface Plasmon Resonance
λ	Wavelength
α	polarizability of the particle
ε	permittivity of the metal
RIE	reactive ion etching
ICP	inductively coupled plasma
ICP-RIE	inductively coupled plasma reactive ion etching
RF	radio frequency
PIII	plasma immersion ion implantation

Pulsed-PIII	pulsed-plasma doping
J_{sc}	Current density
MACE	metal-assisted chemical etching
IQE	internal quantum efficiency
sccm	a measure of gas throughput (pressure times volume over time)
RB	Rhodamine B
NHE	standard hydrogen electrode
ISE	Ion selective electrode
KBR	Kellog Brown and Root
KAAP	Kellogg Advanced Ammonia Process
HER	hydrogen evolution reaction

Chapter One

Introduction

1.1 Overview

Nitrogen reduction to ammonia is an energy-intensive process; it consumes about ~5% of the world natural gas and about 1-2% of the world's annual energy supply [1]. The ever-increasing demand for ammonia justifies the need to find an alternative approach to its synthesis. The demand is expected to further expand with the growing need for alternative fuels replacing the current fossil fuels. Ammonia is considered a successful replacement due to its safety compared with hydrogen. Alternative, environmentally friendly production methods are vital to address global warming, due to the massive amounts of fuel consumption and CO_2 evolution from the current industrial Haber-Bosh process. Since the mid-1900 scientists have put a significant effort into finding an alternative approach to ammonia formation; some research went toward imitating nature by studying enzymes which are capable of reducing ammonia at ambient conditions, but the work struggled with the complexity of these enzymes.

Other approaches were directed towards electrochemical nitrogen reduction; these studies focused on finding suitable catalytic electrodes that can achieve 100% faradaic efficiency. There are many obstacles in this approach, mainly the competitive hydrogen evolution reaction and the durability of these electrodes and performance from this approach is still far from competitive with the traditional Haber Bosch process.

The photocatalytic approach is certainly an environmentally friendly approach to nitrogen reduction, given that it needs only sunlight as an energy source. The literature background in this field is detailed further in this chapter. The approach adopted in this thesis as detailed in Chapter 2 is to mimic natural energy systems in plants and enzymes by using black silicon (bSi) semiconductor layer to reduce nitrogen to ammonia photochemically at

ambient conditions, using molecular nitrogen, water and sunlight as the only reactants. The semiconductor is decorated with gold nanoparticles (GNP) to activate the plasmonic effect and back coated with Cr (III) as a sacrificial reductant. The impressive results from this structure are described in Chapter three. The working prototype was further optimised by testing different types of wafers, changing the pH, deposition times and reaction temperature as described in Chapter Four. A catalyst study was conducted in Chapter five on the working prototype, introducing Ru (III) and Fe (III) as a catalyst; the study confirmed the catalytic abilities of Ru (III) and its ability to form complexes with the generated ammonia, which eventually increases the total ammonia yield. The thesis concludes with a Summary and discussion of further work in Chapter six.

1.2 Global warming

All forms of life on the planet are paying a great cost for the intensive use of the current energy sources, mainly because of their environmental impact and also due to their lack of sustainability. Fossil fuels represent around 83% of the world's energy used in 2011, including coal, oil and gas. In fact, without fossil fuels, humankind would not have been able to develop industrially to achieve the lifestyles which we enjoy today.

The environmental impact of these types of energy supply is attributed to their chemical content and the way they are formed. Atmospheric carbon dioxide is absorbed by trees and stored in the form of carbon compounds[2]. After millions of years, many trees sank into the swampy ground and disappeared, taking the carbon they had absorbed with them forming coal. The same happened with the sea creatures which stored the carbon in their bodies and eventually after their death, their bodies became buried underground, and

under high pressure, they were transformed into oil and gas [3]. The environmental problem arises with their high carbon content as these are burned to obtain the energy used to move machines, generating electricity, or forming other agriculturally beneficial chemicals, releasing the carbon dioxide back into the atmosphere causing the greenhouse effect.

Naturally, carbon-dioxide, in addition to other gases like methane, nitrous oxide and ozone in the atmosphere from a blanket like a layer that absorbs energy and warms the atmosphere and the surface of the Earth[4]. This process maintains the earth's temperature allowing life to exist. The growing use of fossil fuels cases more gases to be released which increases the energy retention thereby affecting the planet climate.

The tangible effects of the excessive use of fossil fuel are apparent; according to the World Health Organization dangerous outdoor air pollution due to fossil fuel burning kills 4.2 million people a year globally. Also, hotter weather, rising sea levels, frequent extreme weather and ocean acidification are a direct result of global warming. The temperature has recorded unprecedented levels since 2013, in fact, the Bureau of Meteorology has added purple and magenta to the forecast map for heat waves up to 54°C. Low-lying islands and coastal cities are endangered because of the rising sea levels due to the melting of the glaciers and ice caps all over the world. Natural weather catastrophes like bushfires, cyclones, droughts and floods are more aggressive and frequent. Also and more importantly, most of the excess CO_2 in the atmosphere is absorbed by the oceans changing its acidity and affecting the sea life and the food chains of sea creatures [5, 6].

1.3 Renewable energy

This form of energy is from naturally replenishing sources, including solar and wind. In a report published in 2017 [7] various forms of renewable energy contributed about 19% to global energy consumption and about 25% to the generation of electricity in 2015 and 2016, respectively. Its share of global energy is predicted to grow to 24% by 2020 [8].

Historically, before the use of fossil fuels (coal), nearly all energy used was renewable, including traditional biomass used to fuel fires [9], and wind energy used to move ships over water [10]. Wind power was one of the earliest forms of renewable energy which has been vastly developed through history, from ships moving to windmill and eventually electricity generation through wind turbines [11]. Geothermal power is thermal energy generated and stored in the heat of the earth; it can be drawn by pumping cold water into the hot rocks and returning the heated vapour to the surface, which is used to drive electricity-generating steam turbines [12]. Hydropower uses the energy of moving water to move specially designed water turbines to generate electricity. It is the most developed renewable energy system, and it is used to provide electricity generation in more than 160 countries worldwide [13].

In 1885, Siemens discovered the photovoltaic effect in the solid state and commented "In conclusion, I would say that however great the scientific importance of this discovery may be, its practical value will be no less obvious when we reflect that the supply of solar energy is both without limit and without cost and that it will continue to pour down upon us for countless ages after all the coal deposits of the earth have been exhausted and forgotten"[14]. Solar energy is the most abundant permanent energy resource on earth; sun emits energy at a rate of 3.8×10^{23} kW per second, after reflecting a significant portion, and absorbing some of it by the planet atmosphere, about 60% of this amount reaches the surface of the earth. This

amount of energy is 7500 times the world's total annual primary energy consumption[8]. The known solar technologies are solar heating, photovoltaics, concentrated solar power, concentrator photovoltaics, solar architecture and artificial photosynthesis [15, 16]. These technologies are mainly identified as either passive solar or active solar depending on the way they capture, convert, and are transported. Passive techniques include designing spaces that naturally circulate air or building orientation toward the sun, while photovoltaics, artificial photosynthesis etc called active technologies.

Using a renewable energy source does not mean that automatically it is an entirely environmentally benign process; for example, the environmental impacts on wildlife from building hydro dams. Also, the impact of the manufacturing process for turbines used in the wind, geothermal, and hydropower areas. However, these resources make a much lighter environmental footprint than the widely used fossil fuels[17].

These types of renewable energy are produced using mechanical means, instead of by harnessing a natural process, the most popular form being bioenergy. Bioenergy is withdrawn from organic matter of recently living plant or animal origin to generate electricity and heat, or to produce liquid fuels such as ethanol and biodiesel for transportation [18].

1.4 The photocatalysis process

''Acceleration of a photo-induced reaction by the presence of a catalyst'' is a precise description of what is described as photocatalysis since light acts as a reactant rather than a catalyst [19]. When a semiconductor is illuminated with photons of energy (light) greater than or equal to the bandgap (bg) energy of the semiconductor, the result will be the production of hole and electron pairs (e^-,h^+), which react with available species to form ions (eq. 1).

A^+B^+ (e^-,h^+) → A^-+B^+ ….(On semiconductor surface when Light energy ⩾bg energy) (1)

In more detail, an (e^-,h^+) pair is formed when electromagnetic radiation excites an electron from the valence band (VB) to the conductive band (CB), leaving behind a positive hole (eq. 2)[20]. Following light exposure, (e^-, h^+) pairs created by the photo-process have two possible destinies; either they interact with adsorbate molecules leading to the generation of reduction and oxidation products (eq. 3, 4), or they re-recombine. The latter process is detrimental to the desired overall photocatalytic process [20].

hv + SC → e^- + h^+---------- (2)

A+ e^- → A^-_{ads} ---------- (3)

B+ h^+→ B^+_{ads}---------- (4)

Generally, semiconductor choice is crucial to support a particular reaction, depending on the position of the conduction band (CB) and valence bands (VB) of the photo-absorber concerning the redox potentials of the desired photochemical reaction. The chemical

potentials of the photo-generated (e^-, h^+) pairs depend on the position of the energy levels in the semiconductor. In titania, as an example, the energy levels of its CB and the top of the VB are -0.3 and 3.0 V, respectively, making it a mildly reducing and strongly oxidising material[21]. In the case of nitrogen reduction, the potentials of the reduced species are explained in figure 1-1 below, though a full explanation for the expected mechanism is explored later in this chapter.

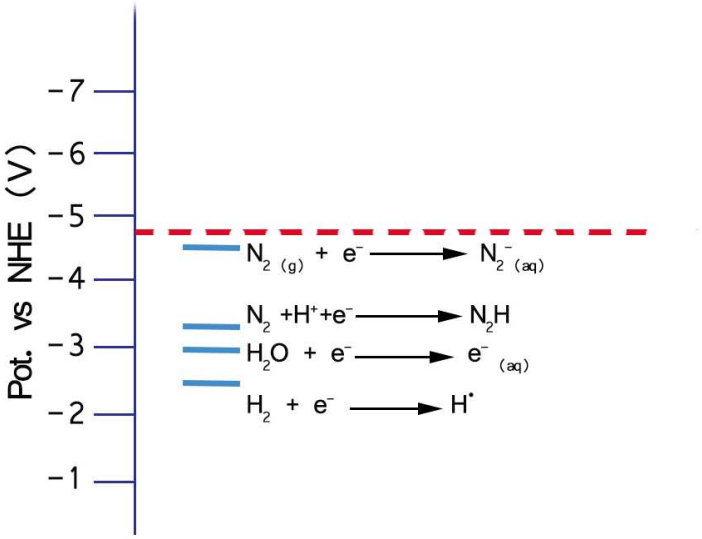

Figure 1-1: Schematic representation of the potentials of the reduced species in nitrogen reduction versus NHE, (reproduced from [22]).

The steps following absorption of solar radiation depending on the rates of charge carrier generation and their following transfer to various reacting species. The essential criteria that effect photocatalytic materials are the crystallographic phase, exposed crystal face, crystallite size, the presence of dopant materials, and lattice defects creating impurities and vacancies. External parameters include solution pH, temperature, the structure of

reactant and its initial concentration [20]. For example, titania as a photocatalyst has been widely used; its reaction kinetics are described in figure 1-2 below.

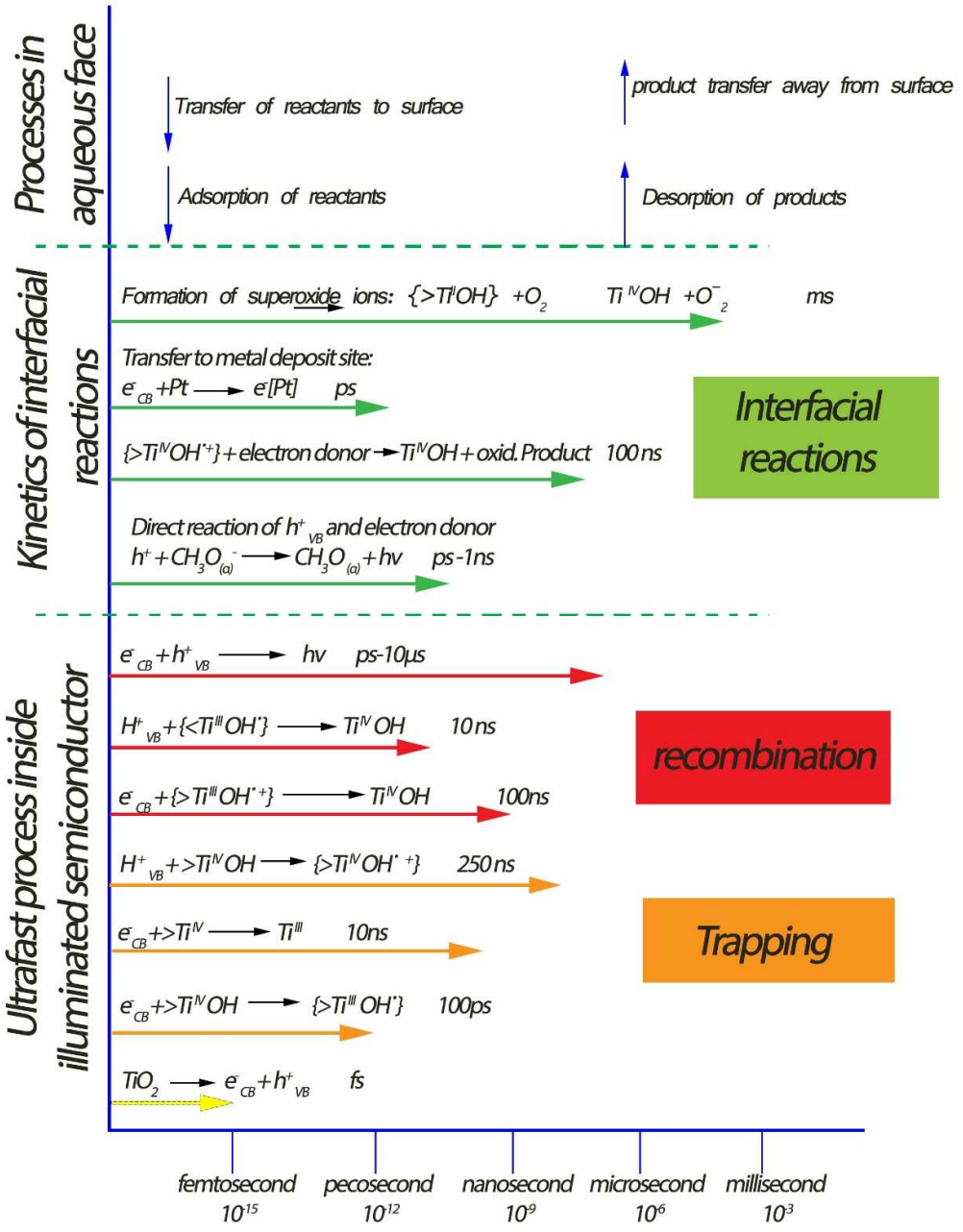

Figure 1-2: Schematic illustration TiO_2 photocatalysis elementary reactions with corresponding timescales (reproduced from ref. [23]).

Initial rates of photocatalysed reactions are directly proportional to the mass of catalyst used (how many active sites are present). However, the ability to increase the reaction rate by increasing the amount of photocatalyst reaches a plateau at a certain point as the rate determining parameter changes away from adsorption. This relationship is also attributed to the screening effect of the particles, ultimately causing a decrease in light penetration depth. Adsorption is typically deemed to be the factor that controls photocatalysis kinetics, particularly in the slurry type reaction systems where mass transfer limitations may be avoided through efficient stirring. Adsorption of species can effectively trap electrons and holes, improving the charge carrier separation process (relative to the recombination rate) and thereby increasing the photocatalytic efficiency. Recombination rates observed in photocatalysts are high, so interfacial charge carrier trapping must be rapid, and this may require the scavenger species to be pre-adsorbed on the surface [20].

1.5 Nitrogen reduction to ammonia

Ammonia synthesis from nitrogen and hydrogen has been of great importance to the modern world. The world's population growth from 1.6 billion people in 1900 to today's seven billion would not have been possible without ammonia synthesis [24]. It has played an essential role in the nutritional needs of organisms by serving as a basic part of food components and fertilizers [25], in addition to the production of other materials such as cleaning products and pharmaceuticals [26].

Synthesis of ammonia from nitrogen was discovered by Haber in 1913, replacing the old energy-consuming Birkeland–Eyde process to produce nitric acid [27]. This process was conducted in extreme conditions (high pressures and temperatures), at which, nitrogen reacts with hydrogen in the presence of iron [28]. Later, it was developed by Carl Bosch to produce Industrial quantities in a procedure called the Haber–Bosch process, for which he was awarded a Nobel Prize in 1931 [29] (detailed literature of industrial approach is described in chapter five).

It is challenging to reduce molecular nitrogen because it is stable and chemically inert [30]. Nonetheless, nitrogen can be reduced via a variety of different procedures [30, 31]. These procedures often require to severe conditions (e.g., the Haber−Bosch process) [32], relatively complex biological enzymes [33], or high energy consumption electrochemical procedures [34] (figure 1-3).

The reduction reaction (reduction of atomic nitrogen N_2 in water to form ammonia) requires an input of energy, $N_{2\,(g)} + 3H_2O_{\,(L)} \rightarrow 2NH_{3\,(g)} + 3/2O_{2(g)}$ $\Delta G = 678$ kJ mol^{-1}, were ΔG is the Gibbs energy stored in one mole of the ammonia [35]. Naturally, this process is

carried out by nitrogenase enzymes in azotobacter at room temperature and atmospheric pressure [36, 37].

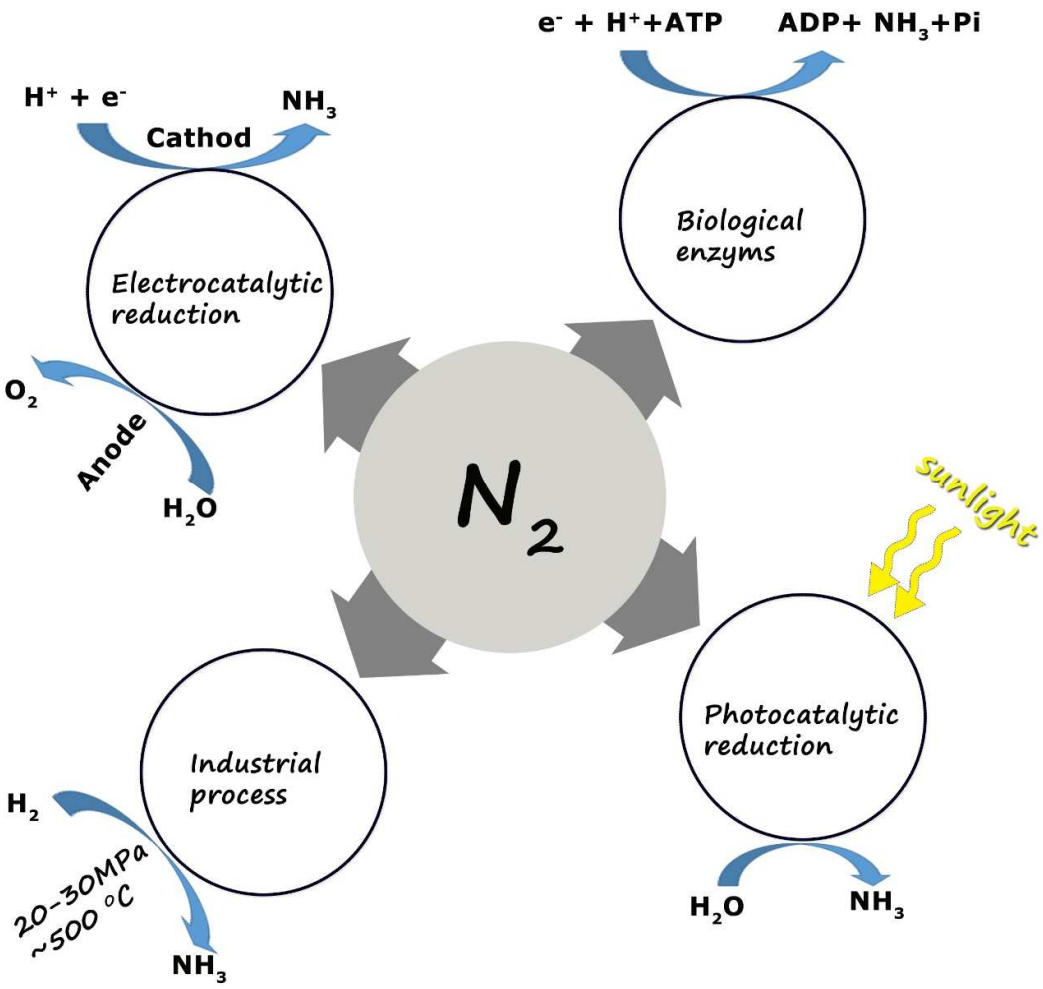

Figure 1-3: Schematic illustration of different reaction routes for nitrogen reduction to ammonia.

Therefore, molecular nitrogen fixation by hydrogen Inspired by the natural process to form ammonia at ambient temperature and pressure, is a very attractive area to research, especially, where these alternative pathways are CO_2-emission-free. The possibility of using

sunlight to provide a part of the required energy input to this reaction has stimulated efforts to use illuminated semiconductor materials as photoelectrodes.

The major barrier to N_2 reduction in aqueous media is the high energy associated with the formation of N_2H [30, 38]. There are several pathways to form N_2H from N_2 in water. Theoretical studies have expected that solvated nitrogen anions ($N_{2\ (aq)}^{-}$) could be formed in water, proposing the possibility of forming N_2H through $N_{2(aq)}^{-}$ and H^+; however, the reduction potential to form $N_{2(aq)}^{-}$ through (eq 5) is -4.2 V [39]; also, it is difficult to observe $N_{2(aq)}^{-}$ experimentally [22]

$$N_2 + e^- \rightarrow N_{2\ (aq)}^{-} \qquad E = -4.2V \qquad \text{----------5}$$

A two step reaction is more likely to happen; the first being $H^+ \rightarrow H^\cdot$, followed by the reaction of $H^\cdot$ with atomic nitrogen. The total reaction (eq8) has a more achievable reduction potential of -3.2 V versus NHE [38, 39]

$$H_2O + e^- \rightarrow e^-(aq) \qquad E^0 = -2.86\ V \qquad \text{----------6}$$

$$H^+ + e^- \rightarrow H^\cdot \qquad E = -2.3\ V \qquad \text{----------7}$$

$$N_2 + H^+ + e^- \rightarrow N_2H \qquad E = -3.2\ V \qquad \text{----------8}$$

Solvated electrons serve as an intermediate in this reaction, because atomic hydrogen formed through (eq7) [40] has a slightly higher potential than the potential to form ($e_{(aq)}^{-}$) (eq6) [41]. Thus, emission of electrons from b-Si into the water could produce a supply of solvated electrons; these electrons are capable of initiating high-energy reduction reactions of H^+ to $H^\cdot$ and the subsequent reduction reaction with N_2 to form N_2H and ultimately NH_3 [22]. Lately, Jeffrey et al. [42] have confirmed this mechanism by conducting a combination

of experimental and computational approaches is elucidate the detailed molecular-level mechanistic pathway from N_2 to NH_3.

Also, as understood from equations (6-8) the reduction of N_2 molecules needs a rather negative potential that the conduction band of most common semiconductors (TiO_2, g-C_3N_4, $SrTiO_3$, CdS and so on) cannot achieve, resulting in difficulty in solar driven nitrogen reduction reaction (NRR). Therefore, special semiconductor-based nanocatalysts with high efficiency and stability need to be developed to produce ammonia under mild conditions [43].

1.6 Photochemical nitrogen fixation

1.6.1 oxide-based photocatalysts

TiO_2 based photocatalysts were the earliest studies toward the photo-fixation of nitrogen, in 1977 Schrauzer and Guth [44] reported chemisorbed N_2 on the powder mixtures of rutile and anatase TiO_2 under UV irradiation along with trace amounts of N_2H_4. Their findings were that TiO_2 had a vital role in the reduction process, and doping with iron boosted the overall process. In 1988, Bourgeois et al. [45] disagreed with these findings, proposing that unmodified TiO_2 exhibited photocatalytic NRR activity after annealing at high temperature in air, which manipulated the doped impurities states in the bandgap of semiconductor and the surface hydroxyl groups [43].

The Bourgeois [45] hypothesis was further supported by later research published by Radford and Francis [46], who confirm the inability of TiO_2 to produce ammonia without doping. The hypothesis rationalised this proposal that doped Fe^{3+} ions could trap the electrons and thus decrease the recombination rate of (e^-,h^+) pairs. The same theory was later

confirmed by Zhao et al. in 2014, with optimal Fe^{3+} doping resulting in higher quantum yield for NRR using ethanol as a scavenger [43].

In 2002, Antonelli et al. [47] used a reduced mesoporous titanium oxide photocatalyst to photo-reduce nitrogen; the study attributed the yield collected to the assisted N_2 triple bond cleavage by the low-valence Ti centres. In 2017 Hirakawa et al. [48], suggested a different mechanism proposing that the Ti^{3+} species on the oxygen vacancies (OVs) were the active sites for NRR. Nitrogen adsorbed on Ti^{3+} sites and nitrogen triple bonds (N≡N) were activated, forming Ti^{4+}-azo species. Subsequently, electrons in the CB were trapped in the surface OVs and regenerated on the Ti^{3+} sites. These produce Ti^{4+}-hydrazo species; then, the NH_3 molecules were generated, with the re-formation of surface active sites under irradiation. Working in tandem, Au nanocrystals anchored on TiO_2 nanosheets were used to reduce N_2. In the beginning, N_2 molecules were chemisorbed and activated by the OVs on TiO_2, and NH_3 is formed from the OVs-activated N_2 molecules by the trapped hot electrons [43, 48, 49].

Doping TiO_2 with different metal species was a relatively unsuccessful photocatalytic approach because of the co-catalyst ability of the loaded transition metal atoms [43, 50-52]. Also, Schottky junctions are formed at the interface between semiconductors and transition metal nanoparticles, in which built-in electric fields promote the separation of (e^-, H^+) pairs[53, 54]. Based on this principle, Rao et al. sorted the photocatalytic nitrogen fixation activity of metals loaded onto TiO_2 as Ru > Fe > Os [55]. Viswanathan et al. [56] obtained the order as Ru > Rh > Pd > Pt and correlated it with the strength of intermediary M–H bonds. Other than TiO_2, there were many attempts to use different oxides to reduce the atomic nitrogen, like carbon-$WO_3 \cdot H_2O$ hybrids in pure water, where carbon played a remarkable role in activating N_2 molecules and accelerating the separation and transport of the photocarriers [57]. Also,

BiO quantum dots efficiently generate ammonia in the absence of sacrificial reagent or co-catalyst, the low valence state Bi (II) species were conducive to N_2 activation by temperature programmed desorption experiments and DFT calculations [58].

1.6.2 Oxyhalide based photocatalysts

In 2015, Zhang et al. proposed an efficient NRR on BiOBr nanosheets by introducing OVs into the exposed (001) facets. The theoretical simulation indicates that N_2 is activated by the OVs. The bond length of the adsorbed N_2 on OVs elongates to 1.133 Å, which is longer than the bond length of the original N≡N (1.078 Å). The hypothesis is that the OV trapped electrons could jump into the empty antibonding orbitals of activated N_2 molecules and ease the bond breakage [59]. In 2017, Wang et al. [60] used ultrafine Bi_5O_7Br nanotubes with sufficient and sustainable oxygen vacancies to reduce nitrogen without any sacrificial reagents or co-catalysts. Also, Bi_5O_7I nanosheets with dominant exposed {001} and {100} facets used in photocatalytic NRR, the results showed that Bi_5O_7I-001 exhibit a higher photocatalytic NH_3 production rate compared to Bi_5O_7I-100.

1.6.3 Graphitic nitride carbon (g-C3N4) based photocatalysts

These compounds have been studied heavily in other reactions like water splitting, CO_2 reduction and organic synthesis due to their unique characteristics including low-cost and stable photocatalyst performance [61].

Dong et al. [62] introduced nitrogen vacancies (NVs), proposing their responsibility for improved NRR, because of their shape and size, as the nitrogen atoms can absorb and activate the chemically inert N_2. In addition to their ability to trap the photo-excited electrons, which promote the separation of electrons and holes. The success of the approach induced

researching of different kinds of g-C_3N_4 based photocatalysts in photochemical ammonia synthesis [63-67].

1.6.4 Transition-metal sulphides and other photocatalysts

Metal sulphides have suffered severe photo-corrosion whenever used in the photocatalytic NRR since CdS was used in 1980, with a few breakthroughs [68]. In 2017, $Cd_{0.5}Zn_{0.5}S$ loaded with Ni_2P, which acted as a co-catalyst, promoted the transfer of photo-induced electrons, and holes resulting in ammonia production with a quantum efficiency of 4.32% at 420 nm [69]. Wang et al. used ultrathin MoS_2 nanosheets to synthesis ammonia with a synthesis rate of 325 μmol·gcat.$^{-1}$·h^{-1}, and compared it with bulk MoS_2 which had no activity in ammonia synthesis. The study proposed that the ultrathin MoS2 nanosheets generate light-induced trions with a high concentration of electrons [43, 70]. Hu et al. used the OVs and NVs concept to demonstrate that sulfur vacancies (SVs) in $Zn_{0.1}Sn_{0.1}Cd_{0.8}S$ and $Mo_{0.1}Ni_{0.1}Cd_{0.8}S$ could also induce the photo-conversion of N_2 to NH_3, with the same hypothesis that SVs acted as electron nets, which prevented the electron-hole recombination [71, 72]. Zhang et al. reported the use of CuCr-LDH (LDH is layered double hydroxide) ultrathin nanosheets producing relatively good results. The study regarded the yields to the compressive strain and distorted structure of the LDH originating from the abundant oxygen defects, which greatly boosted the N_2 chemisorption and activation [73].

1.7 References

1. Michalsky, R., et al., *Solar thermochemical production of ammonia from water, air and sunlight: Thermodynamic and economic analyses.* Energy, 2012. **42**(1): p. 251-260.
2. Dioxide, A.C., *the Global Carbon Cycle.* Department of Energy ER-0239, Washing, 1985.
3. Quigley, T. and A. Mackenzie, *The temperatures of oil and gas formation in the sub-surface.* Nature, 1988. **333**(6173): p. 549.
4. Khalil, M., *Non-CO2 greenhouse gases in the atmosphere.* Annual Review of Energy and the Environment, 1999. **24**(1): p. 645-661.
5. Weissburg, M. and A.M. Draper, *Impacts of Global Warming and Elevated CO2 on Sensory Behavior in Predator-Prey Interactions: A Review and Synthesis.* Frontiers in Ecology and Evolution, 2019. **7**: p. 72.
6. De Cian, E. and I.S. Wing, *Global energy consumption in a warming climate.* Environmental and resource economics, 2019. **72**(2): p. 365-410.
7. Sawin, J., *Renewable energy policy network for the 21st century renewables 2017 global status report.* REN21 Secretariat: Paris, France, 2017: p. 1-302.
8. Grathwohl, M., *World Energy Supply: Resources-Technologies-Perspectives*. 2018: Walter de Gruyter GmbH & Co KG.
9. Citossi, M. and M. Cobal, *A PRELIMINARY STUDY TO PRODUCE SOLAR CARBON.* 2018.
10. Darling, D., *The Encyclopedia of Alternative Energy and Sustainable Living. Retrieved 31 March 2011*. 2011.
11. Patel, M.R., *Wind and solar power systems: design, analysis, and operation*. 2005: CRC press.

12. Boyle, G., *Renewable energy.* Renewable Energy, by Edited by Godfrey Boyle, pp. 456. Oxford University Press, May 2004. ISBN-10: 0199261784. ISBN-13: 9780199261789, 2004: p. 456.

13. Grumbine, R.E. and J. Xu, *Mekong hydropower development.* Science, 2011. **332**(6026): p. 178-179.

14. Siemens, W., *On the electromotive action of illuminated selenium, discovered by Mr. Fritts, of New York.* Van Nostrand's Engineering Magazine (1879-1886), 1885. **32**(118): p. 514.

15. Nelson, V.C., *Introduction to renewable energy*. 2011: CRC press.

16. Faunce, T., et al., *Artificial photosynthesis as a frontier technology for energy sustainability.* Energy & Environmental Science, 2013. **6**(4): p. 1074-1076.

17. Outka, U., *The renewable energy footprint.* Stan. Envtl. LJ, 2011. **30**: p. 241.

18. Fischer, G. and L. Schrattenholzer, *Global bioenergy potentials through 2050.* Biomass and bioenergy, 2001. **20**(3): p. 151-159.

19. Mills, A. and S. Le Hunte, *An overview of semiconductor photocatalysis.* Journal of photochemistry and photobiology A: Chemistry, 1997. **108**(1): p. 1-35.

20. Shand, M. and J.A. Anderson, *Aqueous phase photocatalytic nitrate destruction using titania based materials: routes to enhanced performance and prospects for visible light activation.* Catalysis Science & Technology, 2013. **3**(4): p. 879-899.

21. Fujishima, A., et al., *Titanium dioxide photocatalyst*. 2002, Google Patents.

22. Zhu, D., et al., *Photo-illuminated diamond as a solid-state source of solvated electrons in water for nitrogen reduction.* Nat Mater, 2013. **12**(9): p. 836-841.

23. Friedmann, D., C. Mendive, and D. Bahnemann, *TiO< sub> 2</sub> for water treatment: Parameters affecting the kinetics and mechanisms of photocatalysis.* Applied Catalysis B: Environmental, 2010. **99**(3): p. 398-406.

24. Smil, V., *Enriching the earth: Fritz Haber, Carl Bosch, and the transformation of world food*. 2001, The MIT Press, Cambridge, United Kingdom.

25. *Ammonia*. 2014; Available from: http://en.wikipedia.org/wiki/Ammonia.

26. Erisman, J.W., et al., *How a century of ammonia synthesis changed the world.* Nature Geoscience, 2008. **1**(10): p. 636-639.

27. Ihde, A.J., *The development of modern chemistry*. 1970: Courier Dover Publications.

28. Bauer, K., D. Garbe, and H. Surburg, *Ullmann's encyclopedia of industrial chemistry.* Ullmann's Encyclopedia of Industrial Chemistry, 1988. **11**.

29. Waite, A.E., *The Hermetic and Alchemical Writings of Aureolus Philippus Theophrastus Bombast, of Hohenheim, Called Paracelsus the Great*. Vol. 1. 1967: University Books.

30. Bazhenova, T. and A. Shilov, *Nitrogen fixation in solution.* Coordination chemistry reviews, 1995. **144**: p. 69-145.

31. Benson, E.E., et al., *Electrocatalytic and homogeneous approaches to conversion of CO 2 to liquid fuels.* Chemical Society Reviews, 2009. **38**(1): p. 89-99.

32. Ozaki, A., et al., *A Treatise on Dinitrogen Fixation.* Wiley, New York, 1979: p. 169.

33. Eady, R.R., *Structure-function relationships of alternative nitrogenases.* Chemical reviews, 1996. **96**(7): p. 3013-3030.

34. Murakami, T., et al., *Electrolytic synthesis of ammonia in molten salts under atmospheric pressure.* Journal of the American Chemical Society, 2003. **125**(2): p. 334-335.

35. Grayer, S. and M. Halmann, *Electrochemical and photoelectrochemical reduction of molecular nitrogen to ammonia.* Journal of electroanalytical chemistry and interfacial electrochemistry, 1984. **170**(1): p. 363-368.

36. Rees, D.C., et al., *Structural basis of biological nitrogen fixation.* Philosophical Transactions of the Royal Society A: Mathematical, Physical and Engineering Sciences, 2005. **363**(1829): p. 971-984.

37. Howard, J.B. and D.C. Rees, *Structural basis of biological nitrogen fixation.* Chemical reviews, 1996. **96**(7): p. 2965-2982.

38. Shilov, A., *Catalytic reduction of molecular nitrogen in solutions.* Russian chemical bulletin, 2003. **52**(12): p. 2555-2562.

39. Bauer, N., *THEORETICAL PATHWAYS FOR THE REDUCTION OF N2 MOLECULES IN AQUEOUS MEDIA: THERMODYNAMICS OF N2Hn1.* The Journal of Physical Chemistry, 1960. **64**(7): p. 833-837.

40. Roduner, E., *Hydrophobic solvation, quantum nature, and diffusion of atomic hydrogen in liquid water.* Radiation Physics and Chemistry, 2005. **72**(2): p. 201-206.

41. Alpatova, N.M., L.I. Krishtalik, and Y.V. Pleskov, *Electrochemistry of solvated electrons*, in *Organolithium Compounds/Solvated Electrons*. 1987, Springer. p. 149-219.

42. Christianson, J.R., et al., *Mechanism of N2 Reduction to NH3 by Aqueous Solvated Electrons.* The Journal of Physical Chemistry B, 2013. **118**(1): p. 195-203.

43. Xue, X., et al., *Review on photocatalytic and electrocatalytic artificial nitrogen fixation for ammonia synthesis at mild conditions: Advances, challenges and perspectives.* Nano Research: p. 1-21.

44. Schrauzer, G. and T. Guth, *Photocatalytic reactions. 1. Photolysis of water and photoreduction of nitrogen on titanium dioxide.* Journal of the American Chemical Society, 1977. **99**(22): p. 7189-7193.

45. Bourgeois, S., D. Diakite, and M. Perdereau, *A study of TiO2 powders as a support for the photochemical synthesis of ammonia.* Reactivity of solids, 1988. **6**(1): p. 95-104.

46. Radford, P.P. and C.G. Francis, *Photoreduction of nitrogen by metal doped titanium dioxide powders: a novel use for metal vapour techniques.* Journal of the Chemical Society, Chemical Communications, 1983(24): p. 1520-1521.

47. Vettraino, M., et al., *Room-temperature ammonia formation from dinitrogen on a reduced mesoporous titanium oxide surface with metallic properties.* Journal of the American Chemical Society, 2002. **124**(32): p. 9567-9573.

48. Hirakawa, H., et al., *Photocatalytic conversion of nitrogen to ammonia with water on surface oxygen vacancies of titanium dioxide.* Journal of the American Chemical Society, 2017. **139**(31): p. 10929-10936.

49. Yang, J., et al., *High-efficiency "working-in-tandem" nitrogen photofixation achieved by assembling plasmonic gold nanocrystals on ultrathin titania nanosheets.* Journal of the American Chemical Society, 2018. **140**(27): p. 8497-8508.

50. Schrauzer, G. and T. Guth, *Photolysis of water and photoreduction of nitrogen on titanium dioxide.* Journal of the American Chemical Society, 2002. **99**(22): p. 7189-7193.

51. Rusina, O., et al., *Nitrogen photofixation at nanostructured iron titanate films.* Angewandte Chemie International Edition, 2001. **40**(21): p. 3993-3995.

52. Ileperuma, O., K. Tennakone, and W. Dissanayake, *Photocatalytic behaviour of metal doped titanium dioxide: Studies on the photochemical synthesis of ammonia on Mg/TiO2 catalyst systems.* Applied Catalysis, 1990. **62**(1): p. L1-L5.

53. Kubacka, A., M. Fernández-García, and G. Colón, *Advanced Nanoarchitectures for Solar Photocatalytic Applications.* Chemical Reviews, 2012. **112**(3): p. 1555-1614.

54. Qu, Y. and X. Duan, *Progress, challenge and perspective of heterogeneous photocatalysts.* Chemical Society Reviews, 2013. **42**(7): p. 2568-2580.

55. Rao, N., S. Dube, and P. Natarajan, *Photocatalytic reduction of nitrogen over (Fe, Ru or Os)/TiO2 catalysts.* Applied Catalysis B: Environmental, 1994. **5**(1-2): p. 33-42.

56. Ranjit, K.T., T.K. Varadarajan, and B. Viswanathan, *Photocatalytic reduction of dinitrogen to ammonia over noble-metal-loaded TiO2.* Journal of Photochemistry and Photobiology A: Chemistry, 1996. **96**(1): p. 181-185.

57. Li, X., et al., *Efficient Solar-Driven Nitrogen Fixation over Carbon–Tungstic-Acid Hybrids.* Chemistry – A European Journal, 2016. **22**(39): p. 13819-13822.

58. Sun, S., et al., *Efficient photocatalytic reduction of dinitrogen to ammonia on bismuth monoxide quantum dots.* Journal of Materials Chemistry A, 2017. **5**(1): p. 201-209.

59. Li, H., et al., *Efficient Visible Light Nitrogen Fixation with BiOBr Nanosheets of Oxygen Vacancies on the Exposed {001} Facets.* Journal of the American Chemical Society, 2015.

60. Wang, S., et al., *Light-Switchable Oxygen Vacancies in Ultrafine Bi5O7Br Nanotubes for Boosting Solar-Driven Nitrogen Fixation in Pure Water.* Advanced Materials, 2017. **29**(31): p. 1701774.

61. Ong, W.-J., et al., *Graphitic Carbon Nitride (g-C3N4)-Based Photocatalysts for Artificial Photosynthesis and Environmental Remediation: Are We a Step Closer To Achieving Sustainability?* Chemical Reviews, 2016. **116**(12): p. 7159-7329.

62. Dong, G., W. Ho, and C. Wang, *Selective photocatalytic N2 fixation dependent on g-C3N4 induced by nitrogen vacancies.* Journal of Materials Chemistry A, 2015. **3**(46): p. 23435-23441.

63. Wu, G., Y. Gao, and B. Zheng, *Template-free method for synthesizing sponge-like graphitic carbon nitride with a large surface area and outstanding nitrogen photofixation ability induced by nitrogen vacancies.* Ceramics International, 2016. **42**(6): p. 6985-6992.

64. Ma, H., et al., *Large-scale production of graphitic carbon nitride with outstanding nitrogen photofixation ability via a convenient microwave treatment.* Applied Surface Science, 2016. **379**: p. 309-315.

65. Ma, H., et al., *Preparation of graphitic carbon nitride with large specific surface area and outstanding N2 photofixation ability via a dissolve-regrowth process.* Journal of Physics and Chemistry of Solids, 2016. **99**: p. 51-58.

66. Hu, S., et al., *Fe3+ doping promoted N2 photofixation ability of honeycombed graphitic carbon nitride: The experimental and density functional theory simulation analysis.* Applied Catalysis B: Environmental, 2017. **201**: p. 58-69.

67. Li, X., et al., *Efficient photocatalytic fixation of N2 by KOH-treated g-C3N4.* Journal of Materials Chemistry A, 2018. **6**(7): p. 3005-3011.

68. Liu, Q., L. Ai, and J. Jiang, *MXene-derived TiO2@C/g-C3N4 heterojunctions for highly efficient nitrogen photofixation.* Journal of Materials Chemistry A, 2018. **6**(9): p. 4102-4110.

69. Ye, L., et al., *Ni2P loading on Cd0.5Zn0.5S solid solution for exceptional photocatalytic nitrogen fixation under visible light.* Chemical Engineering Journal, 2017. **307**: p. 311-318.

70. Sun, S., et al., *Photocatalytic robust solar energy reduction of dinitrogen to ammonia on ultrathin MoS2.* Applied Catalysis B: Environmental, 2017. **200**: p. 323-329.

71. Cao, Y., et al., *Photofixation of atmospheric nitrogen to ammonia with a novel ternary metal sulfide catalyst under visible light.* RSC Advances, 2016. **6**(55): p. 49862-49867.

72. Hu, S., et al., *Effect of sulfur vacancies on the nitrogen photofixation performance of ternary metal sulfide photocatalysts.* Catalysis Science & Technology, 2016. **6**(15): p. 5884-5890.

73. Zhao, Y., et al., *Layered-Double-Hydroxide Nanosheets as Efficient Visible-Light-Driven Photocatalysts for Dinitrogen Fixation.* Advanced Materials, 2017. **29**(42): p. 1703828.

Chapter Two

Semiconductor photoelectrochemical build and preliminary tests

2.1. Introduction

To build a successful photoelectrochemical system; sustainable and relatively efficient conversion of sunlight into photochemical energy is crucial. A substantial fraction of the light must be absorbed and should generate spatially separate excited electrons and holes. The recombination of photo-generated electrons/holes should be minimal, while these charge carriers need to be swiftly directed to sites that prefer charge transfer to species in solution. The desired photo-induced chemical reaction should possess a sufficiently fast reaction kinetics. In short, the operational efficiency of a photo-electrochemical system depends critically on the associated interfacial physiochemical and electrochemical properties and strongly on the individual material properties of each component.[1]

Research in this field has been focused on bridging the 'gap' between systems that can absorb light efficiently and those that can achieve prolonged reactions with reasonable efficiencies. Experimental evidence shows that many perceived obstacles can be overcome through the rational design of the photoelectrochemical systems.[1]

This section begins with a review of the background literature in the field of b-Si and plasmonic nano-article attachment. It then describes the methods used in this work to prepare and characterise decorated b-Si-based photo-catalytic devices.

2.2. Device kinetics

The performance of semiconductor devices has been widely discussed in many reviews and introductory books [2-4].In particular, the performance of photovoltaic semiconductors in contact with redox couples is the interest of this section.

To design an efficient solar photocatalytic cell, it is quite crucial to understand[5]

- The physics of the semiconductors device
- The semiconductor-liquid contact (interface) thermodynamic and kinetic parameters
- The function of the surface electro-catalyst

In general, the semiconductor device physics relates to the electron flow through the designed semiconductor and the interface with the redox couple. The semiconductor-liquid interface contains a redox couple (acceptor, A, and the donor, D^-) having electrochemical potential $-qE°(A/ D^-)$ where E° is the Nernst potential of the redox pair (A/ D^-). The electronic flow will emerge through the designed semiconductor components as soon as they are in contact with each other, controlled by the work function of each component [6]. Solution/semiconductor interfacial electric fields will be established as the electronic flow between the semiconductor, and the solution emerges until equilibrium is reached. The Fermi level and the electrochemical potential will be the same after equilibrium (Figure 2-1). [1, 5]

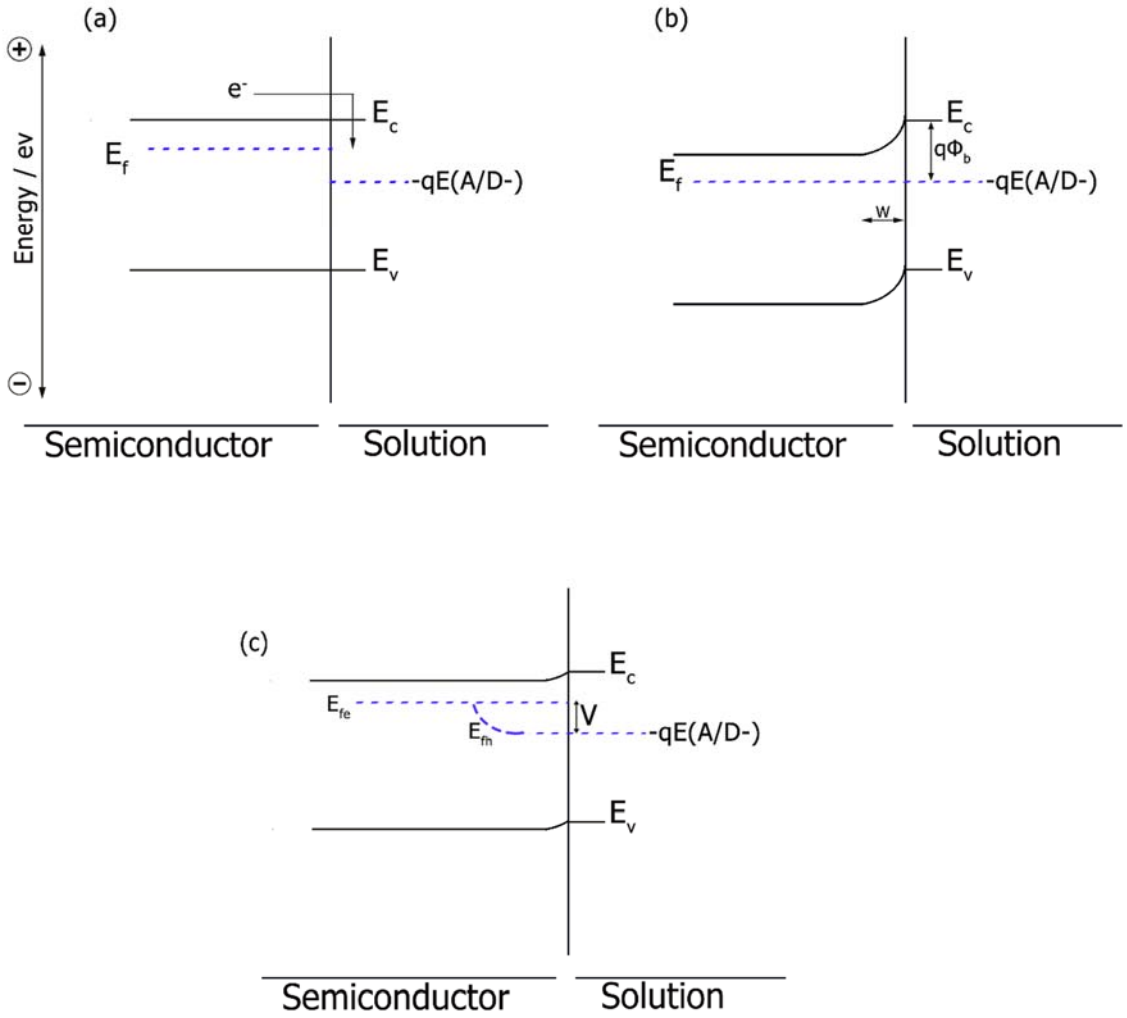

Figure 2-1: Band energy equilibration of a semiconductor/liquid interface and Fermi level E_f (a) before and (b) after equilibrium is reached, both in the dark, while (c) is in quasi-static equilibrium under steady illumination; the solution Nernstian potential is qE(A/D$^-$). $q\Phi_b$ is the barrier height; the maximum theoretical energy that can be extracted from separated electron/hole pair at the junction. At equilibrium, in the absence of illumination, Fermi level E_F of the semiconductor is equal to qE(A/D$^-$). Under steady illumination (c), a non-equal electron and hole population is generated. E_{fe} is the electron and E_{fh} is the hole quasi-Fermi level. The voltage generated V by the junction under illumination is obtained by the difference between E_{fe} and qE(A/D$^-$) (reproduced from [5])

For a typical p-type semiconductor photo-cathode in equilibrium with species in solution (e.g., N_2/NH_3), the electrode will generate an excess negative charge, developed from the ionised dopant atoms (Boron in the case of Silicon) in the semiconductor. The negative charge is dispersed over the depletion width, W, in the semiconductor; conversely, the positive charge is spread over a substantially narrower region (the Helmholtz double layer) close to the electrode in the solution. A P-type semiconductor is traditionally used as a photo-cathode because the electric field that is developed in equilibrium results in band bending, due to the drop in the electric field strength in the solid, that directs photogenerated minority charge carriers (electrons, for P-type semiconductors) to move into the solution.[5, 7]

The strength of the electric field and, hence, the potential energy barrier, depends on the difference between the initial energy of the semiconductor Fermi level and the value of -qE(A/D-) (see figure 1). Absorption of the light generates charge carriers (electron/hole pairs); these pairs are generally very spatially separated by the generated electric field because crystalline inorganic semiconductors have relatively high mobilities of charge carriers (10-1000 $cm^2\ V^{-1}\ s^{-1}$). Given the initial difference in electrochemical potentials is on the order of 1 eV, and the depletion width in the semiconductor is typically on the order of hundreds of nanometers, the semiconductor electric field can be as large as $10^5\ V\ cm^{-1}$[5].

In early literature [8-10], the ideally behaved illuminated semiconductor/liquid interface was expected to have V equal to $q\Phi_b$ (Figure 2-1). However, a detailed study of unpinned silicon/liquid contacts showed that the maximum V obtained is less than $q\Phi_b$ and mainly limited by kinetic instead of thermodynamic factors[11, 12]. The generated electron/hole pair can be recombined in the bulk semiconductor, at the surface states or in the depletion region.

The excited electrons may finally tunnel through the interface to reduce species in the solution. [1]

2.3. Materials morphology and design

2.3.1. Enhancements of the surface structure

A study published in 2009, using a regenerative ferrocenium/ferrocene redox system, has demonstrated that re-structuring GaP, by etching, increases the photocurrent [13]. Also recently, higher photocurrent and larger persistent photoconductivity were obtained in a nanoporous GaN compared to un-etched n-GaN. This peculiar photo-response was attributed to the space charge model in the nanoporous structure[14]. Another good light absorber is InP (band gap 1.35 eV). However, limited availability decreases its commercial and scientific interest[15]. Etching of ZnSe was found to considerably decrease electron-hole recombination rates, and thus, thus significantly increases the photocurrent of a single-crystal ZnSe electrode in various electrolytes [16]. A porous form of hematite (Fe_2O_3), was generated after etching its crystalline form with HF. The etched form has proven to have a higher photoelectrochemical efficiency than the as-prepared form due to its porosity[17].

Etching of silicon (as will be explained in greater detail later in this chapter), has been proven to boost it photocurrent and enhance its photochemical efficiency. The formed nano-wires on its surface increase the path length of incident light by up to a factor of 73. This exceptional light-trapping path length enhancement factor is well above the Lambertian limit ($2n2 \sim 25$ without a back reflector) and is relatively superior to other light-trapping methods [18, 19].

2.3.2. Plasmonic effects

The power conversion efficiency (PCE)[20] is controlled by the absorption of light and the collection of the generated charges[21]. The recombination of electron/hole pairs becomes predominant with a consequent decrease of the PCE whenever the active semiconductor layer is thicker[22]. Light trapping, due to the depositing of metallic nanoparticles can provide a significant enhancement to the PCE. Nanoparticles of metals like Au, Ag are attached to the semiconductor surface to increase the optical path length of the light on the device surface to enhance light absorption through Surface Plasmon Resonance (SPR)[22].

Stimulated by incident light the SPR can be defined as “the resonant oscillation of conduction electrons at the interface between negative and positive permittivity material”[23]. The incident light scattered as a function of particle size at a specific frequency leads to collective oscillation of electrons in the metallic nanoparticles and a stronger absorption. In fact, gold metallic nanoparticles have been already proven to enhance silicon photocurrents by 33%[24]

These electromagnetic properties of metal nanoparticles have been previously known since 1902 [25], but the interest in these properties has increased lately with the development of new nanofabrication techniques.

Incident light is scattered or absorbed in the region of the resonance wavelength of the particles, depending on the size of the particles. The suppression of the particles is defined as the sum of the absorption and scattering [24]. For nanoparticles in the quasistatic limit, the absorption and scattering cross sections are given by (eq 9 and 10) [26]

$$\boldsymbol{C}\text{abs} = \frac{2\pi}{\lambda} \boldsymbol{Im}\,[\alpha] \text{.....9}$$

And

$$\boldsymbol{C}\text{sca} = \frac{1}{6\pi}\left(\frac{2\pi}{\lambda}\right)^4 [\alpha]^2 \text{.....10}$$

Where λ is the wavelength, α is the polarizability of the particle, given that α = 3V (ε-1)/(ε+ 2), V is the volume of the particle and ε is the permittivity of the metal.

As mentioned earlier and given in the equation above, the size (volume) of the particles plays a crucial role in the absorption and scattering of the incident light. Smaller than wavelength nanoparticles tend to absorb more light and dominate the extinction. On the other hand, as the size of the particles increases, light scattering dominates extinction. However, less efficiency of the scattering process is expected, due to, the higher order multipole excitation modes and retardation effects with increasing particle size[24].

Size, shape, material, and refractive index of the surrounding medium are the main factors affecting the resonance frequency. For example, change of the resonance frequency can happen by over-coating of the metal particles on a substrate. Practically, depositing larger size particles on a substrate leads to a loss of the spherical geometry towards ellipsoids, this change in shape causes a red-shifting of the resonance frequency[27]. Materials used can also effect resonance, as can be seen by depositing the same particle size of gold and silver; silver nanoparticles have a higher frequency resonance than gold nanoparticles. Alloying

them together in different ratios yield a new resonances between that of the pure gold and silver particles resonances[28].

In short, the plasmonic effect of surface-attached nano-particles can increase the efficiency of solar cell structures and reduces the problem of electron/hole recombination which occurs when silicon is textured directly. This effect depends mainly on the shape, size, material, and refractive index of the attached nanoparticles.

2.4. Materials design

2.4.1. Silicon

Silicon (Si) materials, which demonstrate a wide optical adsorption range, high absorption efficiency, and high electron mobility, are potential photoelectric conversion materials for essential applications in the field of photovoltaics and photocatalysis[29, 30]. Flat Si surfaces, however, have a high natural reflectivity with a robust spectral dependence. Minimisation of reflection losses is of crucial importance for light absorbing applications, such as high-efficiency solar cells. Different approaches have been developed to avoid reflectance, in many cases specific to a particular surface morphology[31, 32]. Black silicon is a surface alteration of reflective silicon with very low reflectivity and correspondingly high absorption of visible (and infrared) light. Recent investigations have shown that black silicon (b-Si) exhibits enhanced photoelectrochemical and photocatalytic performance [33-35].

2.4.1.1. Black silicon (b-Si)

Black silicon (b-Si) is a surface modified silicon where a nanoscale surface structure is formed after an etching process[36]. It is a low reflectivity (less than 1%), highly photo-sensitive material, 100 to 500 times more light sensitive than regular silicon[37]. The first discovery of this material was at Harvard University by accident in 1980 during a reactive ion etching (RIE) experiment. They applied a hyper-powerful laser (matching the whole sunlight energy for the entire earth) on a silicon surface, while simultaneously adding sulphur hexafluoride. A black surface (as seen by the naked eye) was formed, which on closer inspection was revealed to be microscopic spikes (in the form of hairy nanowires)[38]. Eric Mazur's laboratory at Harvard University (1998) developed a method forming a similar structure using femtosecond laser pulses, called Mazur's approach [39].

The b-Si nano-structural surface consists of either cones with tips pointing away, made of single-crystal silicon and a height >10 µm and diameter less than 1 µm[40], or a series of nano-scale pores randomly distributed with a variety of heights and depths. This surface exhibits broad absorption optical range (250-2500 nm)[41], due to the formation of a so-called “effective medium”[42]. Because of this property, b-Si is an ideal coating for solar cells[43-45], as well as for photo-detectors (with high-efficiency through increased absorption)[46], and gas sensors[47].

2.4.1.2. Fabrication of b-Si

The fabrication processes of b-Si are classified according to the condition by which the etching process is done: either wet or dry etching. The two methods have positive and negative aspects, but the resulting b-Si is essentially the same. Wet etching is somewhat more

preferable than dry, especially in industrial application, because it does not need expensive instruments, high energy consumption or complicated fabricating processes[48].

2.4.1.2.1. **Wet etching methods**

Wet etching is a process of material removal that uses liquid chemicals, or etchants, to remove materials from a wafer of silicon[49]. Usually, this process contains three steps: (a) spread of etchant solution (usually HF) on the wafer surface; (b) a redox reaction between the wafer material and the etchant; (c) side products migrating away, leaving the desired surface[49, 50].

Traditionally, the silicon wafer etching process is subdivided into metal-assisted (catalysed) etching and electrochemical etching [48, 51]. The Metal-assisted chemical etching (MACE) is an electroless process that uses a redox reaction to deposit metal onto a surface, while electrochemical methods involve deposition of premade nano-metal particles (NPs) on a surface. Both processes are followed by etching using an oxidant[51]. The first step is depositing a metal (such as Au, Ag, or Pt) as NPs on the silicon surface. NPs attract electrons on the silicon surface which will promote the oxidation to silica (SiO_2) in the presence of a suitable oxidant. The second step is etching; HF is used to remove the formed silica by converting it into H_2SiF_6. A pit is expected to be produced on the surface of the silicon under each NP[52]. The proposed mechanism for the etching process is

$$H_2O_2 + 2H^+ + 2e^- \rightleftharpoons 2H_2O \quad \text{----------} \quad (1)$$
$$Si + 2H_2O \rightleftharpoons SiO_2 + 4H^+ + 4e^- \quad \text{----------} \quad (2)$$
$$SiO_2 + 6HF \rightleftharpoons H_2SiF_6 + 2H_2O \quad \text{----------} \quad (3)$$
$$Si + 2H_2O_2 + 6HF \rightleftharpoons H_2SiF_6 + 4H_2O \quad \text{----------} \quad (4)$$

Wherein (Eq 1), a cathodic reaction occurs at the metal NP surface, in (Eqs 2 and 3) anodic reaction that takes place at the contact point between silicon and NPs[48, 53-55]. The voltage difference between the two electrodes increases the concentration of electrons on the cathode electrode, which stimulates the reaction in (Eq 4) which results in continued etching of the silicon surface.

Generally, the formation and morphology of the b-Si surface is affected by

- The procedure of metallization
- composition of the etching solution
- etching time

Various metallization procedures will yield different pore sizes and density[56]. The etching solution composition plays an important role in the dissolution of the SiO_2, and later in the morphology of the b-Si [57-59]. The depth of the pores of the silicon substrate is directly proportional to the etching time and the rate of penetration of NPs on silicon surface[57].

2.4.1.2.2. Dry etching methods

Dry etching methods use either lasers, plasmas or gases to remove surface material. The reaction is achieved using high kinetic energy particle beams, a chemical reaction, or a combination of both [49].

A substantial amount of work has been done on the dry RIE of silicon substrates, mainly on the inductively coupled plasma reactive ion etching (ICP-RIE) and damage-free reactive ion etching [60]. Combinations of two gases were primarily used in RIE: the first gas reacts with the surface by forming radicals species, while the other gas passivates the surface after obtaining the desired etches [61-63]. The typical gas mixtures are a combination of SF_6/O_2, $SF_6/Cl_2/O_2$, or $SF_6/O_2/CH_4$. The desired surface morphology is achieved by controlling

the plasma chemistry, radio frequency (RF) power, and pressure. The resulting morphology can be isotropic, positively and negatively tapered, or even fully vertical walls [38, 48, 61].

The other important technology is plasma immersion ion implantation (PIII) or pulsed-plasma doping (pulsed PIII)[64]. This process of etching depends on applying a high voltage pulsed DC power supply and targeting them into the substrate with a silicon wafer placed over it, in order to implant it with desired dopants [65].

In a conventional plasma immersion system, an atmosphere consists of working gas at a suitable pressure. A chamber consists of two parts separated by conducting grid: an upper region of plasma and a lower reactive region. The top area of the chamber confines the plasma and stops the expansion of the ion, while the grid repels electrons that are close to it. As a result, positive ions are the only ions that diffuse into the lower part through the grid and are implanted into the wafer. Hot NaOH is used to remove surface damage of the silicon surface. Later, the action gases (i.e. SF_6/O_2) react (as ions and free radicals) with the surface of the silicon substrate; a high negative voltage pulse is applied to cause the injected ions to react with the silicon substrate[66]. Practically, an etching mask is formed (deposited) from an array of silver or gold nanoparticles[67]. In the next step, the reactive etching gas is injected into the chamber, and when a voltage is applied, the areas without Ag or Au NPs (masking agents) are etched, while other areas with NPs remain un-attacked. Finally, the masking NPs are removed from the surface, leaving etched silicon. The morphology of this surface critically depends on etching time[68].

In addition to plasma, laser pulses have been introduced to irradiate the silicon wafers[69-71]. Femtosecond lasers are famous for preparing b-Si; however, the pulse length of the lasers range from femtosecond to picosecond in some cases. To control the morphology of the resulting b-Si, different reagents (e.g. liquid chlorine (CCl_4) and fluorine ($C_2Cl_3F_3$) precursors)

can be used to increase the etching rate and form different desired morphologies[70, 72]. Most importantly, the resulting morphology of the b-Si through most dry etching methods is controlled by the reaction rates and/or relative reactivity of the reagents[48].

2.4.2. Application of black silicon (b-Si)

B-Si is known for its ability to emit terahertz radiation (electromagnetic waves between microwave and infrared regions). This type of radiation has its application in medical imaging[73], communication, power generation[74], spectroscopy, sub-millimetre astronomy, hydrogen production through photoelectrochemical water splitting[75] and in many other fields[76]. As such, many researchers use b-Si as a source of terahertz radiation [77-79].

One of the essential applications of b-Si is in the fabrication of solar cells, and this is due to the growing need for energy sources that are cheap, reliable, sustainable and environmentally friendly[80]. Wet fabrication method has been used to manufacture most of the b-Si solar cells[81, 82]. Some research[33] showed that the nano-textured silicon solar cell performed best in the 30 s MACE process, where the efficiency of the cells and the current density (J_{sc}) were about 18.2% and 28.9 mA/cm^2 respectively. Plasma immersion ion implantation (PIII)[65] have also been used to produce b-Si solar cells under a variety of conditions. Results show that pins with an average height of 150 – 600 nm have been fabricated on b-Si surfaces by applying different forming conditions and increasing the hight of the pins decreases the wavelength from 300 nm to 1100 nm. The Si-based solar cell on the optimised pins height of 300 nm resulted in an efficiency of 15.99% with a short circuit current of 34.0 mA/cm^2[83].

Yuan et al. [40] conducted a simple, one-step, nanoparticle-catalysed b-Si etching that can provide effective antireflection for relatively efficient solar cells. A 3 min b-Si etching

process produced pores about 500 nm deep, providing a good settlement between surface reflection and internal quantum efficiency (IQE) loss.

The use of b-Si surface as a catalyst to perform oxidation-reduction reactions has many challenges because of its hydrophobicity and relatively weak catalytic activity. However, it has been used widely, primarily when a relatively efficient catalyst is attached [84]. The most extensive application for it is in water-splitting reactions[85].

2.4.3. Plasmonic gold coating

Semiconductor-metal nanocomposites have been vastly utilised in photocatalysis field. The efficiency of photocatalysis reactions was improved when metal nanoparticles were deposited on its surface; examples include titania as semiconductor [86-88] and electrodeposited Pt nanoparticles on cathode platforms for hydrogen generation [89-94]. The role of metal nanocomposites in the interfacial charge-transfer processes is not understood fully yet[95]. A full understanding of the energy levels of such nanocomposite systems is essential for designing the future properties of next-generation photovoltaic cells [88]. In this context, extensive attention has been applied to water splitting reactions using titania nanoparticles modified with nano-metals (like Au, Pt and Ag) [96]. On the other hand, nitrogen conversion has received less attention, possibly due to its experimental challenges and low conversion efficiency.

Metal nano-deposits may act as a conduit for electrons, withdrawing them away from the holes that exist in the other side of the semiconductor. Figure 2-2 shows the intermediate

function of nanometals in saving and shuttling the photogenerated electrons from the semiconductor to an acceptor in a photocatalytic process.[88]

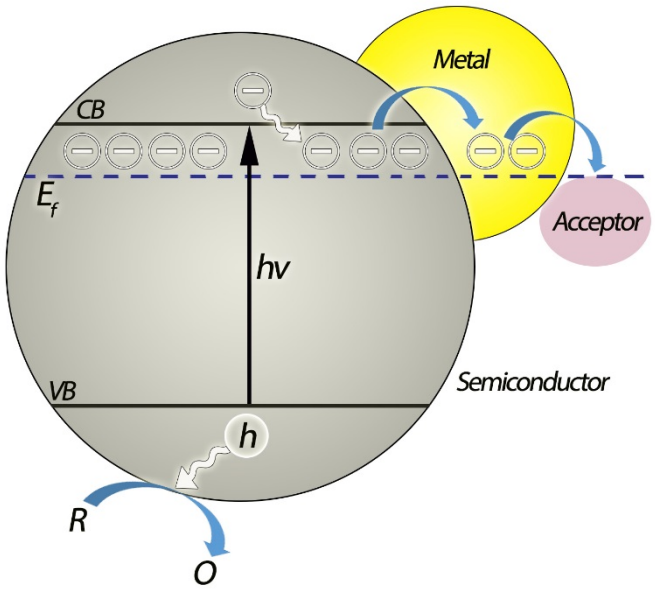

Figure 2-2: metal nanoparticles effect on the photogenerated electrons from the semiconductor to an acceptor reaction (reproduced from ref. [88])

The reported theory for this[95] involves the formation of a barrier at the metal-semiconductor interface called the Schottky barrier. This barrier is formed when an electrically neutral and isolated metal and semiconductor are attached to each other. The conduction band levels of metal and semiconductor are different, but when connected, the two cause electrons to transfer from the semiconductor to the metal until the two levels are equal at the interface. This new electrical contact creates a space-charge layer caused by the movement of electrons and holes away from the barrier region; the surface of the metal withdraws the electrons, while, the surface of the semiconductor withdraws holes.

In the literature[97, 98], gold nanoparticles (GNP) have been shown to absorb both UV and visible light, being able to use a broader range of the solar spectrum. Gold nanoparticles absorb visible light due to their plasmonic effect (surface plasmon resonance (SPR) described earlier in this chapter), which, increases an absorption maximum at approximately 560 nm.

The difference in the conduction levels value between titania alone and titania with deposited GNP is about 22 mV more negative[99], and this may be attributed to the surface barrier (Schottky barrier) behaviour between the titania and the gold particles, which motivates the electron migration processes yielding an efficient separation of charges.

Prashant, et al.[88] have also studied the effect of metal particle size on the Fermi Level equilibration (the level of energy below conduction band; caused by attached nano-metal). They found that this addition caused the Fermi level to become more negative, thus, moving the Fermi level closer to the conduction band of the semiconductor.

Combining these concepts into a single structure the predicted co-catalyst and hole scavenging contributions in a nitrogen conversion reaction based on b-Si is explained in figure 2-3 below. This explanation is based on the proved contributions of those factors in the photocatalysis process through literature [95, 100].

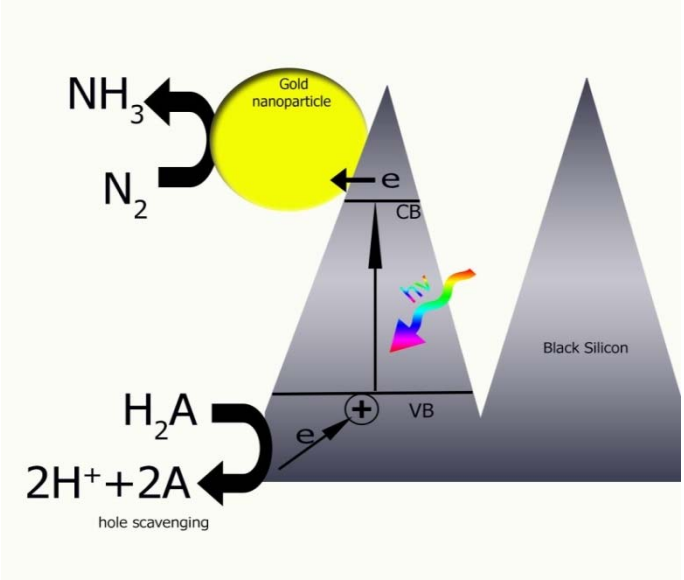

Figure 2-3: Predicted mechanism of the simultaneous reactions of nitrogen and hole scavenger over metal promoted black silicon under illumination.

2.5. Semiconductor preparation

In the present work, a p-type boron-doped 100 mm commercial <100> silicon wafer (resistivity=10–20 ohm cm^{-1}) of 525 µm thickness (Atecom Ltd, Taiwan) was used as a substrate material for black silicon formation. The wafers were used as supplied. The dry etching process was carried out using an Oxford PlasmaLab 100 ICP380 system. The etching process was a mixed mode, wherein etching and passivation occurred at the same time. Process conditions for the black silicon formation were: SF6 gas flow rate 65 sccm, O2 gas flow rate 44 sccm, process pressure of 35 mTorr, 100 W reactive ion etching (RIE) power, 20 °C electrode temperature and 10 Torr He backside cooling pressure. The RIE process resulted in a homogeneously distributed silicon nanowire arrays with length about 3 µm across the full wafer after 20 min etching. Nitrogen adsorption-desorption experiments were performed at 77 K with a Micromeritics Tristar II. The samples were degassed at 200°C for 5 h before measurement. The surface area of bSi calculated from nitrogen sorption results by Brunauer–Emmett–Teller method is 10.4 cm^2. After the RIE process, the gold coating was carried out on a K550X sputter coater at 25 mA at 1 × 10−1 mbar. The discharge time was 4 min. The size of the GNPs ranges from 3 to 30 nm.

2.6. Initial Application Tests (Rhodamine B (RB) degradation)

A study of Rhodamine B (RB) degradation was carried out to test the photocatalytic activity of b-Si with GNPs on its surface. A cell was built to avoid issues arising from evaporation, leak elimination, and stable conditions obtained. The cell was manufactured totally from PVC, and a specially designed rubber ring was used to enable fixing the b-Si sample into the intended place and to eliminate leaks. The capacity of the designed cell was set to be 1ml ($1cm^3$); the sample b-Si wafers were fixed to $0.5cm^2$ in area (Figure 2-4).

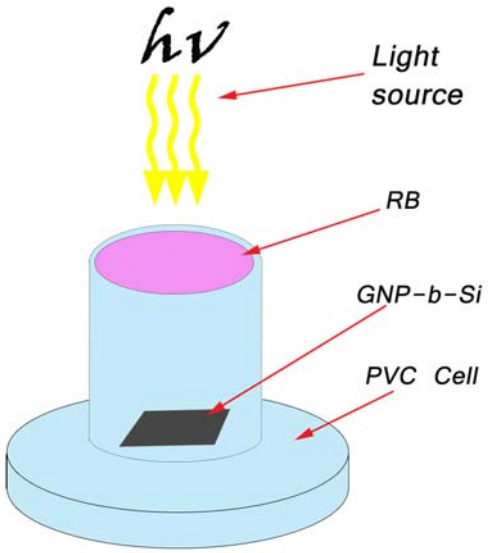

Figure 2-4: Rhodamine B (RB) degradation cell design

Degradation of 0.01g/L RB was monitored using UV-Vis spectroscopy; a test was done for the resultant solution after each 60 min of illumination (Figure 2-5A). Results show that the RB absorption is inversely proportional to the time of illumination and the calculated rate

of degradation was $1.6x10^{-8}$ M/min. The expected mechanism[101, 102] possibly involves four main reactions:

$$RB + h\nu \rightarrow RB^{*} \quad \text{(1)}$$

$$RB^{*} + O_2 \rightarrow RB^{+*} + O_2^{-*} \quad \text{(2)}$$

$$O_2^{-*} + H^{+} \rightarrow OOH^{*} \quad \text{(3)}$$

$$RB^{+*} \rightarrow \text{Rhodamine} \rightarrow \text{products} \quad \text{(4)}$$

In (eq 1), RB is excited by irradiation with a combination of visible and UV light, which then reduces O_2 to O_2^{-*} (eq 2). In (eq 3) the active O_2^{-*} readily reacts with protons in water (from autoprotolysis) to form OOH^{*}, which is crucial for the N-de-ethylation of RB, which in turn is necessary for the complete degradation of the dye[102]. The last equation (eq 4) describes an overall view of how the highly reactive RB^{+*} reacts with RB to produce minor products like carbon dioxide and other small products[103]. These results were later compared with the illumination of RB (0.01g/L) on b-Si wafer surface (Figure 2-5B).

RB Illumination in the presence of b-Si showed that aqueous RB losses it's distinctive red colour faster (about 300 min) than without silicon (more than 540 min). UV-Vis data of Figure 2-5 confirms this observation. The calculated rate of decomposition from a plot of absorbance vs time in Figure 2-6 is $5.95x10^{-8}$ M/min, which is higher than when the illumination is done without the b-Si catalyst wafer.

B-Si plated with gold NPs (GNPs) has also been used for the same purpose (Figure 2-5C, 2-6). The results were notable; the NP plated b-Si has a stronger ability compared with b-Si to behave as a photocatalytic agent. This may be attributed to the plasmonic effect of GNPs, which are bound to the surface and interact actively with light resulting in a polariton [104,

105]. The plasmonic effect of gold could play an essential role in the optical properties of silicon, as in the ultraviolet range it absorbs in the plasma frequency, while in the visible range gold has electronic inter-band transitions. In total, the resultant surface (plated with GNPs) can absorb light from both regions of light[106].

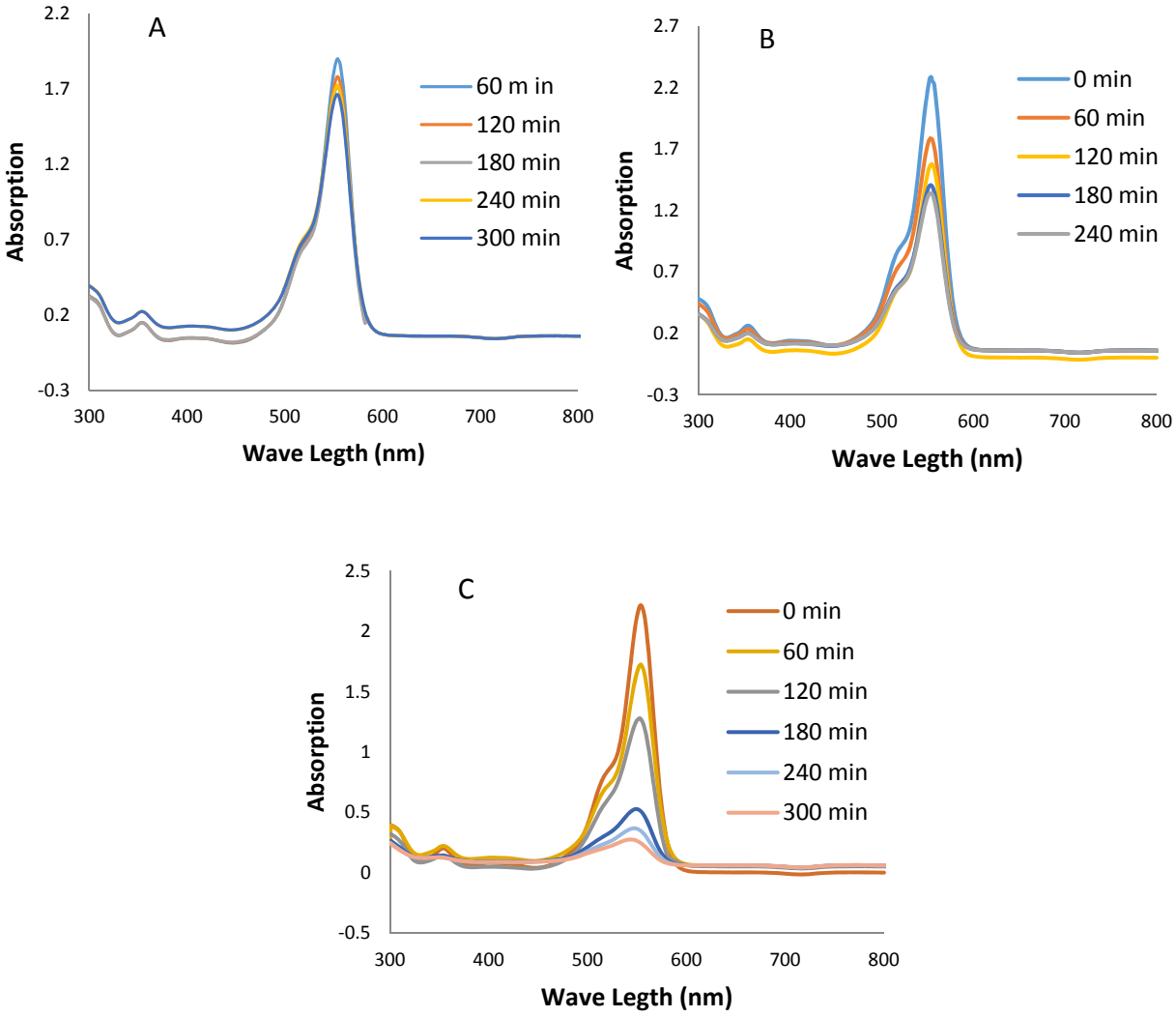

Figure 2-5: Absorption spectra of RB [0.01g/L] aqueous solution in the presence of A: no catalyst, B: b-Si, C: b-Si with GNPs during illumination

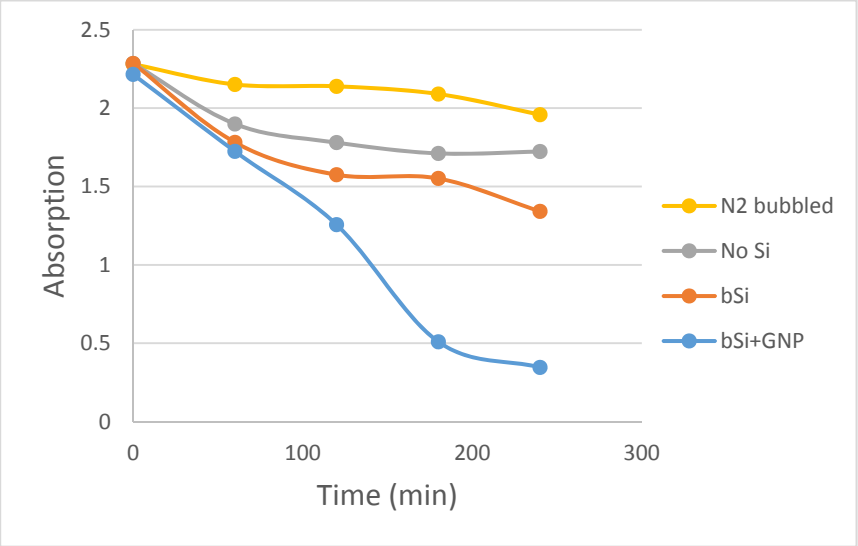

catalyst	Rate M/min
bSi+GNP	7.34 E-08
b- Si	2.80 E-08
without b-Si (no catalyst)	2.14 E-08
N_2 bubbled (No oxygen)	1.34 E-3

Figure 2-6: Comparison of absorption spectra of RB [0.01g/L] aqueous solution with and without b-Si, GNPs plated b-Si and without catalyst

Another experiment has been done to confirm that oxygen plays a role in the mechanism of degradation. The experiment involved de-oxygenating the solution with nitrogen gas before and during the experiment. The results confirmed that the presence of oxygen is crucial in this mechanism and the RB degradation is not possible in a solution without O_2 (Figure 2-6).

2.7. Summary and Conclusions

Many factors impact on the efficiency of a photovoltaic cell, including choosing the appropriate semiconductor with suitable bandgap, selecting the dopant and as a result, semiconductor conductivity, and surface modification which manipulate the semiconductor-liquid interface thermodynamic and kinetic parameters.

In addition to charge separation, surface modification significantly affects light absorption. Etching the silicon boosts it photo-absorption by up to 500 times. Black silicon (b-Si) is an etched form of silicon that has better ability to absorb light with a broader wavelength and has better charge separation than flat (unetched) silicon. There are two main approaches to prepare b-Si, dry and wet etching. Also, metal attachment to the semiconductor surface increases light absorption by plasmon resonance. The attached metal type, size, shape, and refractive index of the surrounding medium are the main factors affecting the resonance frequency.

In this part of the thesis, dry etched silicon wafers with gold nanoparticles deposited into its surface were tested. The superior photocatalytic abilities of the prepared cell compared to flat silicon was proven through photocatalytic degradation of RB dye. B-Si shows a better ability to degrade the dye, while the GNP coated b-Si showed further improvement. Also, the reaction mechanism was proven, whith less degradation being achieved with oxygen-free electrolyte.

2.8. REFERENCES

1. Archer, M.D., *Nanostructured and photoelectrochemical systems for solar photon conversion*. Vol. 3. 2008: Imperial College Press.
2. Tan, M.X., et al., *Principles and applications of semiconductor photoelectrochemistry.* Progress in Inorganic Chemistry, Volume 41, 1994: p. 21-144.
3. Nozik, A.J. and R. Memming, *Physical chemistry of semiconductor− liquid interfaces.* The Journal of Physical Chemistry, 1996. **100**(31): p. 13061-13078.
4. Gerischer, H., *The role of semiconductor structure and surface properties in photoelectrochemical processes.* Journal of Electroanalytical Chemistry and Interfacial Electrochemistry, 1983. **150**(1-2): p. 553-569.
5. Walter, M.G., et al., *Solar water splitting cells.* Chemical reviews, 2010. **110**(11): p. 6446-6473.
6. Lang, N. and W. Kohn, *Theory of metal surfaces: work function.* Physical Review B, 1971. **3**(4): p. 1215.
7. Lewis, N.S., *Chemical control of charge transfer and recombination at semiconductor photoelectrode surfaces.* Inorganic chemistry, 2005. **44**(20): p. 6900-6911.
8. Baglio, J.A., et al., *Electrochemical characterization of p-type semiconducting tungsten disulfide photocathodes: efficient photoreduction processes at semiconductor/liquid electrolyte interfaces.* Journal of the American Chemical Society, 1983. **105**(8): p. 2246-2256.

9. Aruchamy, A. and M.S. Wrighton, *A comparison of the interface energetics for n-type cadmium sulfide/-and cadmium telluride/nonaqueous electrolyte junctions.* The Journal of Physical Chemistry, 1980. **84**(22): p. 2848-2854.

10. Schneemeyer, L.F. and M.S. Wrighton, *n-Type molybdenum diselenide-based photoelectrochemical cells: Evidence for Fermi level pinning and comparison of the efficiency for conversion of light to electricity with various solvent/halogen/halide combinations.* Journal of the American Chemical Society, 1980. **102**(23): p. 6964-6971.

11. Rosenbluth, M.L., C.M. Lieber, and N.S. Lewis, *630 ‐ mV open circuit voltage, 12% efficient n ‐ Si liquid junction.* Applied Physics Letters, 1984. **45**(4): p. 423-425.

12. Lieber, C.M. and N.S. Lewis, *Catalytic reduction of carbon dioxide at carbon electrodes modified with cobalt phthalocyanine.* Journal of the American Chemical Society, 1984. **106**(17): p. 5033-5034.

13. Price, M.J. and S. Maldonado, *Macroporous n-GaP in nonaqueous regenerative photoelectrochemical cells.* The Journal of Physical Chemistry C, 2009. **113**(28): p. 11988-11994.

14. Lee, Y.-H., J.-H. Kang, and S.-W. Ryu, *Enhanced photocurrent and persistent photoconductivity in nanoporous GaN formed by electrochemical etching.* Thin Solid Films, 2013. **540**: p. 150-154.

15. USGS, *Mineral Commodity Summaries 2010*, U.S.G. Survey, Editor. 2010, United States Government Printing Office, Washington: 2010.

16. Tenne, R., H. Flaisher, and R. Triboulet, *Photoelectrochemical etching of ZnSe and nonuniform charge flow in Schottky barriers.* Physical Review B, 1984. **29**(10): p. 5799.

17. HU, Y.-X., et al., *Effect of HF Treatment on the Photoelectrochemical Properties of a Hematite Thin Film Photoanode for Water Splitting.* Acta Physico-Chimica Sinica, 2014. **30**(6): p. 1099-1106.

18. Garnett, E. and P. Yang, *Light trapping in silicon nanowire solar cells.* Nano letters, 2010. **10**(3): p. 1082-1087.

19. Han, S.E. and G. Chen, *Toward the Lambertian limit of light trapping in thin nanostructured silicon solar cells.* Nano letters, 2010. **10**(11): p. 4692-4696.

20. Dennler, G., M.C. Scharber, and C.J. Brabec, *Polymer‐fullerene bulk‐heterojunction solar cells.* Advanced materials, 2009. **21**(13): p. 1323-1338.

21. Schilinsky, P., C. Waldauf, and C.J. Brabec, *Recombination and loss analysis in polythiophene based bulk heterojunction photodetectors.* Applied Physics Letters, 2002. **81**(20): p. 3885-3887.

22. Notarianni, M., et al., *Plasmonic effect of gold nanoparticles in organic solar cells.* Solar Energy, 2014. **106**: p. 23-37.

23. https://en.wikipedia.org/wiki/Surface_plasmon_resonance. *Surface plasmon resonance*. 2017 1 July 2017.

24. Pillai, S., et al., *Surface plasmon enhanced silicon solar cells.* Journal of applied physics, 2007. **101**(9): p. 093105.

25. Wood, R., *XLIV. A suspected case of the electrical resonance of minute metal particles for light-waves. A new type of absorption.* The London, Edinburgh, and Dublin Philosophical Magazine and Journal of Science, 1902. **3**(16): p. 396-410.

26. Craig, F.B., F. Bohren, and D. Huffman, *Absorption and scattering of light by small particles.* Inc: John Wiley & Sons, New York, USA, 1983.

27. Royer, P., et al., *Substrate effects on surface-plasmon spectra in metal-island films.* Physical Review B, 1987. **35**(8): p. 3753.

28. Baba, K., T. Okuno, and M. Miyagi, *Silver‐gold compound metal island films prepared by using a two‐step evaporation method.* Applied physics letters, 1993. **62**(5): p. 437-439.

29. Service, R.F., *Materials science - Silicon lights the way to faster data flow.* Science, 2001. **293**(5534): p. 1413-1414.

30. Ng, W.L., et al., *An efficient room-temperature silicon-based light-emitting diode.* Nature, 2001. **410**(6825): p. 192.

31. Blanco-Redondo, A., et al., *Observation of soliton compression in silicon photonic crystals.* Nature Communications, 2014. **5**.

32. Hafezi, M., et al., *Imaging topological edge states in silicon photonics.* Nature Photonics, 2013. **7**(12): p. 1001-1005.

33. Oh, J., H.-C. Yuan, and H.M. Branz, *An 18.2%-efficient black-silicon solar cell achieved through control of carrier recombination in nanostructures.* Nature Nanotechnology, 2012. **7**(11): p. 743-748.

34. Ao, X., et al., *Black silicon with controllable macropore array for enhanced photoelectrochemical performance.* Applied Physics Letters, 2012. **101**(11).

35. Steglich, M., et al., *Improvement of Ge-on-Si photodiodes by black silicon light trapping.* Applied Physics Letters, 2013. **102**(11).

36. Bhardwaj, J.K. and H. Ashraf. *Advanced silicon etching using high-density plasmas*. in *Micromachining and Microfabrication*. 1995. International Society for Optics and Photonics.

37. Srivastava, S.K., et al., *Silver catalyzed nano-texturing of silicon surfaces for solar cell applications.* Solar Energy Materials and Solar Cells, 2012. **100**: p. 33-38.

38. Jansen, H., et al., *The black silicon method: a universal method for determining the parameter setting of a fluorine-based reactive ion etcher in deep silicon trench etching with profile control.* Journal of Micromechanics and Microengineering, 1995. **5**(2): p. 115.

39. Wang, C., et al., *The thresholds of surface nano-/micro-morphology modifications with femtosecond laser pulse irradiations.* Nanotechnology, 2010. **21**(7): p. 075304.

40. Yuan, H.-C., et al., *Efficient black silicon solar cell with a density-graded nanoporous surface: Optical properties, performance limitations, and design rules.* Applied Physics Letters, 2009. **95**(12): p. 123501.

41. Crouch, C., et al., *Infrared absorption by sulfur-doped silicon formed by femtosecond laser irradiation.* Applied Physics A, 2004. **79**(7): p. 1635-1641.

42. Choy, T.C., *Effective medium theory: principles and applications*. 1999: Oxford University Press.

43. Liu, Y., et al., *Nanostructure Formation and Passivation of Large‐Area Black Silicon for Solar Cell Applications.* Small, 2012. **8**(9): p. 1392-1397.

44. Shen, Z., et al., *Black silicon on emitter diminishes the lateral electric field and enhances the blue response of a solar cell by optimizing depletion region uniformity.* Scripta Materialia, 2013. **68**(3): p. 199-202.

45. Peng, K., X. Wang, and S.-T. Lee, *Silicon nanowire array photoelectrochemical solar cells.* Applied Physics Letters, 2008. **92**(16): p. 163103.

46. Pralle, M., et al. *Black silicon enhanced photodetectors: a path to IR CMOS*. in *SPIE Defense, Security, and Sensing*. 2010. International Society for Optics and Photonics.

47. Gaburro, Z., et al. *Multiparametric sensor for air pollutants based on a porous silicon optical microcavity*. in *Mater. Res. Soc. Symp Proc*. 2000. Cambridge Univ Press.

48. Hsu, C.-H., et al., *Fabrication and characteristics of black silicon for solar cell applications: An overview.* Materials Science in Semiconductor Processing, 2014.

49. Neudeck, G.W. and R.F. Pierret, *Introduction to Microelectronic Fabrication.* Modular Series on Solid State Devices, 2002. **5**.

50. Zhuang, D. and J.H. Edgar, *Wet etching of GaN, AlN, and SiC: a review.* Materials Science and Engineering: R: Reports, 2005. **48**(1): p. 1-46.

51. Li, X., *Metal assisted chemical etching for high aspect ratio nanostructures: A review of characteristics and applications in photovoltaics.* Current Opinion in Solid State and Materials Science, 2012. **16**(2): p. 71-81.

52. Yuan, H.-C., et al. *Antireflection and SiO 2 surface passivation by liquid-phase chemistry for efficient black silicon solar cells*. in *Photovoltaic Specialists Conference (PVSC), 2012 38th IEEE*. 2012. IEEE.

53. Peng, K., et al., *Motility of metal nanoparticles in silicon and induced anisotropic silicon etching.* Advanced Functional Materials, 2008. **18**(19): p. 3026-3035.

54. Peng, K., et al., *Fabrication of Single ‐Crystalline Silicon Nanowires by Scratching a Silicon Surface with Catalytic Metal Particles.* Advanced Functional Materials, 2006. **16**(3): p. 387-394.

55. Tsuboi, T., T. Sakka, and Y.H. Ogata, *Metal deposition into a porous silicon layer by immersion plating: Influence of halogen ions.* Journal of applied physics, 1998. **83**(8): p. 4501-4506.

56. Kayahan, E., N. Ceylan, and K. Esmer, *Ag-metallization effects on optical and electrical properties of porous silicon.* Applied Surface Science, 2008. **255**(5): p. 2808-2812.

57. Li, X. and P. Bohn, *Metal-assisted chemical etching in HF/H 2 O 2 produces porous silicon.* Applied Physics Letters, 2000. **77**(16): p. 2572-2574.

58. Bastide, S., et al., *Chemical etching of Si by Ag nanocatalysts in HF ‐ H2O2: application to multicrystalline Si solar cell texturisation.* physica status solidi (c), 2009. **6**(7): p. 1536-1540.

59. Lu, Y.-T. and A.R. Barron, *Nanopore-type black silicon anti-reflection layers fabricated by a one-step silver-assisted chemical etching.* Physical Chemistry Chemical Physics, 2013. **15**(24): p. 9862-9870.

60. Sökmen, Ü., et al., *Capabilities of ICP-RIE cryogenic dry etching of silicon: review of exemplary microstructures.* Journal of Micromechanics and Microengineering, 2009. **19**(10): p. 105005.

61. Yoo, J., G. Yu, and J. Yi, *Black surface structures for crystalline silicon solar cells.* Materials Science and Engineering: B, 2009. **159**: p. 333-337.

62. Ambrico, M., et al., *Melanin-like polymer layered on a nanotextured silicon surface for a hybrid biomimetic interface.* Journal of Materials Chemistry C, 2014. **2**(3): p. 573-582.

63. Lee, K.-s., et al., *Damage-free reactive ion etch for high-efficiency large-area multi-crystalline silicon solar cells.* Solar Energy Materials and Solar Cells, 2011. **95**(1): p. 66-68.

64. Ohring, M., *Materials science of thin films*. 2001: Academic press.

65. Xia, Y., et al., *A novel method to produce black silicon for solar cells.* Solar Energy, 2011. **85**(7): p. 1574-1578.

66. Chu, P.K., *Recent developments and applications of plasma immersion ion implantation.* Journal of Vacuum Science & Technology B, 2004. **22**(1): p. 289-296.

67. Ghoshal, T., et al., *"In situ" hard mask materials: a new methodology for creation of vertical silicon nanopillar and nanowire arrays.* Nanoscale, 2012. **4**(24): p. 7743-7750.

68. Bi, Y., et al., *Plasma-etching fabrication and properties of black silicon by using sputtered silver nanoparticles as micromasks.* Thin Solid Films, 2012. **521**: p. 176-180.

69. Her, T.-H., et al., *Femtosecond laser-induced formation of spikes on silicon.* Applied Physics A, 2000. **70**(4): p. 383-385.

70. Bonse, J., et al., *Femtosecond laser ablation of silicon–modification thresholds and morphology.* Applied Physics A, 2002. **74**(1): p. 19-25.

71. Tull, B.R., et al., *Silicon surface morphologies after femtosecond laser irradiation.* Mrs Bulletin, 2006. **31**(08): p. 626-633.

72. Radu, C., et al., *Silicon structuring by etching with liquid chlorine and fluorine precursors using femtosecond laser pulses.* Journal of Applied Physics, 2011. **110**(3): p. 034901.

73. Van Noort, R. and M. Black, *Silicone rubbers for medical applications.* Biocompatibility of clinical implant materials, 1981. **2**: p. 79-798.

74. Gallardo, M.R. and L.E. Long, *Electrically conductive black silicone paint having spacecraft applications*. 1997, Google Patents.

75. Oh, J., et al., *Nanoporous black silicon photocathode for H 2 production by photoelectrochemical water splitting.* Energy & Environmental Science, 2011. **4**(5): p. 1690-1694.

76. ; Available from: http://en.wikipedia.org/wiki/Terahertz_radiation.

77. Overton, G., *TERAHERTZ TECHNOLOGY Black silicon emits terahertz radiation*. 2008, PENNWELL PUBL CO 98 SPIT BROOK RD, NASHUA, NH 03062-2801 USA.

78. Xiao, Z., et al. *Formation of Silicon Nanopores and Nanopillars by a Maskless Deep Reactive Ion Etching Process*. in *Solid-State Sensors, Actuators and Microsystems Conference, 2007. TRANSDUCERS 2007. International*. 2007. IEEE.

79. Koynov, S., M.S. Brandt, and M. Stutzmann, *Black multi‐crystalline silicon solar cells.* physica status solidi (RRL)-Rapid Research Letters, 2007. **1**(2): p. R53-R55.

80. Parkinson, B. and J. Turner, *The Potential Contribution of Photoelectrochemistry in the Global Energy Future.* Photoelectrochemical Water Splitting: Materials, Processes and Architectures, 2013. **9**: p. 1.

81. Yeo, C., et al., *Antireflective silicon nanostructures with hydrophobicity by metal-assisted chemical etching for solar cell applications.* Nanoscale research letters, 2013. **8**(1): p. 1-7.

82. Li, X., et al., *Upgraded Silicon Nanowires by Metal‐Assisted Etching of Metallurgical Silicon: A New Route to Nanostructured Solar‐Grade Silicon.* Advanced Materials, 2013. **25**(23): p. 3187-3191.

83. Zhong, S., et al., *Influence of the texturing structure on the properties of black silicon solar cell.* Solar Energy Materials and Solar Cells, 2013. **108**: p. 200-204.

84. Xiu, Y., et al., *Hierarchical silicon etched structures for controlled hydrophobicity/superhydrophobicity.* Nano letters, 2007. **7**(11): p. 3388-3393.

85. Reece, S.Y., et al., *Wireless solar water splitting using silicon-based semiconductors and earth-abundant catalysts.* Science, 2011. **334**(6056): p. 645-648.

86. Mohamed, R. and E. Aazam, *Effect of Sn loading on the photocatalytic aniline synthesis activity of TiO< sub> 2</sub> nanospheres.* Journal of Alloys and Compounds, 2014. **595**: p. 8-13.

87. Xu, R., et al., *Shape‐dependent catalytic activity of silver nanoparticles for the oxidation of styrene.* Chemistry – An Asian Journal, 2006. **1**(6): p. 888-893.

88. Subramanian, V., E.E. Wolf, and P.V. Kamat, *Catalysis with TiO2/gold nanocomposites. Effect of metal particle size on the Fermi level equilibration.* Journal of the American Chemical Society, 2004. **126**(15): p. 4943-4950.

89. Halima, A., U. Rana, and D. MacFarlane, *Boron-Doped Diamond (BDD) Coatings Protect Underlying Silicon in Aqueous Acidic Media–Application to the Hydrogen Evolution Reaction.* Electrochimica Acta, 2014. **115**: p. 639-643.

90. Lewerenz, H.-J. and L. Peter, *Photoelectrochemical Water Splitting: Materials, Processes and Architectures*. Vol. 9. 2013: Royal Society of Chemistry.

91. Wang, J., et al., *Incorporation of Pt Particles in Boron-Doped Diamond Thin Films Applications in Electrocatalysis.* Electrochemical and Solid-State Letters, 2000. **3**(6): p. 286-289.

92. Gao, J.-S., et al., *Preparation and Characterization of Metal Nanoparticles on a Diamond Surface.* Chemistry of Materials, 2000. **12**(11): p. 3495-3500.

93. Kye, J., et al., *Platinum Monolayer Electrocatalyst on Gold Nanostructures on Silicon for Photoelectrochemical Hydrogen Evolution.* ACS Nano, 2013. **7**(7): p. 6017-6023.

94. Oh, I., J. Kye, and S. Hwang, *Enhanced Photoelectrochemical Hydrogen Production from Silicon Nanowire Array Photocathode.* Nano Letters, 2011. **12**(1): p. 298-302.

95. Shand, M. and J.A. Anderson, *Aqueous phase photocatalytic nitrate destruction using titania based materials: routes to enhanced performance and prospects for visible light activation.* Catalysis Science & Technology, 2013. **3**(4): p. 879-899.

96. Ashokkumar, M., *An overview on semiconductor particulate systems for photoproduction of hydrogen.* International Journal of Hydrogen Energy, 1998. **23**(6): p. 427-438.

97. Zhu, H., et al., *Mechanism of supported gold nanoparticles as photocatalysts under ultraviolet and visible light irradiation.* Chem. Commun., 2009(48): p. 7524-7526.

98. Youn, N.K., et al., *The effect of dissolved oxygen on the 1, 4-dioxane degradation with TiO< sub> 2</sub> and Au–TiO< sub> 2</sub> photocatalysts.* Journal of hazardous materials, 2010. **177**(1): p. 216-221.

99. Jakob, M., H. Levanon, and P.V. Kamat, *Charge distribution between UV-irradiated TiO2 and gold nanoparticles: determination of shift in the Fermi level.* Nano Letters, 2003. **3**(3): p. 353-358.

100. Soares, O., et al., *Photocatalytic nitrate reduction over Pd–Cu/TiO< sub> 2</sub>.* Chemical Engineering Journal, 2014. **251**: p. 123-130.

101. Wu, J.-M. and T.-W. Zhang, *Photodegradation of rhodamine B in water assisted by titania films prepared through a novel procedure.* Journal of Photochemistry and Photobiology A: Chemistry, 2004. **162**(1): p. 171-177.

102. Qu, P., et al., *TiO< sub> 2</sub>-assisted photodegradation of dyes: A study of two competitive primary processes in the degradation of RB in an aqueous TiO< sub> 2</sub> colloidal solution.* Journal of Molecular Catalysis A: Chemical, 1998. **129**(2): p. 257-268.

103. Wilhelm, P. and D. Stephan, *Photodegradation of rhodamine B in aqueous solution via SiO< sub> 2</sub>@ TiO< sub> 2</sub> nano-spheres.* Journal of Photochemistry and Photobiology A: Chemistry, 2007. **185**(1): p. 19-25.

104. Minh Hiep, H., et al., *A localized surface plasmon resonance based immunosensor for the detection of casein in milk.* Science and Technology of Advanced Materials, 2007. **8**(4): p. 331-338.

105. Lang, X., et al., *Localized surface plasmon resonance of nanoporous gold.* Applied Physics Letters, 2011. **98**(9): p. 093701.

106. Ghosh, S.K. and T. Pal, *Interparticle coupling effect on the surface plasmon resonance of gold nanoparticles: from theory to applications.* Chemical Reviews, 2007. **107**(11): p. 4797-4862.

Chapter Three

Nanostructured photoelectrochemical solar cell for nitrogen reduction using plasmon-enhanced black silicon

3.1 Introduction

Nitrogen reduction to ammonia at ambient conditions is the main point of interest in this thesis. Working in these conditions restricts the capability to reduce the highly inert and stable molecular nitrogen. The semiconductor developed in the previous chapter (b-Si+GNP) showed significant superiority in the preliminary tests, due to its characteristics. The black silicon absorbs light substantially more than plain silicon. Also, the surface physical configuration (nanospikes) promotes charge separation.

Surface decoration with GNP escalated the light absorbance and light trapping by activating the plasmonic effect in a valued addition to the already high absorbance of b-Si. Also, these nanoparticles served as an electron sink attracting electrons away from semiconductor and decreasing the electron-hole recombination rate, catalysing the reduction reaction.

In this chapter, the working bSi+GNP device was further developed by attaching Cr(III) to the back of the cell to act as a sacrificial agent acting as a hole collector by donating electrons to replace the electrons used in the reduction reaction. Cr(III) addition thereby improves the efficiency and sustainability of the process and allows extended experiments. Also, introducing a sacrificial agent (H_2SO_3) allows the direct formation of ammonium sulphate $(NH_4)_2SO_4$. These sacrificial agents allow for a stable yield production in 24h experiments.

A variety of light intensity (generated by a solar simulator), were tested to find the optimum and nitrogen pressure experiments were also conducted to explore the relation of

ammonia production and nitrogen diffusion rates. This work was published in *Nature Communications* in 2016.

3.2 Nanostructured photoelectrochemical solar cell for nitrogen reduction using plasmon-enhanced black silicon (paper)

nature COMMUNICATIONS

ARTICLE

Received 17 Nov 2015 | Accepted 16 Mar 2016 | Published 20 Apr 2016

DOI: 10.1038/ncomms11335 OPEN

Nanostructured photoelectrochemical solar cell for nitrogen reduction using plasmon-enhanced black silicon

Muataz Ali[1], Fengling Zhou[1], Kun Chen[1], Christopher Kotzur[1], Changlong Xiao[1], Laure Bourgeois[2], Xinyi Zhang[1] & Douglas R. MacFarlane[1]

Ammonia (NH_3) is one of the most widely produced chemicals worldwide. It has application in the production of many important chemicals, particularly fertilizers. It is also, potentially, an important energy storage intermediate and clean energy carrier. Ammonia production, however, mostly uses fossil fuels and currently accounts for more than 1.6% of global CO_2 emissions (0.57 Gt in 2015). Here we describe a solar-driven nanostructured photoelectrochemical cell based on plasmon-enhanced black silicon for the conversion of atmospheric N_2 to ammonia producing yields of 13.3 mg m^{-2} h^{-1} under 2 suns illumination. The yield increases with pressure; the highest observed in this work was 60 mg m^{-2} h^{-1} at 7 atm. In the presence of sulfite as a reactant, the process also offers a direct solar energy route to ammonium sulfate, a fertilizer of economic importance. Although the yields are currently not sufficient for practical application, there is much scope for improvement in the active materials in this cell.

[1] School of Chemistry, Monash University, Clayton, Victoria 3800, Australia. [2] Monash Centre for Electron Microscopy, Department of Materials Engineering, Monash University, Clayton, Victoria 3800, Australia. Correspondence and requests for materials should be addressed to D.M. (email: douglas.macfarlane@monash.edu) or to X.Z (email: xinyi.zhang@monash.edu).

Ammonia production is a highly energy intensive process, consuming 1–3% of the world electrical energy and ~5% of the world natural gas production[1,2]. World production is around 200 million tonnes annually[2,3], reflecting the vast need for this chemical in agriculture, pharmaceutical production and many other industrial processes. Ammonia is also being considered as a carbon-free solar energy storage material, due to its useful characteristics as a chemical energy carrier. Compared with other chemicals that could be used to store solar energy (such as hydrogen), ammonia is safe, ecofriendly and, most importantly, produces no CO_2 emissions[4]. Apart from the well-known industrial Haber–Bosch process, there are a number of other chemical, electrochemical and biological production methods[5–9]. Among them, an electrochemical method is of considerable interest because it can be coupled with hydro, wind, solar or nuclear energy. The electrochemical reduction of nitrogen largely depends on the structure, components and surface morphology of the electrocatalyst[10]. Polyaniline electrodes have been investigated in methanol/$LiClO_4/H^+$ solution, achieving a maximum current efficiency of 16% at −0.12 V (versus standard hydrogen electrode (NHE)) at room temperature and elevated pressure[11]. By using a membrane electrode assembly based cell with Pt electrodes, an ammonia production rate of 1.14×10^{-5} mol m^{-2} s^{-1} has been achieved from air and water at ambient temperature and pressure at an overall cell voltage of 1.6 V (ref. 12). By using the mixture of air and steam in a molten hydroxide suspension of nano-Fe_2O_3, ammonia has also been produced at a cell voltage of 1.2 V at coulombic efficiency of 35% (ref. 13). Although this advance shows a great promise in competing with current ammonia industry, the high temperature (~200 °C) used still requires extra input of heat and energy. Thus, there is intense interest in new catalysts for nitrogen reduction processes and alternative means of carrying out the reaction[14–16].

Photochemical conversion provides a promising approach to convert nitrogen into ammonia by using solar energy. Early attempts used titania, or modified titania semiconductor catalysts[17–19], but all of these produced only impractically low efficiencies. The recent development of surface plasmon resonance (SPR) has provided some new opportunities. Plasmon-induced ammonia synthesis has been demonstrated through nitrogen photofixation on a gold nanoparticle (GNP) -coated Nb-$SrTiO_3$ substrate with visible light irradiation[20]. Photo-illuminated diamond has also been used as a solid-state source of solvated electrons in water for nitrogen reduction[21]. Photochemical nitrogen conversion to ammonia has been achieved on chalcogels containing FeMoS inorganic clusters in ambient conditions; the significance of this work lies in that Fe and Mo are two key metals found in nitrogenases that catalyse nitrogen reduction in nature[22]. More recently, oxygen vacancies of BiOBr nanosheets have been investigated for nitrogen reduction; this work in particular offers improved yields, but suffers from a decreasing photo-reactivity due to the quench of oxygen vacancies[23].

Black silicon (bSi) is a form of silicon in which its surface is covered by a layer of nanostructures (usually nanowires, nanorods or nanotips), which effectively suppresses reflection, by enhancing the scattering and absorption of light. As a consequence, the silicon wafers appear black, instead of the silver-grey typical of planar silicon wafers. bSi possesses many attractive properties, including low reflectance, a large and chemically active surface area, super-hydrophobicity, and a high luminescence efficiency when surface-feature sizes are reduced to a few nanometers[24–26]. In this work we have achieved solar light driven conversion of nitrogen to ammonia using a photoelectrochemical structure, based on plasmon-enhanced bSi, as the photo absorber, decorated with GNPs as the reduction catalysis sites and a hole-sink layer of Cr. This multi-layer structure creates an autonomous electrochemical device capable of carrying out oxidation and reduction reactions on different areas of the device, powered by photo-excitation.

Results

Fabrication of the photoelectrochemical cell. A schematic illustration of the fabrication steps and working mechanism of the photoelectrochemical cell and corresponding scanning electron micrograph and transmission electron micrographs are shown in Fig. 1 and Supplementary Figs 1 and 2. A p-type boron-doped commercial <100> silicon wafer was used as a substrate material. bSi was fabricated using a dry etching method. A GNP layer was then sputtered onto the etched surface as the photocathode. Finally, a Cr layer with thickness ~50 nm was sputtered onto the back surface of the silicon wafer as an anode. Full experimental detail is provided in Methods section.

Photoelectrochemical reduction of nitrogen. A nitrogen photo-reduction cell was constructed (Fig. 2a) with nitrogen gas bubbling over the surface of the material and artificial solar light (300 W Xe lamp) as an illumination source. The yield of

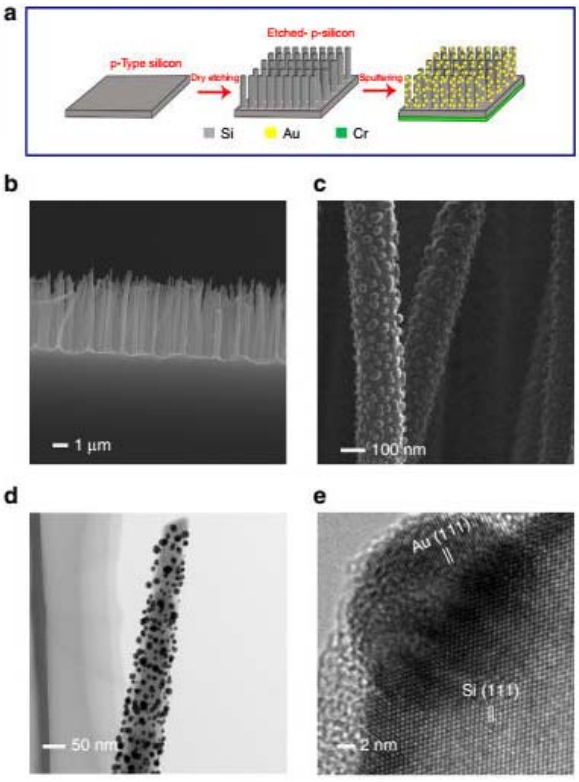

Figure 1 | Schematic of fabrication and SEM and TEM images of the electrodes. (**a**) Schematic illustration of fabrication of the cell. (**b**) Cross-sectional view and (**c**) magnified view of SEM images of GNPs-coated black silicon nanostructure. (**d**) Corresponding TEM and (**e**) HRTEM images of GNPs-coated silicon nanowire. The well-resolved lattice spacings of 0.31 and 0.23 nm correspond to the Si {111} and Au {111} atomic planes, respectively. SEM, scanning electron micrograph; HRTEM, high-resolution TEM; TEM, transmission electron micrograph.

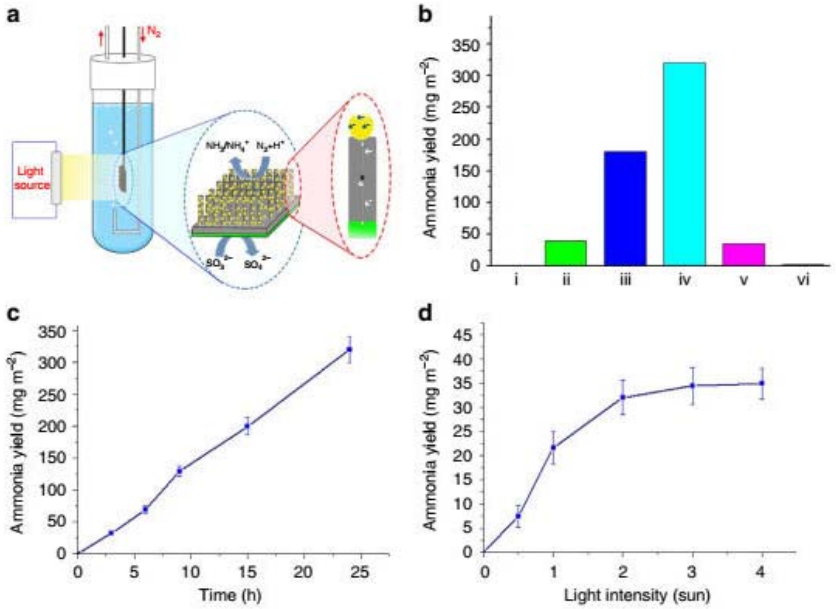

Figure 2 | Photoelectrochemical nitrogen reduction. (**a**) Schematic diagram of the cell. (**b**) Yield of ammonia over 24 h obtained on different substrates: (i) P-type silicon, (ii) bSi, (iii) GNP/bSi, (iv) GNP/bSi/Cr and (v) Au/Si/Cr after illumination with two suns and (vi) GNP/bSi/Cr in dark. (**c**) The time-dependence of ammonia yield obtained after illumination with two suns (error bars are the s.d. of at least three replicates of independent measurement). (**d**) The light intensity-dependence of ammonia yield obtained after illumination for 3 h (error bars are an estimate of the combined errors of measurements).

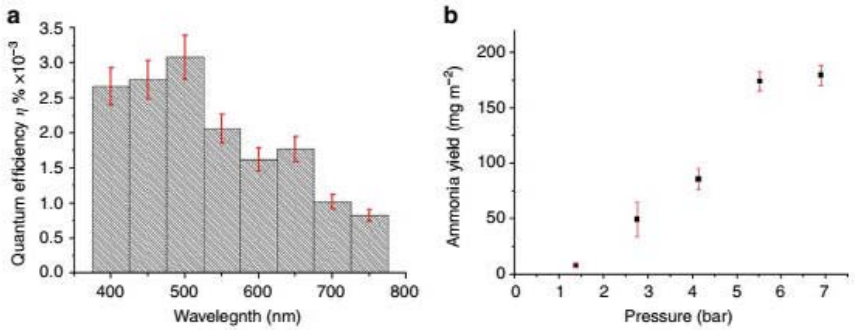

Figure 3 | Quantum efficiency and high-pressure yield obtained on a GNP/bSi/Cr photoelectrochemical cell. (**a**) Quantum efficiency of ammonia synthesis on a GNP/bSi/Cr photoelectrochemical cell as a function of wavelength (error bars are estimates of the combined errors of measurements). (**b**) Yield of ammonia in three hours as a function of nitrogen gas pressure at two suns illumination in a fixed volume glass reactor (error bars are the s.d. of at least three replicates of independent measurement).

ammonia was measured by using an ammonia/ammonium ISE and the indophenol method[27].

Control experiments were conducted in H_2O (18.2 MΩ cm). Yields obtained over a 24 h period are shown in Fig. 2b. Ammonia production can be observed at a low level on bSi; however, after coating with GNPs, the yield of ammonia is increased by nearly four times. To avoid silicon oxidation and enhance charge separation, a Cr layer was coated on silicon to act as the hole-sink and anode; in other words, Cr facilitates hole collection from the Si and acts in this case as a sacrificial anode. This GNP/bSi/Cr photoelectrochemical cell exhibits yield of 320 mg m^{-2} over 24 h. However, the oxidation of Cr was also observed, confirming its role as a sacrificial hole-sink in the process. To avoid the loss of Cr, sodium sulfite was added to the electrolyte used to provide an alternate electron donor to scavenge the photogenerated holes and hence protect the Cr anode. Ammonia production as a function of time with this GNP/bSi/Cr/sulfite structure is shown in Fig. 2c; the final yield of ammonia under these conditions over a 24 h period was 320 mg m^{-2} or 13.3 mg m^{-2} h^{-1}. A durability test consisting of repeated 3 h runs using this sodium sulfite electrolyte also showed very reproducible and stable behaviour for up to 18 h (Supplementary Fig. 3). These results show that the GNP/bSi/Cr cell exhibits excellent activity and stability for ammonia production compared with previous reports, as summarized in Supplementary Table 1. A control experiment was also performed to confirm that the source of the nitrogen in the ammonia was the bubbled N_2, by using Ar to replace N_2 in the experiment; no ammonia was detected (Supplementary Fig. 4).

While a number of possible sacrificial reagents could be used in this context, sulfite was chosen on the basis that, when used in its aqueous acid form, the product of the overall reaction can be

ammonium sulfate: $N_2 + 3H_2SO_3 + 3H_2O \rightarrow 2H_2SO_4 + (NH_4)_2SO_4$. Equivalent reactions can use potassium or ammonium bisulfite in this process (as described in Supplementary Note 1). The final 24 h yield in terms of ammonium sulfate as a product corresponds to 1.24 g m^{-2}. Since the production rate appears to be quite constant over the 24 h period of the experiments in Fig. 2c, it would appear that this yield is not limited by product buildup under these conditions (Supplementary Fig. 5). The effect of light intensity is shown in Fig. 2d, the ammonia yield increases linearly with the intensity of light up to 300 mW cm^{-2} and then plateaus. This limiting rate is likely to be related to factors such as the rates of mass transport of the reactants and products at the active surfaces.

Quantum yield experiments (Fig. 3a) were carried out with 50-nm-wide bandpass filters, confirming that the nitrogen reduction can occur in whole visible range, dropping away as the band gap energy of Si is approached. A small absorption maximum that is observed in the region of the SPR region for GNPs (Supplementary Fig. 6) also appears in the region of 500 nm in Fig. 3a. This suggests that excitation of surface plasmons in the GNP particles provides an additional photo-excitation mechanism that contributes to the overall yield in this region of the spectrum, as has been observed in other SPR-enhanced processes[28,29]. To understand the relationship between the dissolved amounts of nitrogen in the solution and the generated ammonia-ammonium yield, the effect of N_2 pressure on the reaction was investigated in a closed glass pressure vessel (Fig. 3b). An approximately linear dependence of yield on pressure was observed over the range studied, and the yield was 60 mg m^{-2} h^{-1} at 7 atm, as would be expected from a Henry's law dependence of nitrogen solubility on pressure in the aqueous medium. This suggests that the concentration of nitrogen at the reactive sites on the surface is a rate limiting factor in these experiemnts. On the other hand, in our ambient condition experiments, bubbling nitrogen gas generates strong agitation of the medium created near the surface as well as a dynamic gas–liquid–solid interface, which enhances reactions rates by facilitating transport to and from the reaction sites in the strucure (this also explains the relatively lower yields at lower pressures in Fig. 3b). This suggests that strategies to further enhance yield in either case could seek to enhance the kinetics of these processes via further manipulation of the nanostructure of the bSi.

Discussion

The various reference experiments in Fig. 2b reveal the roles of each layer in the overall reaction process, as illustrated in Supplementary Fig. 7. When the bSi was replaced by unetched pristine silicon, the ammonia yield was only ~11% of that produced by the GNP/bSi/Cr structure. bSi effectively suppresses reflection, while simultaneously enhancing the scattering and absorption of light. bSi also provides an extremely large surface area for decoration by the GNPs. High activities of silicon nanostructures have been demonstrated previously in both photoelectrolytic and chemical water splitting[30,31]. The GNP-coated bSi material shows much superior ammonia yield over bSi alone, revealing the functions of the GNPs in separating charge and as an electrocatalytic site for the N_2 reduction reaction. Meanwhile, bSi facilitates hole transfer to the anode layer (Cr) to execute the oxidation reactions. After coating with Cr on the backside, the ammonia production of the GNP/bSi/Cr cell increases to about two times that of GNP/bSi and eight times that of pure bSi. The detailed reduction mechanism of N_2 to NH_3, which involves six electrons and six protons, is not yet well-understood and is the focus of ongoing experimental and theoretical investigations by a number of groups[6,10,32], including ourselves. It is important to note that the overall reaction in the dark with sulfite is not spontaneous, as indicated by the free energy calculation shown in the Supplementary Note 2. This confirms that role of the cell is energy injection into the process, as opposed to photo-catalytic. It is worth noting that sulfite is a product of coal-fired power station flue gas scrubbing, while ammonium sulfate is a commonly used form of ammonia as a fertilizer. So this autonomous photoelectrochemical process may offer scope to valorize this otherwise hazardous waste product.

In summary, we describe a nanostructured photo-electrochemical cell that is capable of mimicking the nitrogen fixation and conversion process of nitrogenases in nature and producing ammonia (13.3 mg m^{-2} h^{-1}, at 2 suns) and an ammonia based fertilizer in a fully solar-driven process. The photoelectrochemical cell is not inherently area limited and can be scaled up with the silicon wafer size, and the nanostructures of the cell can be further improved and optimized in term of the component, size and configuration. Hence significant potential exists for further development of this approach to ammonia generation by using standard manufacturing process. At this preliminary stage, the efficiency of our photoelectrochcmical process is still too low for practical ammonia manufacture. One of the possibilities to improve the efficiency is to couple our cell with a separate PV cell (as detailed further in Supplementary Table 2), since the configuration of our cell is ready to be utilized as an electrochemical cell. Finally, the combination of black silicon-based photo-adsorber and plasmonic catalysts described here could provide a pathway toward an unassisted solar-to-chemical conversion in many applications such as CO_2 fixation and water splitting.

Methods

Preparation and characterization of black silicon (bSi) and electrodes. A p-type boron-doped 100 mm commercial <100> silicon wafer (resistivity = 10–20 ohm cm) of 525 μm thickness (Atecom Ltd, Taiwan) was used as a substrate material for black silicon formation. The wafers were used as supplied. The dry etching process was carried out using an Oxford PlasmaLab 100 ICP380 system. The etching process was a mixed mode, wherein etching and passivation occurred at the same time. Process conditions for the black silicon formation were: SF_6 gas flow rate 65 s.c.c.m., O_2 gas flow rate 44 sccm, process pressure of 35 mTorr, 100 W reactive ion etching (RIE) power, 20 °C electrode temperature and 10 Torr He backside cooling pressure. The RIE process resulted in a homogeneously distributed silicon nanowire arrays with length about 3 μm across the full wafer after 20 min etching. Nitrogen adsorption–desorption experiments were performed at 77 K with a Micromeritics Tristar II. The samples were degassed at 200 C for 5 h before measurement. The surface area of bSi calculated from nitrogen sorption results by Brunauer–Emmett–Teller method is 10.4 cm^2. After the RIE process, the gold coating was carried out on a K550X sputter coater at 25 mA at 1×10^{-1} mbar. The discharge time was 4 min. The size of the GNPs ranges from 3 to 30 nm. The prepared bSi with GNP on its surface was back coated with chromium; the coating process was carried out using a high-resolution turbomolecular-pumped sputter coater, including a TK8845 54 mm Ø × 0.3 mm chromium (Cr) target (Q150T S Quorum Technologies). The coating conditions were 40 mA current density for 120 s (2 × 60 s). The morphology and structure of bSi were investigated by scanning electron microscopy (scanning electron micrograph, JEOL JSM-7100) and transmission electron microscopy (transmission electron micrograph, JEOL-2100F).

Photoelectrochemical nitrogen reduction. All of the chemical reagents in this study were of analytical grade and were supplied by Sigma-Aldrich (Australia).

A photo-reduction cell to reduce nitrogen into ammonia was constructed; the cell contained 10 ml deionized water or electrolyte as specified below and the nitrogen flow rate was 10 ml min^{-1}. Nitrogen was passed through the cell for 1 h to remove oxygen. Black silicon pieces with size of 10 × 10 mm^2 were tested. The artificial solar light source was a 300 W Xe lamp, while the illumination intensity used was 2 suns unless otherwise specified. The experimental conditions were as follows: *bSi (dark)*: black silicon, (reaction conditions; 10 ml deionized water, in dark). *Si*: pristine unetched silicon (reaction conditions; 10 ml deionized water, 2 suns). *GNP/bSi*: GNPs-coated black silicon, (reaction conditions; 10 ml deionized water, 2 suns). *GNP/bSi/Cr*: GNPs-coated black silicon (front) and chromium (back) (reaction conditions; 10 ml deionized water, 2 suns). *bSi/GNP/Cr + SO3 − 2*: GNPs-coated black silicon (front) and chromium (back), (reaction conditions; in 10 ml 150 p.p.m. sodium sulfite electrolyte, 2 suns). *GNP/Si/Cr*: GNPs-coated

pristine unetched silicon (front) and chromium (back) (reaction conditions; 10 ml deionized water, 2 suns). *GNP/bSi/Cr(dark)*: GNPs-coated black silicon (front) and chromium (back) (reaction conditions; 10 ml deionized water, in dark). The cell solution was analysed directly for its ammonia content. The exiting nitrogen gas stream was bubbled through a water filled collector vessel to trap any ammonia carried by the nitrogen for analysis; the fraction appearing in the collector vessel was typically ~12% and was included in the overall NH_3 yield results of GNP/bSi/Cr cell in sodium sulfite electrolyte.

High-pressure experiments. The p-GNP/bSi/Cr was tested under high-pressure nitrogen gas using a Q-tube purging-35-SS vessel, purchased from Q Labtech. The reaction was carried out under irradiation using a 300 W Xe lamp with the intensity equivalent to 2 suns. The electrolyte used was 10 ml deionized water and the catalyst size 1 cm^2 (0.12 g). The electrolyte was bubbled with nitrogen for 20 min followed by addition to the reaction vessel which was purged with nitrogen gas before irradiation. Following irradiation for 3 h the concentration of ammonia/ammonium was analysed.

Ammonia analysis. Ammonia products were analysed by using (i) an ammonia/ammonium ISE (YSI, 6883) and (ii) the indophenol method[33]. The YSI probe was calibrated using standard ammonia solutions containing the sacrificial agent (at concentration lower than electrode manufacturer's salinity limit). To ensure that the added SO_3^{2-} did not interfere with the ammonia analysis methods in this work, the ISE was recalibrated using standard solutions containing the same amount of sacrificial agent (Supplementary Fig. 8). The indophenol method was used as a confirmation of the final yield of each experiment (supplementary Fig. 9). The UV–vis absorption peak of indophenol appears at ~630 nm. At higher concentrations near the UV–vis spectrophotometer absorption limit, samples were diluted to $\frac{1}{4}$ or $\frac{1}{2}$ of original concentration[34,35].

References

1. Jackson, R. B. *et al.* Reach peak emissions. *Nat. Clim. Change* **6,** 7–10 (2016).
2. Service, R. Chemistry. new recipe produces ammonia from air, water, and sunlight. *Science* **345,** 610 (2014).
3. Ceresana. Market Study: Ammonia (UC-3705) (2012).
4. Lan, R. & Tao, S. Ammonia as a suitable fuel for fuel cells. *Fuel Cells* **2,** 35 (2014).
5. Van Tamelen, E. E. & Akermark, B. Electrolytic reduction of molecular nitrogen. *J. Am. Chem. Soc.* **90,** 4492–4493 (1968).
6. Nguyen, M.-T., Seriani, N. & Gebauer, R. Nitrogen electrochemically reduced to ammonia with hematite: density-functional insights. *Phys. Chem. Chem. Phys.* **17,** 14317–14322 (2015).
7. Eady, R. R. Structure-function relationships of alternative nitrogenases. *Chem. Rev.* **96,** 3013–3030 (1996).
8. Reiher, M., Le Guennic, B. & Kirchner, B. Theoretical study of catalytic dinitrogen reduction under mild conditions. *Inorg. Chem.* **44,** 9640–9642 (2005).
9. Leigh, G. Fixing nitrogen any which way. *Science* **279,** 506–507 (1998).
10. van der Ham, C. J. M., Koper, M. T. M. & Hetterscheid, D. G. H. Challenges in reduction of dinitrogen by proton and electron transfer. *Chem. Soc. Rev.* **43,** 5183–5191 (2014).
11. Koleli, F. & Ropke, T. Electrochemical hydrogenation of dinitrogen to ammonia on a polyaniline electrode. *Appl. Catal. B* **62,** 306–310 (2006).
12. Lan, R., Irvine, J. T. S. & Tao, S. Synthesis of ammonia directly from air and water at ambient temperature and pressure. *Sci. Rep.* **3,** 1145 (2013).
13. Licht, S. *et al.* Ammonia synthesis by N_2 and steam electrolysis in molten hydroxide suspensions of nanoscale Fe_2O_3. *Science* **345,** 637–640 (2014).
14. Shima, T. *et al.* Dinitrogen cleavage and hydrogenation by a trinuclear titanium polyhydride complex. *Science* **340,** 1549–1552 (2013).
15. Rodriguez, M. M., Bill, E., Brennessel, W. W. & Holland, P. L. N_2 reduction and hydrogenation to ammonia by a molecular iron-potassium complex. *Science* **334,** 780–783 (2011).
16. Arashiba, K. *et al.* Catalytic reduction of dinitrogen to ammonia by use of molybdenum-nitride complexes bearing a tridentate triphosphine as catalysts. *J. Am. Chem. Soc.* **137,** 5666–5669 (2015).
17. Schrauzer, G. & Guth, T. Photocatalytic reactions. 1. Photolysis of water and photoreduction of nitrogen on titanium dioxide. *J. Am. Chem. Soc.* **99,** 7189–7193 (1977).
18. Ranjit, K., Varadarajan, T. & Viswanathan, B. Photocatalytic reduction of dinitrogen to ammonia over noble-metal-loaded TiO_2. *J. Photochem. Photobiol. A Chem.* **96,** 181–185 (1996).
19. Vettraino, M., Trudeau, M., Lo, A. Y., Schurko, R. W. & Antonelli, D. Room-temperature ammonia formation from dinitrogen on a reduced mesoporous titanium oxide surface with metallic properties. *J. Am. Chem. Soc.* **124,** 9567–9573 (2002).
20. Oshikiri, T., Ueno, K. & Misawa, H. Plasmon-induced ammonia synthesis through nitrogen photofixation with visible light irradiation. *Angew. Chem. Int.* **126,** 9960–9963 (2014).
21. Zhu, D., Zhang, L., Ruther, R. E. & Hamers, R. J. Photo-illuminated diamond as a solid-state source of solvated electrons in water for nitrogen reduction. *Nat. Mater.* **12,** 836–841 (2013).
22. Banerjee, A. *et al.* Photochemical nitrogen conversion to ammonia in ambient conditions with FeMoS-chalcogels. *J. Am. Chem. Soc.* **137,** 2030–2034.
23. Li, H., Shang, J., Ai, Z. & Zhang, L. Efficient visible light nitrogen fixation with BiOBr nanosheets of oxygen vacancies on the exposed {001} facets. *J. Am. Chem. Soc.* **137,** 6393–6399 (2015).
24. Hsu, C.-H. *et al.* Fabrication and characteristics of black silicon for solar cell applications: an overview. *Mater. Sci. Semicond. Process.* **25,** 2–17 (2014).
25. Oh, J., Yuan, H.-C. & Branz, H. M. An 18.2%-efficient black-silicon solar cell achieved through control of carrier recombination in nanostructures. *Nat. Nanotechnol.* **7,** 743–748 (2012).
26. Koynov, S., Brandt, M. S. & Stutzmann, M. Black nonreflecting silicon surfaces for solar cells. *Appl. Phys. Lett.* **88,** 203107 (2006).
27. Searle, P. L. The Berthelot or indophenol reaction and its use in the analytical chemistry of nitrogen. A review. *Analyst* **109,** 549–568 (1984).
28. Mubeen, S. *et al.* An autonomous photosynthetic device in which all charge carriers derive from surface plasmons. *Nat. Nanotechnol.* **8,** 247–251 (2013).
29. Linic, S., Christopher, P. & Ingram, D. B. Plasmonic-metal nanostructures for efficient conversion of solar to chemical energy. *Nat. Mater.* **10,** 911–921 (2011).
30. Wang, Y. *et al.* Silicon nanowires for biosensing, energy storage, and conversion. *Adv. Mater.* **25,** 5177–5195 (2013).
31. Erogbogbo, F. *et al.* On-demand hydrogen generation using nanosilicon: splitting water without light, heat, or electricity. *Nano Lett.* **13,** 451–456 (2013).
32. Christianson, J. R., Zhu, D., Hamers, R. J. & Schmidt, J. R. Mechanism of N_2 reduction to NH_3 by aqueous solvated electrons. *J. Phy. Chem. B* **118,** 195–203 (2013).
33. Harwood, J. E. & Kühn, A. L. A colorimetric method for ammonia in natural waters. *Water Res.* **4,** 805–811 (1970).
34. Scheiner, D. Determination of ammonia and Kjeldahl nitrogen by indophenol method. *Water Res.* **10,** 31–36 (1976).
35. Ivančič, I. & Degobbis, D. An optimal manual procedure for ammonia analysis in natural waters by the indophenol blue method. *Water Res.* **18,** 1143–1147 (1984).

Acknowledgements

This work was supported by the Australian Research Council through Grant No.: DP120104334 and through D.R.M.'s Australian Laureate Fellowship. This work was performed in part at the Melbourne Centre for Nanofabrication (MCN) in the Victorian Node of the Australian National Fabrication Facility (ANFF). The authors acknowledge the use of facilities at the Monash Centre for Electron Microscopy. M.A. is on leave from the Chemistry Department, Al-Nahrain University, Baghdad, Iraq.

Author contributions

D.R.M., X.Z and M.A. conceived the experiments. M.A., F.Z., C.X and C.K. performed the experiments. X.Z. prepared the GNP-coated black silicon. K.C. and L.B. performed electronic microscopic analysis. D.R.M., X.Z. and M.A. contributed in the interpretation of experiments. M.A., X.Z. and D.R.M. prepared the manuscript. All the authors discussed the results and commented on the manuscript.

Additional information

Supplementary Information accompanies this paper at http://www.nature.com/naturecommunications

Competing financial interests: The authors declare no competing financial interests.

Reprints and permission information is available online at http://npg.nature.com/reprintsandpermissions/

How to cite this article: Ali, M. *et al.* Nanostructured photoelectrochemical solar cell for nitrogen reduction using plasmon-enhanced black silicon. *Nat. Commun.* 7:11335 doi: 10.1038/ncomms11335 (2016).

3.3 Supplementary information

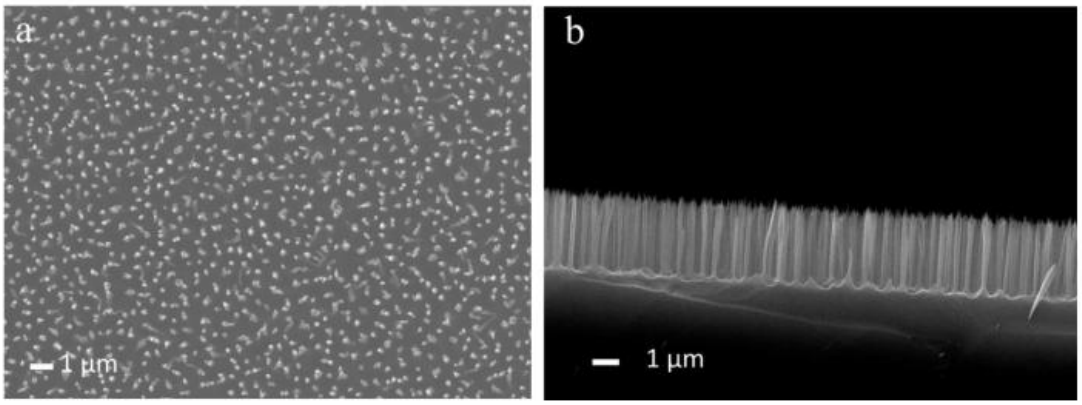

Supplementary Figure 1. SEM images of the bSi. (a) Plain view and (b) cross-sectional view.

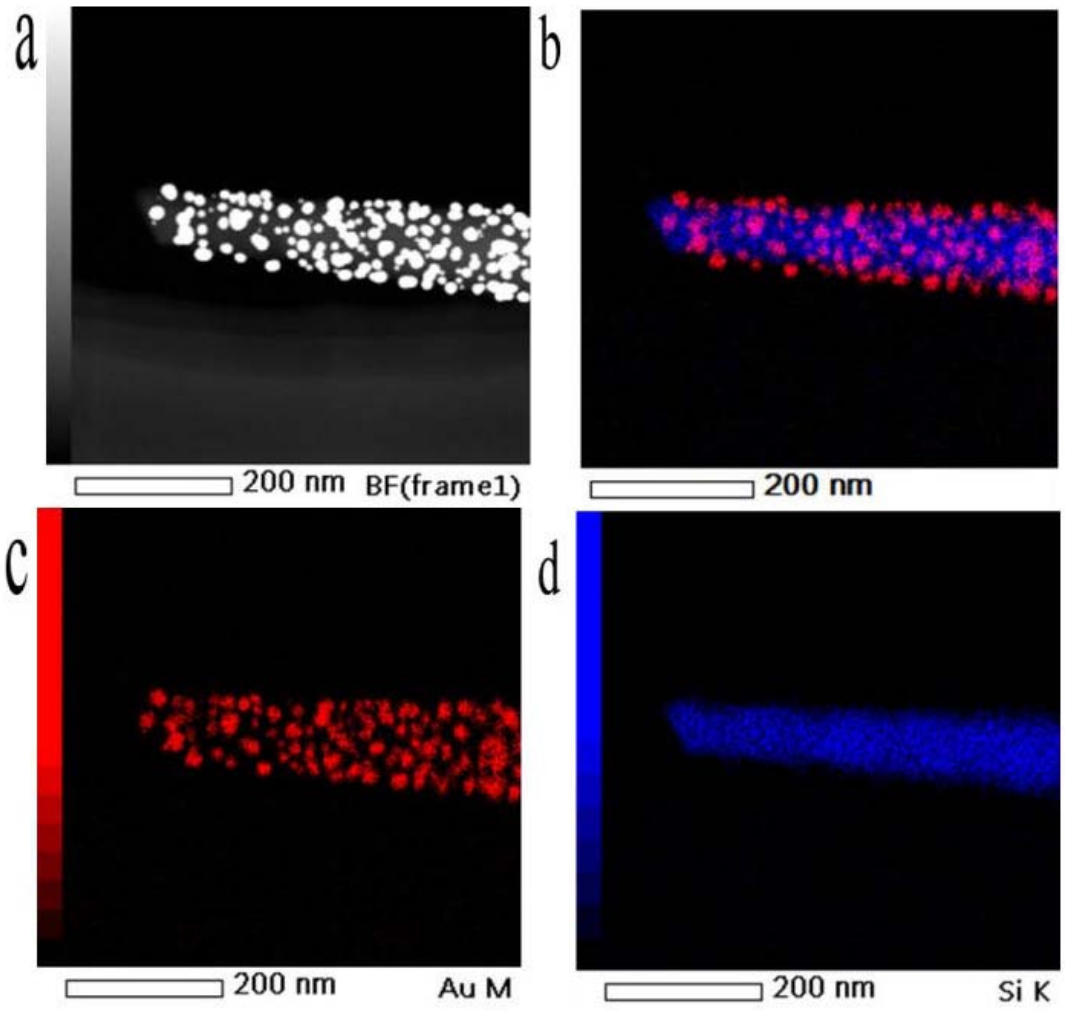

Supplementary Figure 2. (a) STEM and (b-d) EDX images of gold nanoparticles coated a silicon nanowire of the bSi.

2

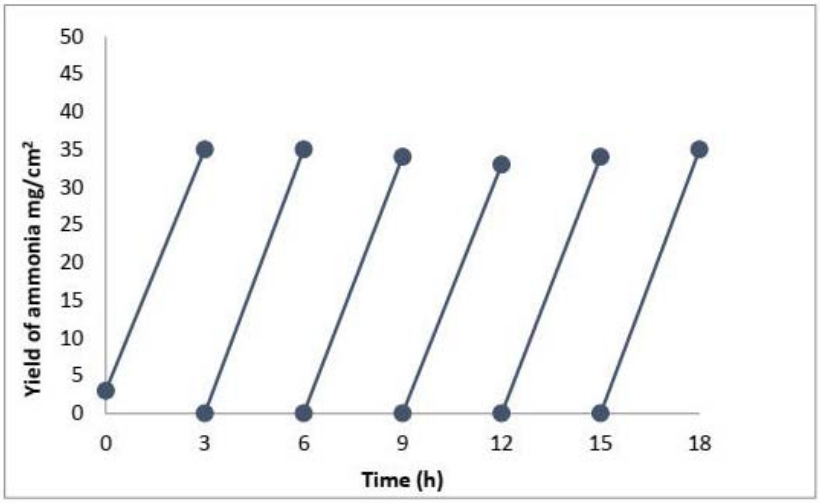

Supplementary Figure 3. Durability tests for the prepared catalysts. Blue points are for bSi/GNP/Cr sample with sulfite sacrificial agent. To ensure that depletion of the reactants or build-up of products did not affect the results, the solution has been replaced after each 3 hour period; the catalyst in this case remains stable over 6 cycles due to the action of the sacrificial agent in solution.

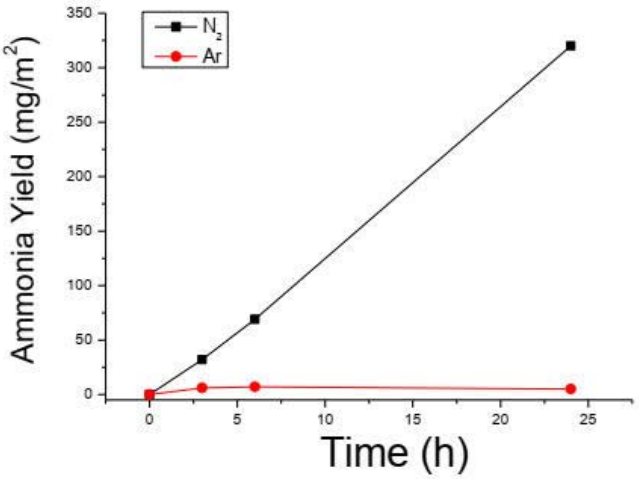

Supplementary Figure 4. Comparison of ammonia yields on GNP/bSi/Cr bubbled with (a) N_2 at 10 ml/min and (b) Ar at 10 ml/min. This control experiment confirms that the ammonia product is produced from the reduction of bubbled N_2.

4

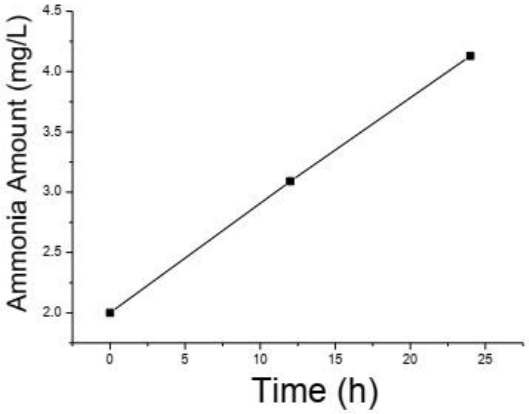

Supplementary Figure 5. The time-dependence of ammonia concentration obtained on GNP/bSi/Cr after illumination with 2 suns in solution containing 2 mg/L ammonia. This control experiment confirms that the photoelectrochemical cell can produce ammonia at constant rate even the ammonia concentration in the solution reaches certain level.

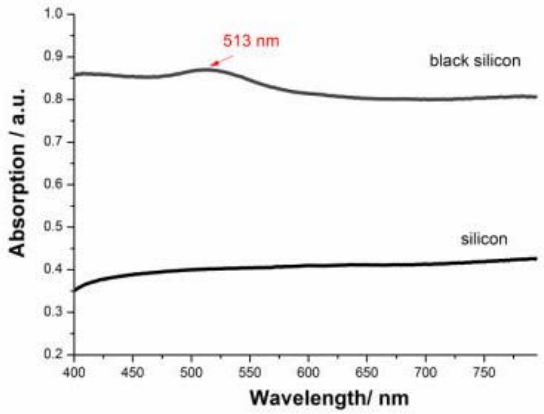

Supplementary Figure 6. UV-vis spectra of gold nanoparticle coated bSi compared with unetched Si. The difference in optical absorption is a result of the nano-structure modification created by the RIE.

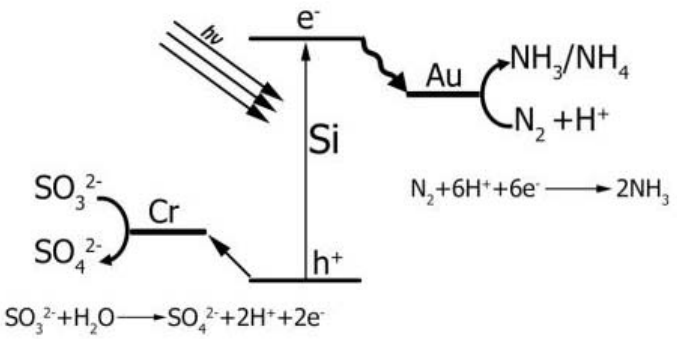

Supplementary Figure 7. Illustration of the electrochemical reaction processes.

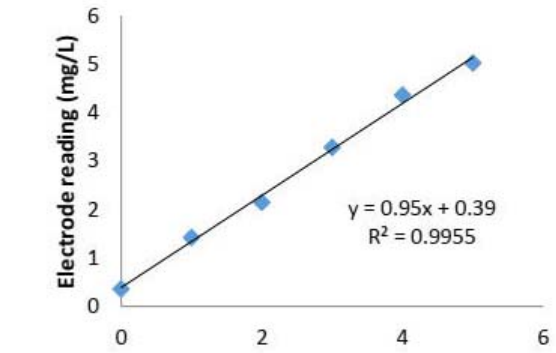

Supplementary Figure 8. Calibration curve of the YSI electrode against NH_3 standard solutions containing 150mg/L SO_3^{-2}.

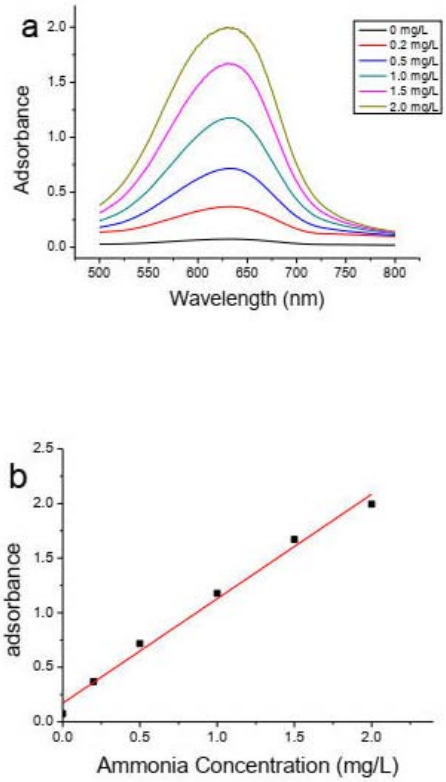

Supplementary Figure 9. (a) UV-Vis spectra for indophenol determination of standards ammonia. **(b)** Calibration curve obtained for standard ammonia solutions.

Supplementary Table1: Comparing ammonia yields in recent literature

year	paper	Absolute Yield (μmol)	Time (hour)	Type*	Reactor Vol. (ml)	Ref.
	This Work	1.88	24	I	10	
1994	Photocatalytic reduction of nitrogen over (Fe, Ru or Os)/TiO 2 catalysts	0.09	24	D	30	[1]
2013	Photo-illuminated diamond as a solid-state source of solvated electrons in water for nitrogen reduction	0.41	24	I	Not-mentioned	[2]
2013	Mechanism of N2 Reduction to NH3 by Aqueous Solvated Electrons	8.20×10^{-3}	24	D	10	[3]
2014	Plasmon - Induced Ammonia Synthesis through Nitrogen Photofixation with Visible Light Irradiation	6.00×10^{-3}	24	I	0.21	[4]
2015	Efficient visible light nitrogen fixation with BiOBr nanosheets of oxygen vacancies on the exposed {001} facets	5	1	D	100	[5]
2015	Photochemical Nitrogen Conversion to Ammonia in Ambient Conditions with FeMoS-Chalcogels	2.1	24	D	10	[6]

*(I): catalysts are immobilized on a substrate. (D): catalysts are dispersed and suspended in the solution. Units vary between journal articles, so, in order to minimize confusion, all the yields have been converted into μmol units. Other factors that effectively influence the yield calculation such as light intensity, yield physical shape (i.e., solid, gas), weight of semiconductor and physical shape of the catalyst, are all crucial when comparing the yield in different catalyst. The yield in this work is higher than the reported yields obtained on immobilized catalysts and highly competitive compared to the highest yields obtained by using dispersed photocatalysts.

Supplementary Table 2. Estimated maximum possible solar to NH_3 energy efficiencies according to reported data

To explore the possibility of coupling an electrolysis device with a separate PV cell, the following data from reports of recent electrochemical reduction reactions are combined with data for an appropriate PV cell that could drive the reaction. Since data for electrolysis inefficiencies are not available this data illustrates the maximum possible solar to ammonia energy efficiency in each case.

Ref (main text)	catalyst	media	T/°C	P/ bar	Potential needed	N_2 Faradaic Eff/%	PV system*	PV efficiency % (max)	Maximum Solar to NH3 energy efficiency (%)
10	Polyaniline	Methanol/ $LiClO_4$/H+	25	1	-0.12V vs NHE (three electrodes)	1.3	4 single junction c-Si cell	10	0.13
10	Polyaniline	Methanol/ $LiClO_4$/H+	25	50	-0.12V vs NHE (three electrodes)	16.3	4 single junction c-Si cell	10	1.63
11	Pt/Nafion 211 Membrane	H_2O/air	RT	1	1.6 V (two electrodes)	1	4 single junction c-Si cell	10	0.1
12	Ni/Fe_2O_3	NaOH/KOH	200	25	1.2 (two electrodes)	35	3 single junction c-Si cell	13	4.55

*: ref to; Banerjee, A. *et al.* Photochemical Nitrogen Conversion to Ammonia in Ambient Conditions with FeMoS-Chalcogels. *Journal of the American Chemical Society* **137**, 2030-2034 (2015).

Supplementary Note 1.

Alternative reactions utilising sulphite sources:

$$N_2 + 3H_2SO_3 + 3H_2O = 2H_2SO_4 + (NH_4)_2\,SO_4$$

$$N_2 + 3KHSO_3 + 3H_2O = KHSO_4 + K_2SO_4 + (NH_4)_2\,SO_4$$

Supplementary Note 2.

Calculation of the reaction free energy change (in the dark).

Using the overall reaction:

$3H_2O + 3SO_3^{2-} + N_2 + 2H^+ = 2NH_4^+ + 3SO_4^{2-}$ **Supplementary equation 1**

The free energy equation can be written

$\Delta G = \Delta G^0 + RT \ln [a(NH_4^+)^2 \,.\, a(SO_4^{2-})^3] / [\, a(H_2O).\, a(SO_3^{2-})^3.\, a(N_2)\, .a(H^+)^2]$

Supplementary equation 2

The following concentrations correspond to the situation in our experiments after 24hours reaction:

$[SO_3^{2-}] = 1.87$mM

$[N_2] = 20$mg/L $= 0.71$ mM (N_2 solubility in water)

$[H^+] = 1.5E^{-6}$ M

$[NH_4^+] = 0.18$mM

$[SO_4^{2-}] = 0.27$mM

We can calculate ΔG^0 for the reaction from the standard electrochemical potentials

$E^0(N_2/NH_4^+) = -0.09$ V

$E^0(H_2SO_3/H_2SO_4) = +0.17$ V

$\Rightarrow \Delta E^0 = -0.26$

$\Delta G^0 = -nF\Delta E^0 = 150$ kJ/mol

where $n = 6$.

Substituting these values into Eqn 2 produces the result:

$\Delta G_{24\,hours}$ = 179 kJ/mol.

The positive value of ΔG indicates that the reaction is distinctly not spontaneous under these conditions in the dark.

Repeating the calculation for an earlier time where the concentration of products is only 10% of the t=24h values, the free energy change is then ΔG = 149 kJ/mol, confirming that the dark reaction is non-spontaneous even at quite early stages of the process.

Supplementary References:

1 Rao, N., Dube, S. & Natarajan, P. Photocatalytic reduction of nitrogen over (Fe, Ru or Os)/TiO_2 catalysts. *Appl. Catal., B* 5, 33-42 (1994).

2 Zhu, D., Zhang, L., Ruther, R. E. & Hamers, R. J. Photo-illuminated diamond as a solid-state source of solvated electrons in water for nitrogen reduction. *Nat Mater* 12, 836-841, (2013).

3 Christianson, J. R., Zhu, D., Hamers, R. J. & Schmidt, J. R. Mechanism of N_2 Reduction to NH_3 by Aqueous Solvated Electrons. *J. Phys. Chem. B* 118, 195-203 (2013).

4 Oshikiri, T., Ueno, K. & Misawa, H. Plasmon - Induced Ammonia Synthesis through Nitrogen Photofixation with Visible Light Irradiation. *Angew. Chem.* 126, 9960-9963 (2014).

5 Li, H., Shang, J., Ai, Z. & Zhang, L. Efficient Visible Light Nitrogen Fixation with BiOBr Nanosheets of Oxygen Vacancies on the Exposed {001} Facets. *Journal of the American Chemical Society* (2015).

6 Banerjee, A. *et al.* Photochemical Nitrogen Conversion to Ammonia in Ambient Conditions with FeMoS-Chalcogels. *J. Am. Chem. Soc.* 137, 2030-2034 (2015).

Chapter Four:

Semiconductor Optimization and Experimental Conditions

4.1 Introduction

Although the yields in chapter three are relatively high, they were not sufficient for commercial application. The relative quantum efficiency of the published paper was in the range of 10^{-3} %, and this needs improvement even though it is solar driven (uses only sunlight as an energy source). Further optimisation is introduced in this chapter regarding catalyst conductivity, catalyst thickness; gold nano-particles cover density, temperature, and pH.

These studies need a stable environment, as the changes to the catalyst were relatively minor and it is crucial to differentiate them to understand the thermodynamic, physical and chemical trends. To establish a stable environment an incubator needs to be built to stabilise many variations like temperature, ambient light, and nitrogen gas flow rate. For these reasons an incubator has been developed (discussed in detail below), the incubator produces a relatively stable environment, minimises ambient light effects, maintains room temperature, provides a good trap (for the evolved gases) and a controlled, steady gas flow rate.

Catalyst thickness and conductivity are obvious parameters that need to be optimised. GNP coating is also an important factor, as described in chapter two. Increasing the thickness of the GNP particle layer will boost the production rate, but on the other hand, will trim the ability of Si to absorb more light due to the increased coverage of the Si surface. The study was designed to find the optimal GNP cover.

In this process, control the temperature was a challenge to overcome; the incubator needs to successfully minimise the effect of ambient temperature and the heat generated from the light source. We also introduced a temperature study in order to observe the trends

of ammonia generation with temperature. The trend obtained was comparable to the pattern of the Si band gap at different temperatures (more details below).

4.2 Incubator design and build

A metal incubator (figure 4-1) was built with the dimensions (500X500X300 mm), with a total volume of 75 L. The size has been chosen, prioritising stable temperature, to be spacious enough to maintain a relatively stable environment and to eliminate temperature fluctuations. A slot 65 X 20 mm was cut on the side, to allow the simulator light beam and room temperature air to go through toward the cell, though the slot was not big enough to allow entry of significant ambient light. Also, a sliding door (the whole side of the incubator) was used to allow sufficient access to the cell, trap and flow controller.

The incubator and the solar simulator were fixed on a heavy base to stabilise the system and to maintain the exact (measured) distance between the simulator and the cell; the distance was chosen as explored earlier in chapter three to maintain two sun illumination from the solar simulator.

The solar simulator usually generates relatively large heat by comparison to the cell size, heating the cell and the air around it and as a result, increase the incubator environmental temperature. A 12V fan (92 X 92 X 25 mm) has mounted on the upper side of the incubator, with 32000 rpm speed, to expel warm air from inside the incubator. This fan was sufficient enough to maintain relatively stable environmental temperature (within a range of 5 degrees) inside the incubator (figure 4-1, 4-2).

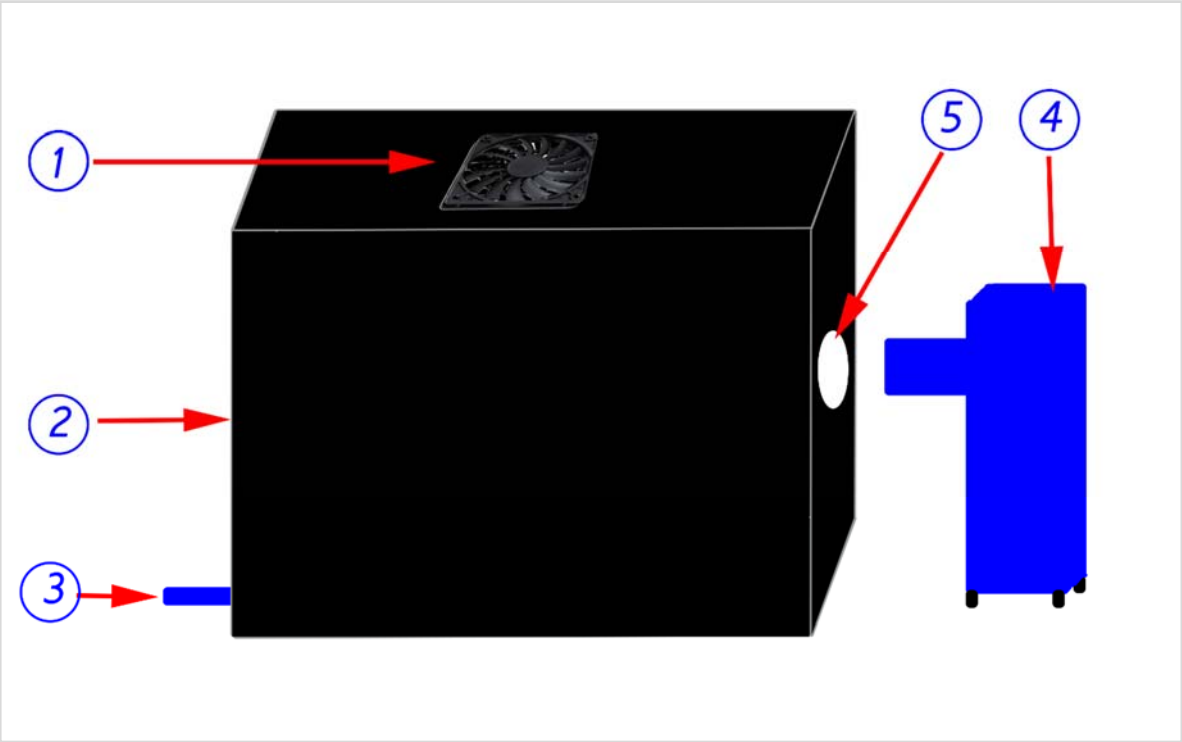

Figure 4-1: Incubator design external view 1) vacuum fan 2) primary metal incubator 3) N_2 gas inlet 4) solar simulator 5) light inlet lit

In order to make sure temperature variations do not affect the gas flow rate controller, two gas flow rate controllers used, outside and inside the incubator, theses controllers were used to controlling and maintaining Nitrogen gas flow through the system; the flow rate was measured using (RESTEK ProFLOW 6000 Flowmeter). A stand was fixed inside the incubator to be used to mount the cell in the exact location in front of the light beam and to mount the trap away from the light beam (figure 4-2).

Ice bath, heater and stirrer are added to the system on later stages as required by each experiment.

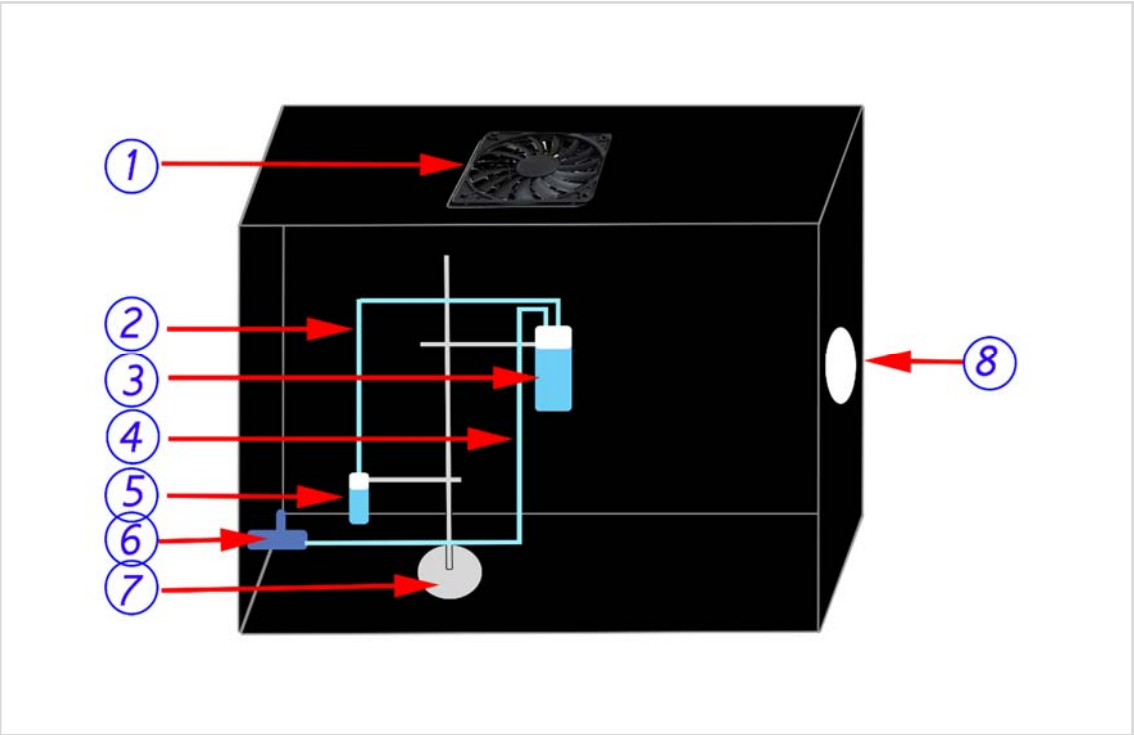

Figure 4-2: Incubator design inside view 1) vacuum fan 2) gas out from the reaction chamber 3) cell (reaction chamber) 4) gas into the reaction chamber 5) evolved gas trap 6) N_2 gas inlet (control) 7) stand 8) light inlet.

4.3 Silicon conductivities, thicknesses and etching conditions

Doping silicon grants it an ability to assist the photo-generated electrons and holes, through pathways of asymmetrical conductivity towards their respective contacts, which may be considered to be a salient characteristic of doped silicon [1]. The conductivity of silicon wafers is the core of the overall photo-generation process, while on the etched surface the physical, chemical and attached metal properties allow electron transfer from the conduction band towards the electrode/electrolyte interface. Conductivity is advantageous for energy conversion efficiency and electron transferability; however, high conductivities will ease and fasten the electron-hole recombination process [1, 2].

The recombination of the electron/hole pair is predominant with a consequent decrease of the power conversion efficiency whenever the semiconductor layer becomes thick [3]. Also, wafer thickness also impacts on the electron travel time through the wafer[4]. Correspondingly, this concept is considered of vital importance to the overall efficiency of the electrode and will be discussed further in 4.6.

Several different wafers with different conductivities and thicknesses were studied (Table 4-1), these wafers were dry-etched in the same way using an Oxford PlasmaLab 100 ICP380 system. The mixed mode etching process was used, wherein etching and passivation occurred at the same time. The conditions for the black silicon formation were: SF6 gas flow rate 65 SCCM, O2 gas flow rate 44 sccm, the pressure of 35 mTorr, reactive ion etching (RIE) power 100 W, electrode temperature 20°C and the backside cooling pressure 15 Torr.

Practically, conductivity was not the main factor affecting the cell efficiency, the yield comparison in table 4-1 not producing any linear trend, though some trends were visible.

Lower resistances (1) were expected to produce higher efficiency; also, yields form (3 and 5) and yields from (2 and 4)) converged, while the yield from (4) was very small.

Also, cell the thickness study was somewhat ambiguous; thicker wafers (4) produced the lower yields as expected, but, the relatively thinner wafer yields (3) were also small compared to (2 and 5). The wafers (2 and 5) might be optimum in this study.

Table 4-1: Ammonia yield for different thicknesses and different resistance wafers

Yield mg m^{-2}	Thickness/µm				No.	Resistance Ohm cm^{-1}
	380	500	525	1000		
			19.70±3.98		1	0.001-0.005
		22.54±2.12			2	1-10
	19.25±1.32				3	5-10
				10.62±1.44	4	1-20
		21.34±2.81			5	10-20

These overall variations might be understood in terms of the overall dry etching process precision; this accuracy can vary on different areas on the same wafer, and also, can be affected by the cleanness of the wafer surface. Rigorous measures were used to clean and maintain the cleanliness of the wafer surface. A two-step cleaning was performed, the first step was wet chemical surface treatment, using hot alkaline and acidic hydrogen peroxide solutions, and a second step was performed systematically in the etching device as mentioned above[5].

Also, doping efficiency in the substrate provided (University Wafers, Boston, Massachusetts) might vary on different wafers and different areas (spots) inside the same wafer, although we used the highest grade available. These variations might vary the efficiency between different wafers and to a lesser extent in the same wafer. For this reason,

in most of our experiments, we used parts from the same wafer when repeating the same experiment.

4.4 Gold coatings and plasmonic effects

Plasmonic effects (as explained in detail in chapter two, section 2.2.2) were one of the most critical concepts in this study; it has remarkably increased the cell efficiency (see chapter three figure 2b and 3a). Consequently, we hypothesised that increasing the number of deposited nano-particles onto the wafer surface would increase the PCE up to a specific limit where the bulk of these particles start to obscure the light reaching wafer surface.

To study the optimum deposited amount with the highest SPR possible, an experiment was designed, where a new set of cells built with different GNP depositing times. These cells were taken from the same wafer to minimise errors came from wafer doping and etching quality. The sputter coater used the same Au target while maintaining the same conditions from previous experiments at 25 mA.

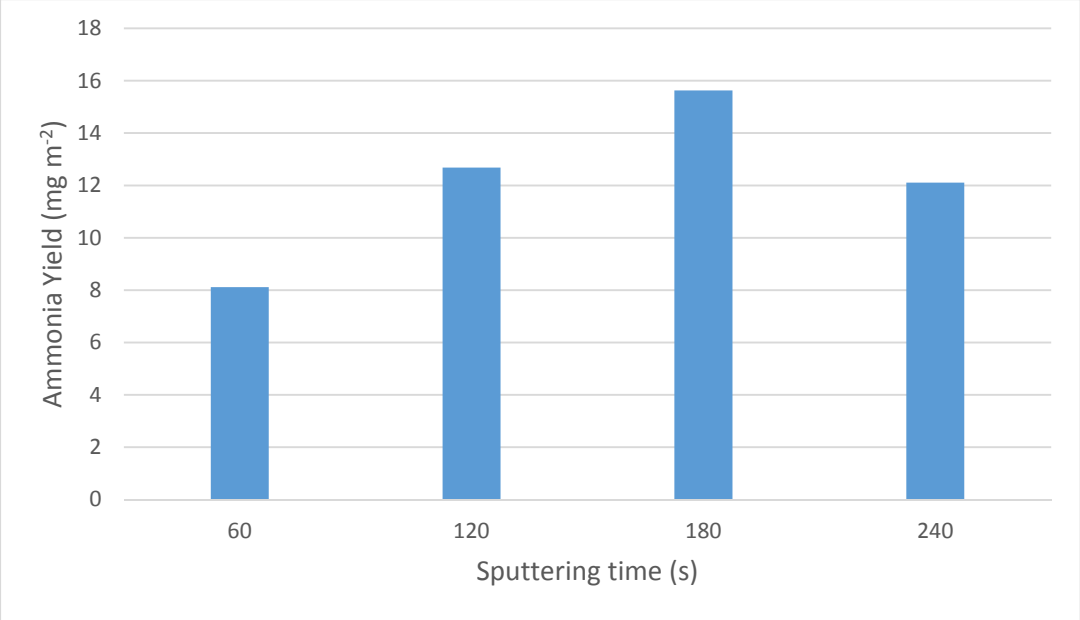

Figure 4-3: Cell efficiency (yield comparison), for cells with different GNP deposition times. Experimental conditions maintained precisely the same as used in chapter three.

Due to sputter device safety recommendations, sputtering was limited to the multiples of 60s. The results obtained increased as expected with the highest efficiency reported is 156 mg m^{-2} when GNP was deposited three times (total of 180s, 60s each time), while the lowest efficiency obtained was 81 mg m^{-2} when GNP was deposited only one time (60s). Beyond 180 s the yield decreased again; the higher number of deposited nano-particles after a specific limit due to a decline in the absorbed light at the higher surface coverage (Figure 4-3).

4.5 pH effects

One of the most critical variables affecting the catalyst performance in an aqueous system is pH. It impacts many parameters like the charge on catalyst particles, the size of catalyst aggregates and the position of the conductance and valence bands [6]. Simply, at low pH, H^+ ions are adsorbed onto the catalyst surface, and in the absence of oxygen, H^+ ions may interact with photo-generated electrons forming H_{ads}° radicals that are capable of producing

H_2 or reducing surrounding ions[7]. This potentially poisons the catalyst surface [8], where, the catalyst surface active sites are filled with H atoms instead of N_2 atoms in an aqueous electrolyte. This will block this surface site for completion of the catalytic cycle. Operating in relatively high pH conditions lowers the surface concentration of H^+ which decreases the overall efficiency.

Two experiments (figure 4-4 and figure 4-5) have been designed to address this issue, where a range of different pH's have been tested. In the first set of experiments, variety electrolytes of pH 2 to pH 9 were prepared using only HCl and/or NaOH in deionised water. In the second set, a range of pH2 to pH6 was prepared using citrate buffer, which has a better ability to relatively maintaining the pH constant during the 3h experiments.

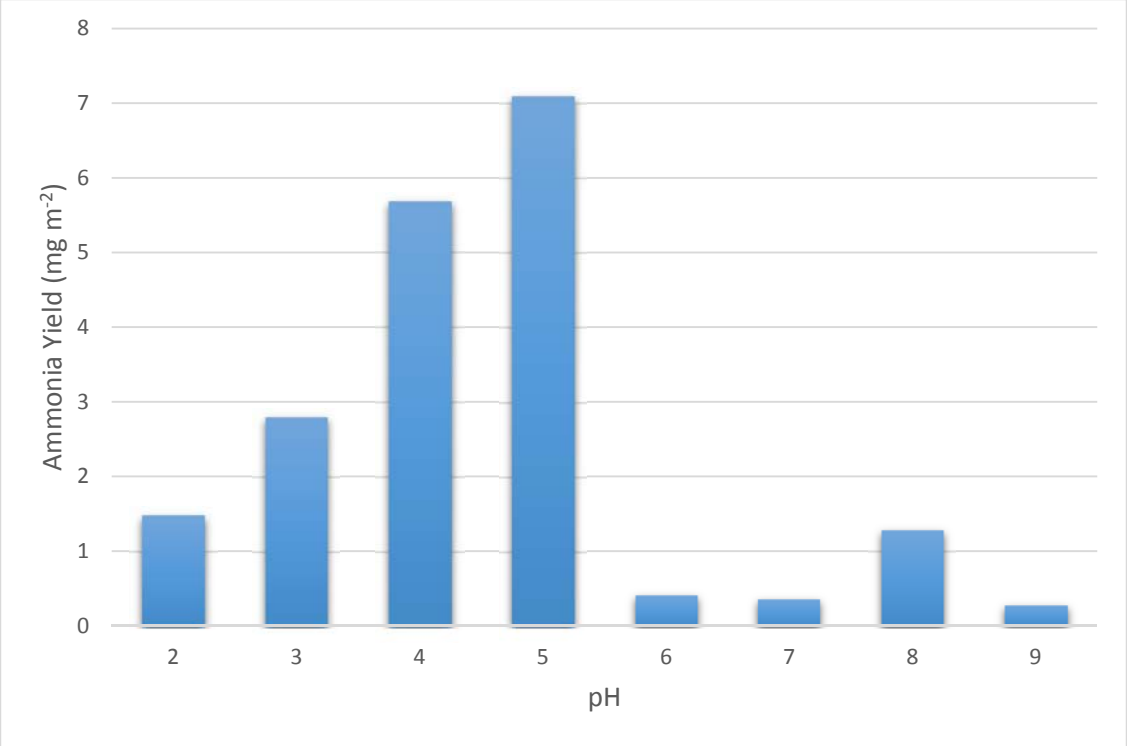

Figure 4-4: Cell efficiency (yield comparison) for a pH range from 2 to 9, obtained using HCl and NaOH. Experimental conditions kept the same as used in chapter three.

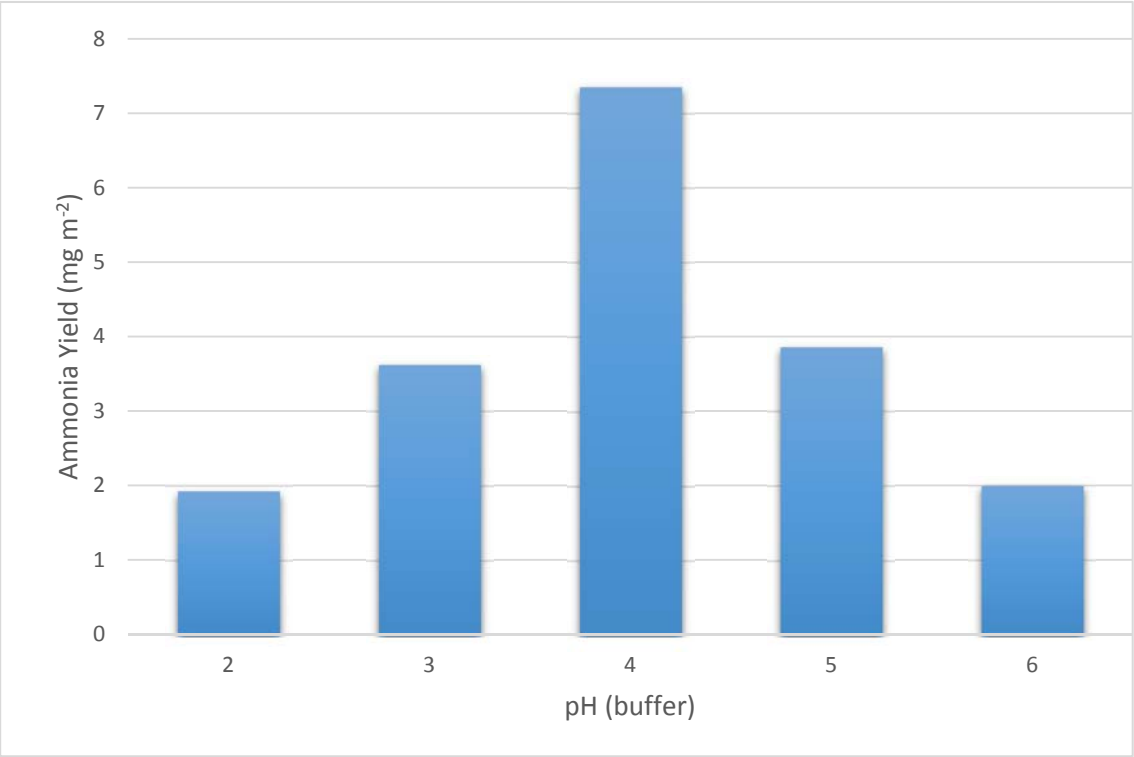

Figure 4-5: Cell efficiency (yield comparison) for a pH range from 2 to 6 in citrate buffers. Experimental conditions kept the same as used in chapter three.

Results for the two different set of experiments were convergent with minor differences, mainly between pH 4-5, which might be expected due to the higher complexity of the electrolyte in the citrate buffer case and the difference in the overall ionic strength of the electrolyte. The set of experiments results indicate that moderate acidic to neutral pH gives the highest efficiency, indicating an optimum balance of proton availability without over-populating the surface H• radicals.

4.6 Temperature effect on PCE

The temperature has a direct effect on semiconductor properties especially conductivity, reactivity and light-absorbing capacity [9]. It is widely recognised that semiconductor thermal conductivity (K) increases with temperature increase, and this is because the number of free electrons in the semiconductor valence band increases with an increase in temperature. Interestingly, this is not always true in the case of silicon nanowires (SNWs), D Donadio and G Galli [10] have concluded from the calculation that K in SNWs reaches nearly constant values between 200 and 600 K (-73 to 326^{o}C).

The temperature might also affect wafer chemical and physical properties; temperature in the presence of aqueous electrolyte will remarkably increase the growth of the SiO_2 layer on the cell surface [11-13] and this layer will act as an insulator and decrease the overall PCE. Also, optical properties and light absorptivity of silicon are directly affected by T. Studies have found that the effect of a temperature increase appears as a redshift of the absorption spectrum [9], and directly impacts the absorption coefficient and free-carrier absorption cross-section[14].

Although we have designed and manufactured an incubator, it is quite difficult to obtain a precisely stable temperature during the photocatalytic process, due to the heat coming from the solar simulator and the direct effect of ambient heat variations. It is rather more meaningful to state a stable range of temperatures (within 10 ^{o}C),. An experiment was designed using temperature ranges of -5, 30-40, 40-50, and 50-60^{o}C; these temperature ranges were obtained using an ice bath and digitally controlled heater. Using parts from the same wafer within the same conditions as before we observed the following result (figure 4-6).

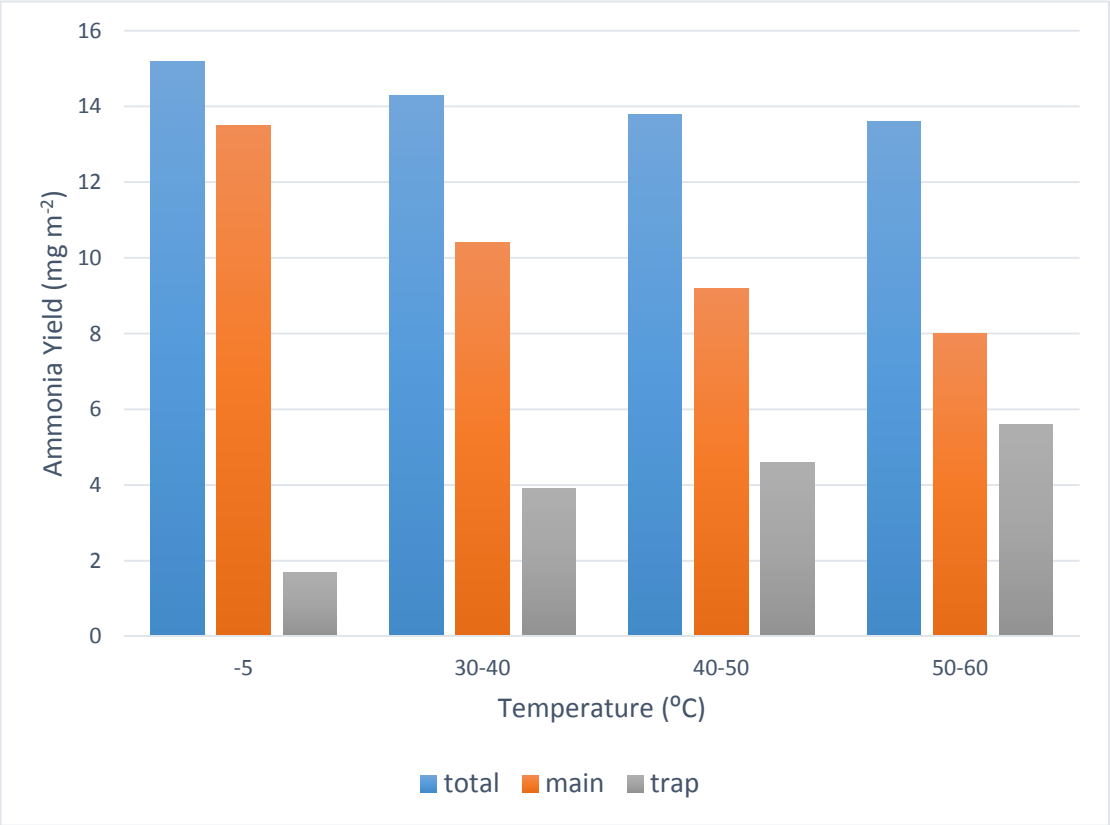

Figure 4-6: Thermal effect on yield in the primary cell chamber, trap and total yield. Columns: blue total yield, orange yield in the main chamber only, grey yield in the trap only. Experimental conditions kept precisely the same as used in chapter three.

Results were relatively clear-cut, the overall trend decreased in the total yield (blue column) with increasing temperature, which disproves the hypothesis of changing chemical and physical properties of the semiconductor, with temperature increase. Since the solubility of N_2 in the aqueous solution is low but increases with decreasing temperature, the behaviour seen in figure 4-6 seems to indicate that the low availability of N_2 is a limiting factor in this process.

Also, a trend here was clear that as the temperature increased the yield collected from the main chamber (orange column) decreased, while the yield obtained from the trap (grey column) increased. This is likely due to the increased volatility of the generated ammonia with increasing temperature [15, 16], and the ability of bubbled nitrogen gas to carry it toward the trap.

4.7 Conclusions

In this chapter, the work focused on optimising the semiconductor and varying the experimental conditions in order to improve the overall prototype efficiency. An incubator was built to minimise the environmental interferences in the experiments, controlling the gas flow rate, and minimising the ambient light.

A variety of Si wafer were investigated with different thicknesses and conductivities, resulting in different trends, the highest efficiency obtained being 22±2 using 500µm sample thickness, with a resistivity of 1-10 ohm cm^{-1}.

The plasmonic effect influences the working prototype productivity; 180s (3 coatings) was found to be the optimised gold thickness that produces the maximum impact without overcoating or blinding the semiconductor surface.

Understanding the pH effect on the PCE and yield formation, involved the design of two experiments varying the electrolyte acidity to find the optimum pH, either buffering the electrolyte or simple acidify/basify using HCl and NaOH. Both approaches show a tendency toward the neutral and/or slightly acidic medium as optimum.

the temperature is a crucial factor in the overall PCE. Higher efficiencies were observed at lower temperatures in contrast with the hypothesis that expected better conductivities at higher temperatures. Also, the amount of the yield in the trap increased with temperature, opposite to that in the primary chamber, confirming ammonia evaporation at higher temperatures.

4.8 References

1. Bullock, J., et al., *Efficient silicon solar cells with dopant-free asymmetric heterocontacts.* Nature Energy, 2016. **1**: p. 15031.
2. Shockley, W. and W. Read Jr, *Statistics of the recombinations of holes and electrons.* Physical review, 1952. **87**(5): p. 835.
3. Notarianni, M., et al., *Plasmonic effect of gold nanoparticles in organic solar cells.* Solar Energy, 2014. **106**: p. 23-37.
4. Fuhrer, M.S., C.N. Lau, and A.H. MacDonald, *Graphene: Materially Better Carbon.* MRS Bulletin, 2011. **35**(4): p. 289-295.
5. Kern, W., *The evolution of silicon wafer cleaning technology.* Journal of the Electrochemical Society, 1990. **137**(6): p. 1887-1892.
6. Shen, M. and M.A. Henderson, *Identification of the active species in photochemical hole scavenging reactions of methanol on TiO2.* The Journal of Physical Chemistry Letters, 2011. **2**(21): p. 2707-2710.
7. Shand, M. and J.A. Anderson, *Aqueous phase photocatalytic nitrate destruction using titania based materials: routes to enhanced performance and prospects for visible light activation.* Catalysis Science & Technology, 2013. **3**(4): p. 879-899.
8. Abghoui, Y., et al., *Enabling electrochemical reduction of nitrogen to ammonia at ambient conditions through rational catalyst design.* Physical Chemistry Chemical Physics, 2015. **17**(7): p. 4909-4918.
9. Weakliem, H. and D. Redfield, *Temperature dependence of the optical properties of silicon.* Journal of Applied Physics, 1979. **50**(3): p. 1491-1493.
10. Donadio, D. and G. Galli, *Temperature dependence of the thermal conductivity of thin silicon nanowires.* Nano letters, 2010. **10**(3): p. 847-851.

11. Raider, S., R. Flitsch, and M. Palmer, *Oxide growth on etched silicon in air at room temperature.* Journal of the Electrochemical Society, 1975. **122**(3): p. 413-418.

12. Morita, M., et al., *Growth of native oxide on a silicon surface.* Journal of Applied Physics, 1990. **68**(3): p. 1272-1281.

13. Hu, J., et al., *Temperature‐Dependent Growth of Germanium Oxide and Silicon Oxide Based Nanostructures, Aligned Silicon Oxide Nanowire Assemblies, and Silicon Oxide Microtubes.* Small, 2005. **1**(4): p. 429-438.

14. Svantesson, K. and N. Nilsson, *Determination of the temperature dependence of the free carrier and interband absorption in silicon at 1.06 µm.* Journal of Physics C: Solid State Physics, 1979. **12**(18): p. 3837.

15. Chao, T.-T. and W. Kroontje, *Relationships between Ammonia Volatilization, Ammonia Concentration and Water Evaporation 1.* Soil Science Society of America Journal, 1964. **28**(3): p. 393-395.

16. Khan, T.S., et al., *Experimental investigation of evaporation heat transfer and pressure drop of ammonia in a 60 chevron plate heat exchanger.* international journal of refrigeration, 2012. **35**(2): p. 336-348.

Chapter Five

Ru as a catalyst for the photochemical nitrogen reduction process

5.1 Introduction

5.1.1 NNR catalysis background

Aiming towards higher economic and environmental efficiency in chemicals manufacturer has always led to a growing need to choose better catalysis. Industrial ammonia production through the Haber–Bosch process was the first heterogeneous catalytic process utilised in the chemical industry and is still in use today[1]. Ostwald [2] began this approach by introducing iron as a catalyst reversing the widely known process at that time of ammonia decomposing into hydrogen and nitrogen over an iron surface. This concept was soon modified by Bosch, who concluded that an impure iron catalyst was responsible for the high concentration obtained from Ostwald's experiments and that the catalyst contained considerable amounts of ammonia and nitride [3]. Haber's interest was not only on the reaction thermodynamics but also on the reaction rate since the catalyst does not directly affect the equilibrium composition and the maximum reaction yield[3].

In 1823, Dobereiner [4], had for the first time reported forming ammonia from a direct combination of hydrogen and nitrogen in air deficiency using platinum as a catalyst. In 1839, Kohlman used a platinum sponge as a catalyst to convert nitric oxide and hydrogen to ammonia. Later, Charles Tellier reported that a sponge of Iron acted as a catalyst able to absorb a considerable amount of nitrogen and form iron nitride, then eventually in the presence of hydrogen ammonia. Also, an Austrian patient used titanium or titaniferous compounds in admixtures with platinum supported on porous materials [1, 5].

In that period, scientists generally accepted that at medium temperatures nitrogen is too inert to react directly with hydrogen. Scientists also acknowledge the fact that although

at high temperatures the reaction becomes possible, the decomposition of ammonia will take place, accordingly the need for a better catalyst led Perman [6] to use iron as a catalyst for nitrogen reduction, but his research faced a problem with the existence of moisture, which was causing retardation of the overall reaction.

In 1909, and after many traias with uranium and osmium as a catalyst, Haber was finally able to prepare 80g/hr of ammonia using 98g osmium at 175 bar. Later, for industrial scale production, a cheap, active and more stable catalyst was required compared to osmium and uranium, since both have handling problems and are rare[7].

At first, iron was introduced in its pure form; later, Mittasch et al. reported that iron was remarkably affected by the extent of impurities in it. Consequently, multicomponent catalysts instead of pure iron were studied [8]. They experimented with a range of iron compounds with additives like oxides, chlorides and sulphates. Originally the hypothesis was to investigate the reaction intermediates which are considered to be metal nitrides. Through systematic, though extensive, research on more than 6500 catalytic compounds during more than 6500 experiments, Mittasch et al. [8] concluded that the general effect of additives on catalytic behaviour could be improving the catalytic activity, but others are positively detrimental and poison the catalysts. Also, the research ended up with the most suitable catalyst for the industry at the time, which was iron combined with alumina and magnesia; conveniently, those were available at high scale in Sweden. This catalyst was active and stable enough for the industrial high temperature and pressure process [5, 7].

Over the past century and especially from the early to mid-1900s; a lot of improvements and optimisation were achieved in the Haber Bosh process (HBP), but the industrial catalyst used today is similar to the original catalyst [9]. Studies find a direct relationship between the

efficiency of HBP and the single-crystal iron structure, proving that Fe(111) crystal face is the most reactive because the highly coordinated Fe sites (C7 within the Fe(111)) experience considerable electronic fluctuations [10, 11]. Also, the addition of promoter oxides (like; Al2O3 and K2O), in industrial HBP, are not sufficiently reduceable, which prevents the sintering of the iron, increases the reaction rate, and increases the surface area [10, 12, 13].

5.1.2 Ru catalytic NRR

In 1960, the non-ferrous catalysts starting to receive more attention as Ozaki et al. introduced the so-called volcano plots, based on the energies of chemical adsorption and desorption of nitrogen species on the catalyst surface[14]. In this plot, iron, osmium and ruthenium were at the maximum, which shifted most of the studies toward Ruthenium-based compounds[13, 14]. Promoters like Al_2O_3 [15], MgO [15-17], $MgAl_2O_4$ [18]and a mixture of Ba-Cs [19] were added to Ru, to boost the nitrogen reduction process, which eventually led to commercialisation of the Ru-based; Kellog Brown and Root (KBR), advanced ammonia process (KAAP)[20]. This process was used industrially in 1992 with a Ru catalyst promoted with Ba-Cs supported on graphitised carbon, which at low pressure, was ten times more active than the HBP iron catalyst [13, 20]. Other studies in the past 20 years used supports to promote the Ru catalyst like BN [21], $BaCeO_3$ nanocrystals [22], MgO [23], CeO_2 [23], Sm_2O_3 [24], graphitic nanofilaments [25] and $[Ca_{24}Al_{28}O_{64}]^{4+}$ [26].

Aiming for a better understanding of the catalytic role of Ru in the NRR, theoretical studies split the NNR mechanisms into two possible types of reaction, associative and dissociative depending on hydrogenation steps to the bound nitrogen on the catalyst surface

[27, 28], studying the overall free energy changes of possible intermediates at ambient conditions. Starting with the N_2 molecule ($*N_2$) binds on to the Ru surface (adsorption energy −0.4 eV), and by considering the entropy loss by changing from the gas phase to a molecule bonded to the surface, +0.08 eV is calculated to be the free energy change. The hardest exothermic step is the addition of the first H atom. This step is +0.75 eV upward in energy and 1.08 eV in free energy and is considered to be the rate determining step. With applied potential (or in our case light), all the steps, from N_2 gas adsorption on the catalyst surface to the NH_3 formation and release, the free energy has either not changed or is decreased, favouring the NRR[27].

As explained earlier nitrogen binding to the catalyst surface is the preliminary step in the NRR, and an ideal catalyst material should have optimal nitrogen binding ability. Accordingly, the volcano plot described earlier as introduced by Ozaki et al. [14] were the guide to the subsequent theoretical studies. Metals like Re, Ru, Rh, Fe, Mo, Ir, Pt, Cu, and Ag were theoretically studied depending on their location on the plot [27, 29]. Results indicate weak binding on both Ag and Cu and optimised binding in Fe, Mo, Ru and Rh, while Pt and Ir had a problem with competing H binding favourably to the catalyst, promoting the hydrogen evolution reaction (HER) [27].

Recently, NRR has performed electrochemically under ambient conditions. The most widely explored catalysts are Ru [30-34], Fe [35], Rh [36] Au [37] and Pt [38]. Photochemically, the only Ru-based study published recently used single atom Ru decorated TiO_2 nanosheets [39]. The study found a direct effect of the isolated Ru atoms on weakened the hydrogen evolution, promoted absorption of N_2, and also improved the charge carrier separation [39].

In this chapter, we extend our studies of black silicon based photoreduction of N_2 to an investigation of the effect of two different catalysts (Fe and Ru) on the overall NRR using black silicon. Also, we are experimenting with the impact of the dispersed catalytic ions (in the electrolyte) on our previously explained photocatalytic NRR. In this work, we attached the prefered catalyst (Ru in this study) onto the Si surface, using three different methods; drop-casting, electroless depositing [40] and photochemical deposition.

5.2 Catalysts investigations

5.2.1 drop-casting Ru catalyst onto black silicon

The first and most straightforward approach to add a catalyst into our successful plasmon-enhanced black silicon was by drop-casting. This experiment was more difficult than expected for several reasons, including poor ability of Ru to be attached firmly to the bSi surface, blocking the light due to overcoating of the bSi, limitation in full area coverage, poor uniformity and blinding the spectrophotometric testing method. To overcome some of these limitations, we experimented with spin coating [41] and simple drop-casting.

Spin coating can overcome some limitations like uniformity and coverage, but it was very unsuccessful in other areas like coverage thickness, especially for our type of semiconductor. This method has a problem with the ability to control the concentration and the layer thickness because even at low spinning speeds the loss of material was visible. Also repeating the experiment to deposit more layers were not repeatable.

Simple drop-casting was the better choice in regards to concentration and thickness control, though it has many deficiencies in regards to coverage and uniformity. Two different concentrations (1 and 100 µM) of $RuCl_3$ were drop-cast into GNP/bSi/Cr samples; the samples

were left for 24hours under photo-exposure to allow Ru to be reduced and attached to the Si surface.

Studying the ability of Ru to catalyse the process in our previously described cell (chapter two) resulted in the data in figure 5-1.

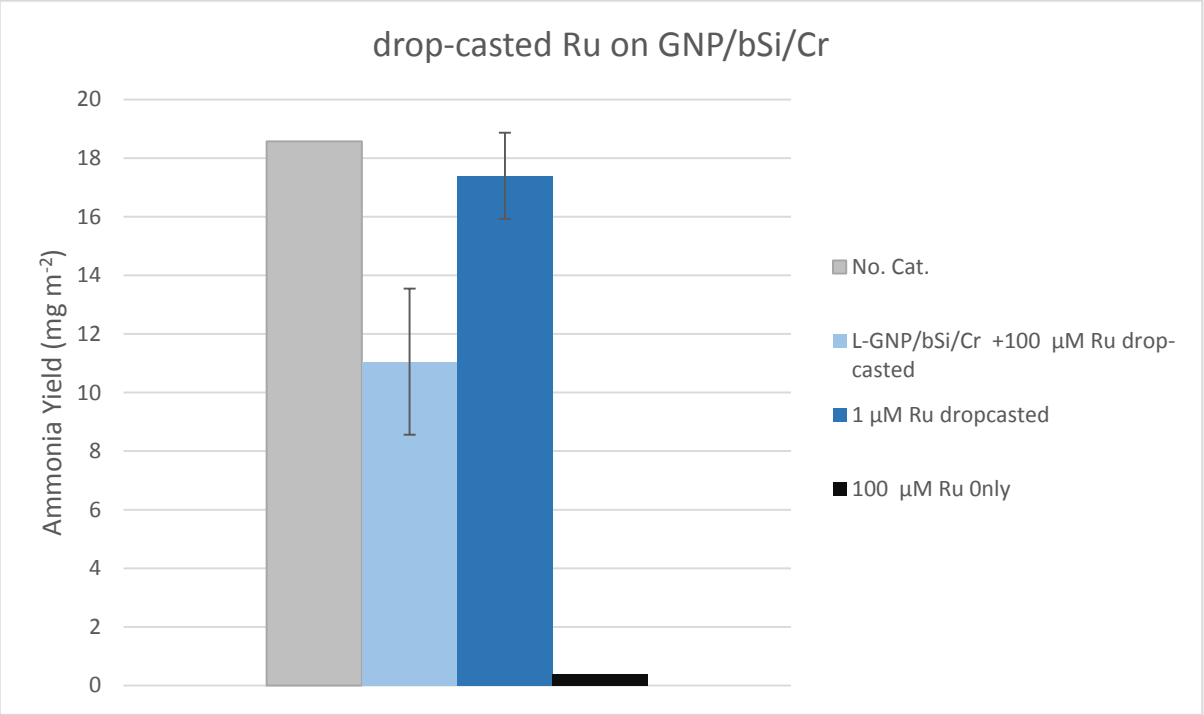

Figure 5-1: Ammonia yield comparison of drop-cast Ru. Control , 100µM RuCl3 drop-cast , 1µM $RuCl_3$ drop-cast , and control experiment of 100µM $RuCl_3$ alone, no semiconductor used . experimental conditions; electolyte: 15ml DW, time: 3h, N_2 flow rate: 5ml/min, and 2sun illumination

the outcome of the experiment was unclear. It was noted that the working solution became darkly coloured indicating the presence of Ru 3^+. Reasons for this may include the dissociation of the remaining (un-attached) $RuCl_3$ in the solution blocking a substantial

amount of the absorbed light and also blinding the photometric detection of the generated ammonia. Also, the differences in results between 1 and 100 µM $RuCl_3$ are obvious, elucidating the semiconductor over-coverage problem. Ru only under sunlight gives small amounts of ammonia, which is expected as background ammonia; this may be considered as clear evidence that Ru^{+3} ions are unable to produce ammonia directly in solution and the study should focus entirely on its catalytic abilities.

5.2.2 electroless Ru catalyst deposition on black silicon

Electroless deposition is another proposed method to attach Ru films onto GNP/bSi/Cr samples. Chen et al. developed this method in 2010 [42], and later further advanced it by adding sensitisation and second activation steps in addition to the previously practised activation and plating steps[40]. Thin Ru films produced by this method are directly affected by the plating time. Accordingly, these thin films transparency and eventually light absorption will be influenced by plating time as well. Replicating the Ru film attachment to the bSi is even more achievable with the dry-etched samples, avoiding the use of dangerous chemicals (HF). Accordingly, only activation, sensitisation, second activation and electroless plating steps were implemented. Firstly, the 1st activation was accomplished by immersing 1 cm^2 Si substrates in a mixture of 0.1% $PdCl_2$ and 1% HCl in deionised water at 40 °C for 10 min. In the second step (sensitisation), bSi samples were plunged into a solution containing 0.3% $SnCl_2$ and 2.5 % HCl in deionised water at 25 °C for 3 min. Finally, samples submerged in a 30 ml Ru electroless plating bath containing 0.0108g $RuCl_3$, 1.8858 g NaClO, 0.04 g NaOH, and 0.0704 g $NaNO_2$ at 40 °C for different times (figure 5-2), samples were extracted and left to dry for at least 12h then washed with deionised water before use [40, 42]. The proposed Ru film formation via an oxidative–reductive mechanism was discussed earlier by Chen et al. [42].

Sufficient thickness of the electroless deposited catalyst with the highest PCE was studied in the following experiment designed by varying the Ru electroless deposition time and correlating with the overall ammonia yield (figure 5-2).

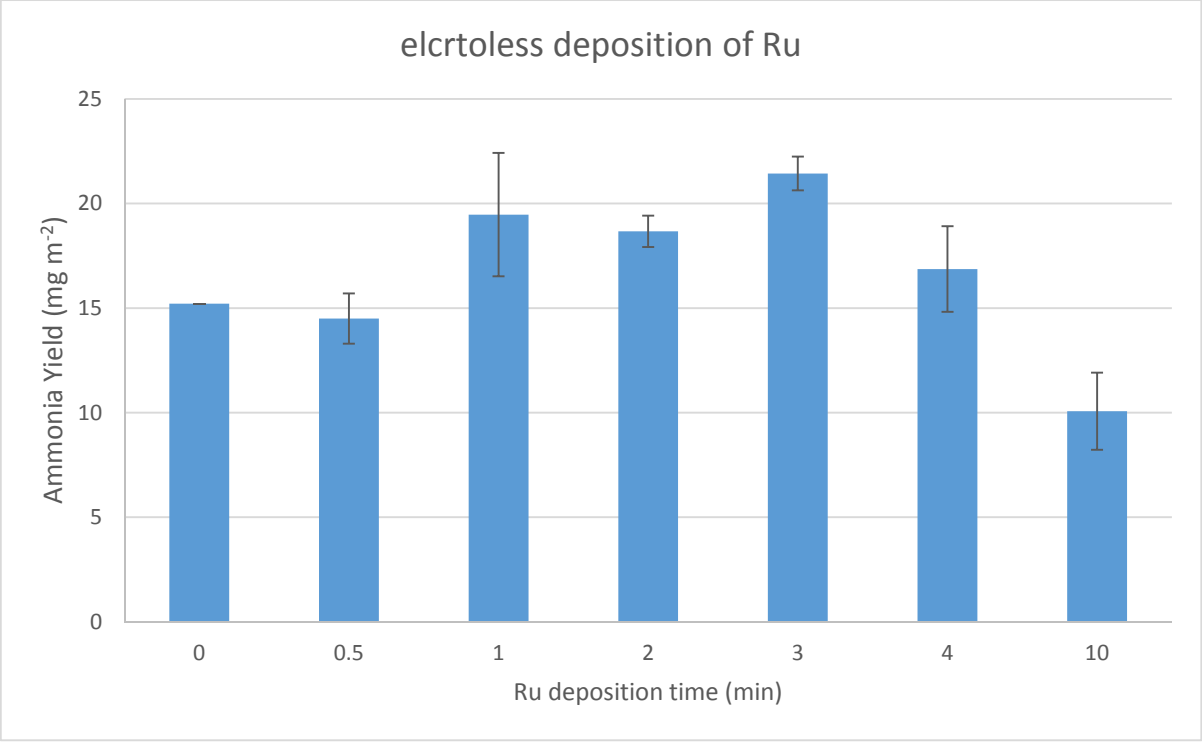

Figure 5-2: Finding sufficient Ru film thickness for the working bSi prototype. Samples were plated with Ru for different times (0.5 - 10 min); control = working prototype (no Ru plating). experimental conditions; electrolyte: 15ml DW, time: 3h, N_2 flow rate: 5ml/min, and 2sun illumination

Results were relative as expected; 1 and 3 minutes has the highest returns compared with 10 minutes, which may be regarded as a result of the over-plating that hinders light absorption. The control (no Ru plating) and 0.5-minute compared to 3-minute plating show that there is an improvement in the overall yield wich which is clear evidence of the catalytic effect of the deposited Ru [39].

5.2.3 Addition of Fe and Ru ions to the electrolyte to catalyse ammonia formation

Industrially the catalytic abilities of metallic iron and ruthenium in dinitrogen reduction to ammonia are well established, where, electrochemically, extensive research of both metals has been conducted in the past few years[30, 32]. Photochemically, the studies are rare, despite the need to develop sustainable ammonia processes and clean energy technoplogies[39]. As discussed earlier, research in all of these fields has proven the effects of these metals in catalysing the NRR, by decreasing the energy needed for the first and highest-energy step[27]. Also, photo-catalytic studies have shown a direct impact on weakening the competitive HER, by promoting stronger absorption of N_2 and improving the charge carrier separation[39].

The catalytic abilities of ions instead of metals have been proven industrially through the existence of iron ionic impurities [8]. Though, the influence of free ions in aqueous electrolyte has not been discussed as yet.

In this experiment, we aimed to study the impact of dispersed Fe^{+3} and Ru^{+3} ions on the overall ammonia yield of our prototype photocatalyst. The main obstacle facing this experiment is extracting the ammonia from the electrolyte, overcoming this obstacle was rather easy in the case of iron because iron oxides are not soluble in aqueous media and it can be filtered before testing the yield. However, this was rather difficult in the case of Ru ions because of $RuCl_3$ is water soluble, this has a direct impact on the colourimetric method used to test the final yield; it changes the electrolyte transparency and may form complexes (as explained later in this chapter) with the synthesised ammonia. To conquer these problems,

two new Indophenol method calibration methods and curves (figure 5-3 A and 5-3 B) have been constructed, based on 100µM and 1mM $RuCl_3$ electrolytes.

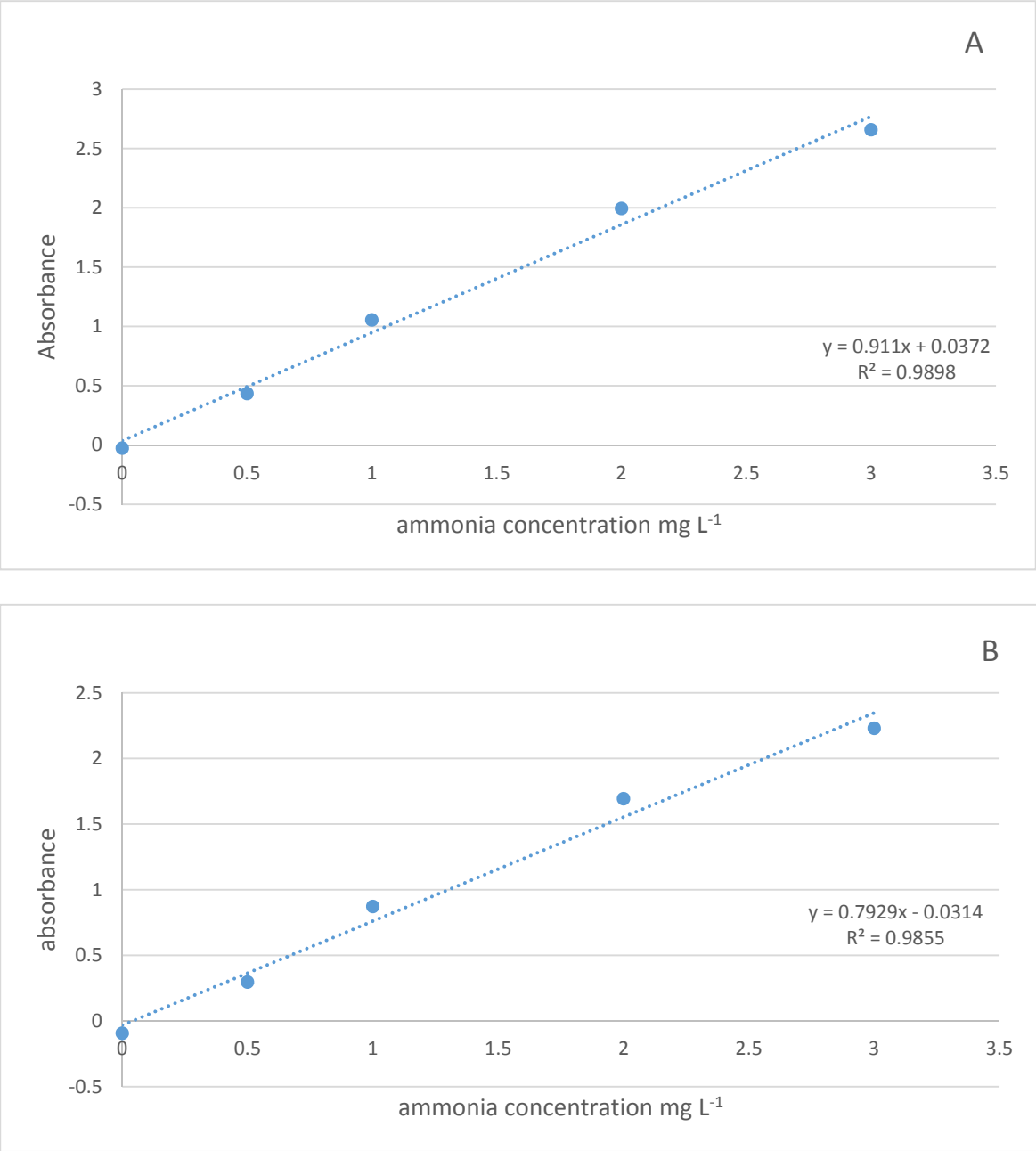

Figure 5-3: Indophenol method UV-Vis calibration curves; these curves were obtained from standard ammonia solutions prepared in A; 100µM $RuCl_3$ and B; 1000µM $RuCl_3$ electrolyte. Absorbance measured at 630 nm.

Comparing these calibration curves with the standard calibration used earlier in chapter three (supplementary information) shows a notable decrease in the absorbance in

the same concentration range, and accordingly the slopes. The slope in figure 5-3A and 5-3B were 0.911 and 0.793 respectively. A relatively good trendline was obtained with a correlation coefficient of 0.9898 and 0.9855 for A and B respectively. These calibration curves were used in later experiments with respect to Ru ion containing electrolytes.

The photo-reaction results in figure 5-4 B and 5-4 C were promising in regards to Ru but somewhat discouraging in the case of Iron. Yields spiked to 36.9 mg m^{-2} in the case of 100µM $RuCl_3$ electrolyte, but the highest yield in the case of Fe was 21.7 mg m^{-2} in the case of 10µM Fe_2O_3.

Several control experiments (figure 5-4 A) were conducted in a dark environment (D) and in 2 sunlight energy supplies (L), gives a yield range between 1.71-2.75 mg m^{-2}, which may be regarded as background ammonia yield coming from bench, gloves….etc, although, we used high purity DW and N_2 gas. Common experimental conditions set to 3h, pH5, two suns and 10 ml/min N_2 flow rate.

The blank experiments (figure 5-4 A) use DW as an electrolyte, no catalyst, 100µM $RuCl_3$ electrolyte and no semiconductor, and 100µM $RuCl_3$ and bSi (with no catalyst deposited). The samples of bSi in 100µM $RuCl_3$ electrolyte gave no significant yield in the dark but a surprising 20.4 mg m^{-2} in the light which may be considered a good indication of the catalytic ability of Ru ions, as the Ru(III) here is acting as a catalyst instead of the GNP coating in earlier samples. It is important that the absence of gold will eliminate the proven plasmonic effect which boosted the yield in previous experiments.

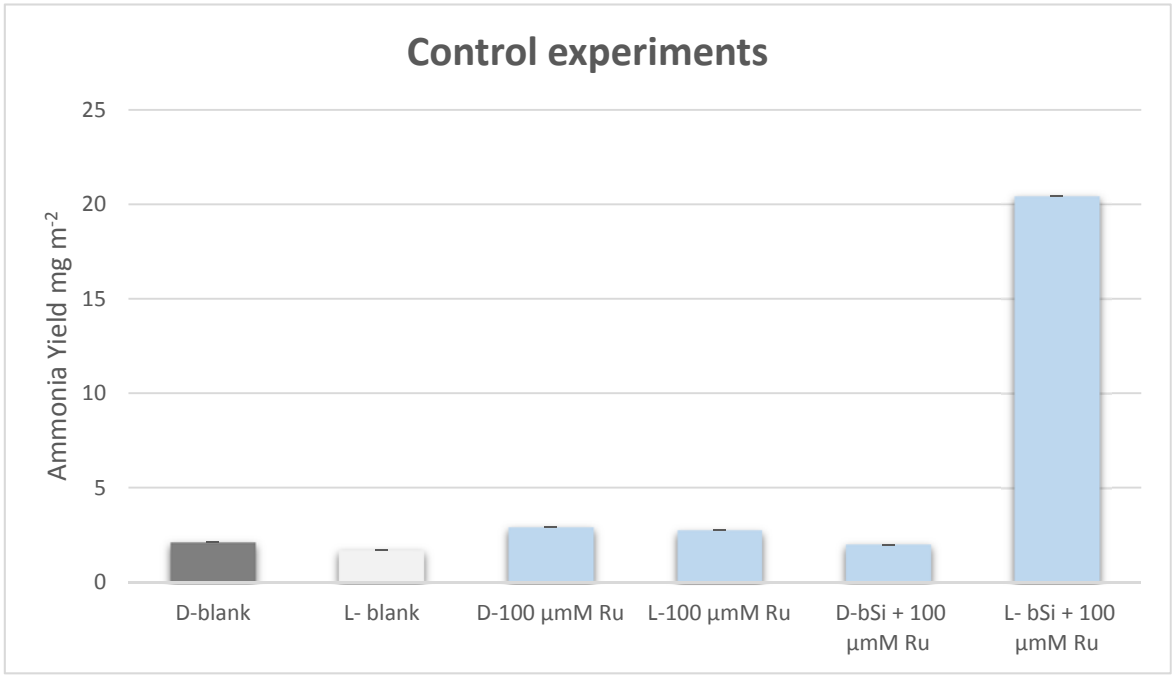

Figure 5-4 A: Photo-catalysis control experiments. D: dark (no light), L: light (simulator light), blank: de-ionised water, Ru: RuCl3, bSi: black silicon only (no catalyst or metal deposited).

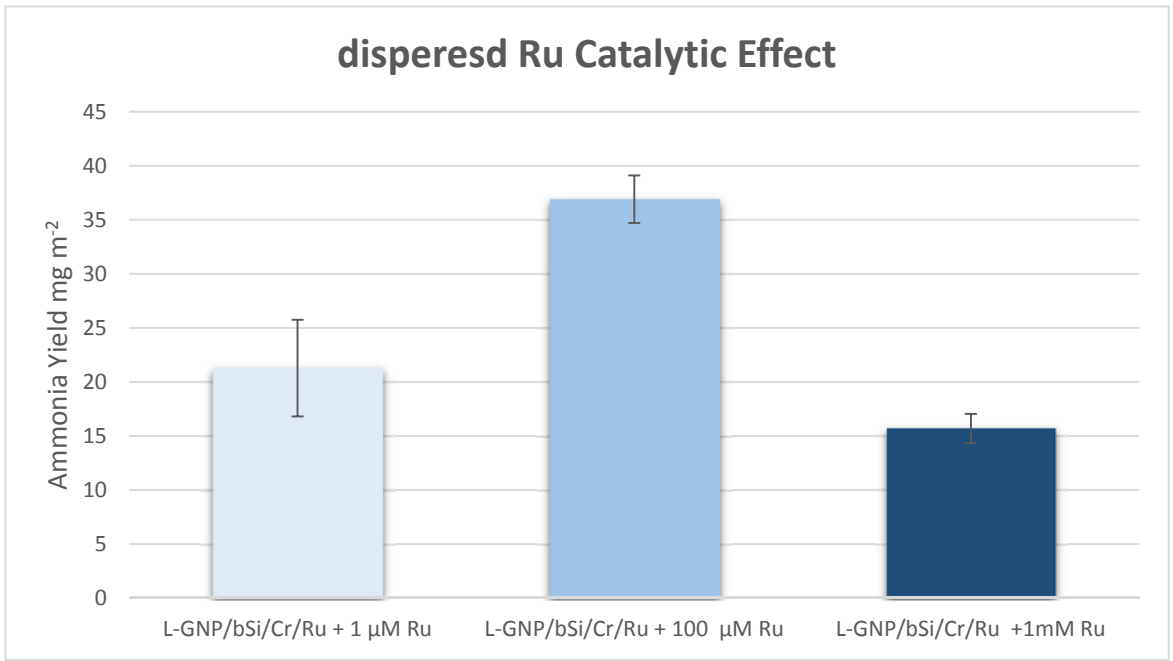

Figure 5-4 B: Ru catalytic effect; GNP/bSi/Cr/Ru: black silicon coated with gold nanoparticles, electroless deposited Ru thin film (3min) with chromium on the back.

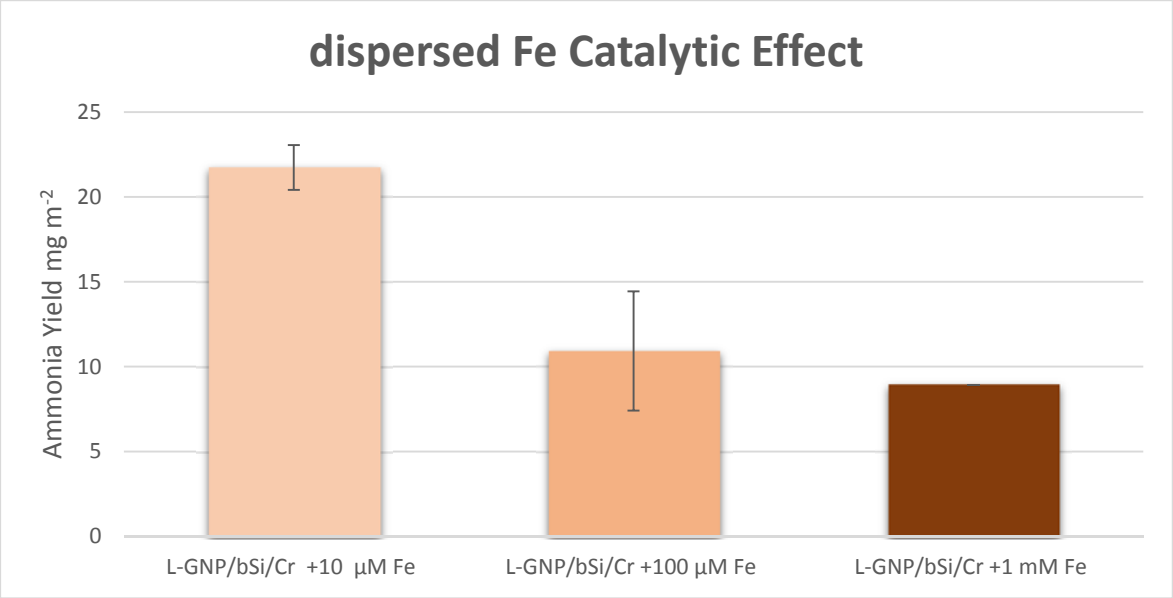

Figure 5-4 C: Fe catalytic effect. The catalytic effect of Fe ions in solution; GNP/bSi/Cr: black silicon coated with gold nanoparticles and chromium on the back. Error bars: standard deviation of at least three repeats.

Combining both Ru catalytic abilities and GNP plasmonic effect in Figure 5-4 B involves both metals in situ in addition to the dissolved Ru ions. The GNP/bSi/Cr prototypes were electroless coated with a thin film of ruthenium for 3 min, and these were used in experiments with varying $RuCl_3$ concentrations (1, 100, 1000µM (figure 5-4 B)). The l lowest electrolyte concentration had a relatively small effect, but 100 µM $RuCl_3$ gave a considerable increase (almost twice) the yield (discussed more extensively in the next section). On the other hand, 1µM $RuCl_3$ results were lower, but this yield converges to the results in 5.2.2; accordingly, the results, in this case, may be regarded to the ineffective amount of the dispersed catalyst and this suggested that the general catalysis is coming from the deposited Ru on to the cell surface.

Comparably, GNP/bSi/Cr tested in an iron-containing electrolyte (10, 100, 1000µM Fe_2O_3) produced notably low yields, which might be regarded to be related to the light blockage by the iron particles, especially at high concentrations. Also, despite the different physical appearance in solution (Ru is dissolved and Fe is dispersed); the weak effect of iron ions compared to that of Ru ions might be understood through volcano plots from the theoretical calculations, explaining the tendency to bind the N_2 atoms to the catalyst surface, which is much better in the case of Ru[14, 43].

This experiment is a direct indication of the catalytic effect of dissolved Ru ions in the NRR experiment. This ability is further studied in the next section of this chapter.

5.3 Dispersed Ru catalysis

5.3.1 separating the catalytic effect of dissolved Ru ions from deposited Ru metal films

Understanding the ability of dispersed Ru ions and separating it from the effect from that of the deposited Ru metal films involved two experiments that were conducted concurrently starting from the same materials (GNP/bSi/Cr, 100µM $RuCl_3$ electrolyte). Samples were taken from the reaction chamber after 3h and 6h and reported in figure 5-5. In experiment 2, after 3h the Ru(III) electrolyte has been replaced with a new DW electrolyte (figure 5-5, light green), while in the first experiment after 3h the Ru(III) electrolyte was kept unchanged (figure 5-5, light blue). Also, a control experiment (GNP/bSi/Cr, DW electrolyte) was conducted.

These results are relatively clear, indicating that a higher yield in the samples kept in the same electrolyte for an extra three hours, these samples reported an average of 23.5 mg m^{-2} in the first three hours and a total of 46.1 mg m^{-2} in six hours. Comparably, the samples with the replacement of the 100µM $RuCl_3$ electrolyte with DW after 3 hours produced 22.4 mg m^{-2} in the first three hours and a combined total of 35.4 mg m^{-2} after six hours.

Results from the first three hours were conconcordant, but diverged in the second three hours after replacing the electrolyte with DW in experiment two. The average three-hour yields in the blue sample were 22.6 mg m^{-2} which was almost the same in the first three hours periods, while the yield in the second experiment was reduced after replacing the

electrolyte with DW to 13.0 mg m^{-2}. This apparent difference indicates the importance of Ru ion as part of the catalysis of the overall NRR process.

Historically, this catalytic effect has been related to the ability of Ru to absorb N_2, decreasing the energy required to break the first bond out of the N_2 three bonds, and promoting a better charge separation. This effect is further discussed in the following sections.

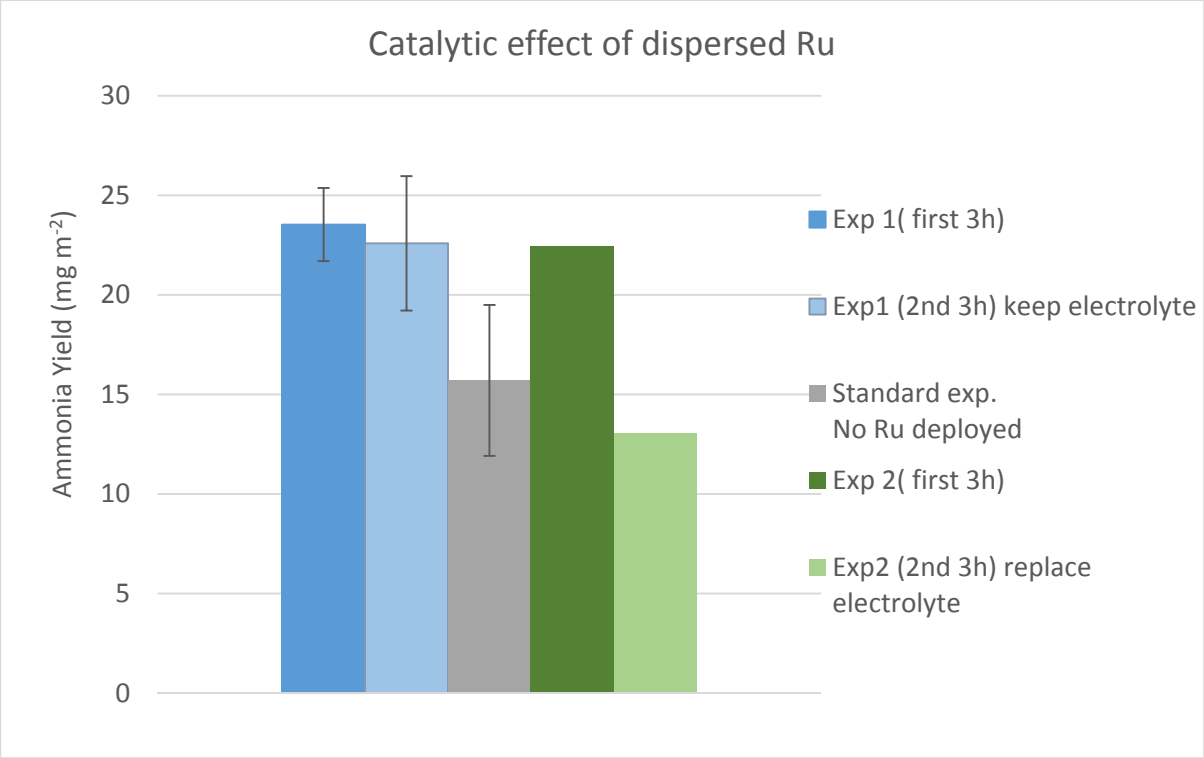

Figure 5-5: Separating the impact of dissolved Ru(III) ions. Experiment one (blue) uses GNP/bSi/Cr and 100µM $RuCl_3$ as an electrolyte for 3h, (blue) and after sampling continues the same experiment with the same electrolyte for a second 3h (light blue). Experiment two (green) uses GNP/bSi/Cr and 100µM $RuCl_3$ as an electrolyte for 3h (green) and after sampling continues the same experiment replacing the electrolyte with DW for a second 3h (light green). Control experiment (grey) GNP/bSi/Cr and DW as the electrolyte. Experimental conditions: 10ml/min flow rate, 2 suns photo-exposure and electrolyte stirring rate 40 rpm. Error bars: standard deviation of at least the repeatings.

5.3.2 understanding the role of Ru ions in the reaction solution

The presence of Ru ions in the reaction chamber produces a noticeably better yield and understanding the source of this requires knowledge of the complexes that can be formed between the Ru ions and the generated ammonia and its derivatives. Historically, there have been many attempts to find which of these complexes are dominant. To mimic what is happening in the reaction solution an experiment was developed, in which a solution of 10 ppm ammonia in a 100µM $RuCl_3$ electrolyte was used in the PCE experiment with GNP/bSi/Cr.

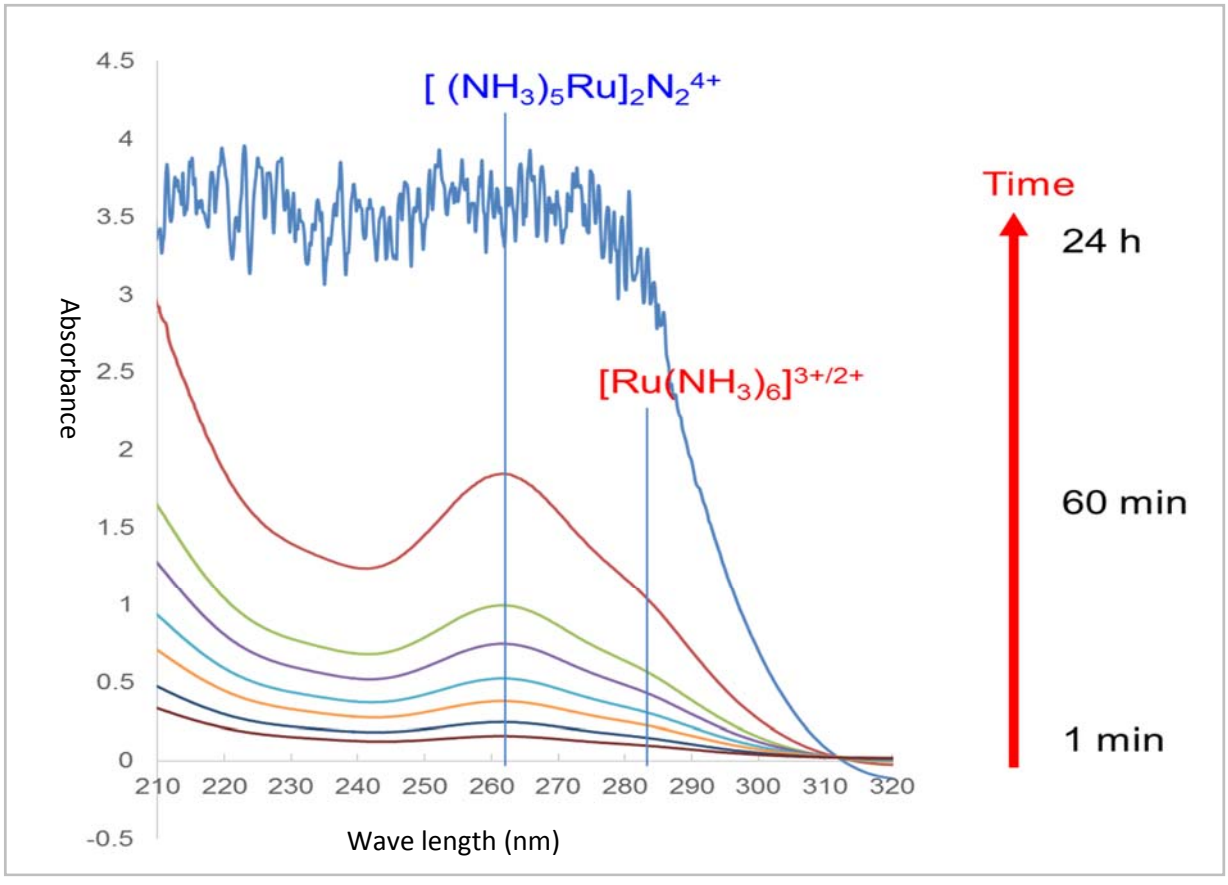

Figure 5-6: UV-vis spectrometric data for different samples during 24h photo-exposure. Peaks at 262 and 284 nm are evidence of the formation of $[Ru(NH_3)_5]_2N_2^{4+}$ and $[Ru(NH_3)_6]^{3+/2+}$, respectively.

Two sun simulator light energy was applied for 24 hours with a stirring rate of 50 rpm. Samples were extracted to be tested by UV-Vis spectroscopy at a different time (figure 5-6). The resultant peaks show the formation in the solution of $[Ru(NH_3)_5]_2N_2^{4+}$ and $[Ru(NH_3)_6]^{3+/2+}$ at 262 and 284 nm respectively.

These observations indicate the to a reduction of Ru^{3+} to Ru^{2+} by the GNP/bSi/Cr structure and the tendency of the Ru(II) ions to absorb NH_3 groups to form both $[Ru(NH_3)_5]_2N_2]^{4+}$ and $[Ru(NH_3)_6]^{3+/2+}$.

The literature reveals the preparation of several complexes containing Ru and NH_3 (figure 5-7). In 1965 Allen and Senoff [44] synthesised $[Ru(NH_3)_5]_2N_2^{4+}$ starting from hydrazine using Zn dust as a reducing agent and by bubbling N_2 through the solution. They were also able to prepare $[(NH_3)_5Ru]_2N_2^{4+}$ and $[Ru(NH_3)_5N_2]^{2+}$ from $(NH_3)_5RuOH_2^{2+}$ [44]. Later they were able to prepare a variety of Ru(II) and Ru(III) ammine complexes by the action of hydrazine hydrate on ruthenium(III) or ruthenium(IV) salts, or by the action of azide ion on aquopentaammineruthenium(III) [45]. Also, Allen and Bottomley reported the formation of $[Ru(NH_3)_5N_2]^{3+}$ after many steps starting from $RuCl_3$ in the presence of HCl and Zn dust[46].

Collectively, all these studies have agreed on the ease of the formation of Ru – ammonia complexes. Studies had also shown the ability of these complexes to fix nitrogen to form $[Ru(NH_3)_5N_2]^{2+}$, which is considered a relatively stable compound [47].

Comparing with the data obtained in 5.3.1, the formation of $[Ru(NH_3)_5N_2]^{2+}$ is rather difficult as the amount of the synthesised ammonia is not sufficient compared to the 100µM Ru^{3+} in the electrolyte in this experiment, but many intermediate $(Ru(NH_3)_x)^{2+}$ species may be formed. These complexes may be catalysing the NRR process by absorbing the generated ammonia

and thereby promoting its equilibrium release from the surface of the catalyst . As a result, the presence of Ru ions increase the reaction yields in 5.3.1, increasing the yield dramatically in figure 5-5 experiment one (blue); but in the second experiment (green), replacing the electrolyte led to the removal of the $Rn(NH_3)_x$ compounds and the yield returned to the control value.

Thus the presence of Ru (II) and (III) ions are usefiul in increasing the efficiency. Also, the compound $[(NH_3)_5Ru]_2N_2^{4+}$, has been prepared simply by the reduction ability of the Si-based prototype, which eliminates the need for Zn dust or any other reducing agents, which is useful in the case electrochemical nitrogen reduction processes.

5.4 References

1. Schlögl, R., *Catalytic Synthesis of Ammonia—A "Never‐Ending Story"?* Angewandte Chemie International Edition, 2003. **42**(18): p. 2004-2008.
2. Ostwald, W., *Grundlinien der anorganischen Chemie*. Vol. 21. 2011: BoD–Books on Demand.
3. Jennings, J.R., *Catalytic ammonia synthesis: fundamentals and practice*. 2013: Springer Science & Business Media.
4. Tamaru, K., *The history of the development of ammonia synthesis*, in *Catalytic ammonia synthesis*. 1991, Springer. p. 1-18.
5. Lindström, B. and L.J. Pettersson, *A brief history of catalysis.* Cattech, 2003. **7**(4): p. 130-138.
6. Perman, E.P., *The direct synthesis of ammonia.* Proceedings of the Royal Society of London. Series A, Containing Papers of a Mathematical and Physical Character, 1905. **76**(508): p. 167-174.
7. Armor, J.N., *A history of industrial catalysis.* Catalysis Today, 2011. **163**(1): p. 3-9.
8. Mittasch, A. and W. Frankenburg, *Early studies of multicomponent catalysts*, in *Advances in catalysis*. 1950, Elsevier. p. 81-104.
9. Vojvodic, A., et al., *Exploring the limits: a low-pressure, low-temperature Haber–Bosch process.* Chemical Physics Letters, 2014. **598**: p. 108-112.

10. Spencer, M., *On the rate-determining step and the role of potassium in the catalytic synthesis of ammonia.* Catalysis letters, 1992. **13**(1-2): p. 45-53.

11. Strongin, D., *The importance of C7 sites and surface roughness in the ammonia synthesis reaction over iron.* 1986.

12. Ertl, G., et al., *Surface characterization of ammonia synthesis catalysts.* Journal of Catalysis, 1983. **79**(2): p. 359-377.

13. Foster, S.L., et al., *Catalysts for nitrogen reduction to ammonia.* Nature Catalysis, 2018. **1**(7): p. 490-500.

14. Ozaki, A., H.S. Taylor, and M. Boudart, *Kinetics and mechanism of the ammonia synthesis.* Proceedings of the Royal Society of London. Series A. Mathematical and Physical Sciences, 1960. **258**(1292): p. 47-62.

15. Aika, K., et al., *Support and promoter effect of ruthenium catalyst: I. Characterization of alkali-promoted ruthenium/alumina catalysts for ammonia synthesis.* Journal of Catalysis, 1985. **92**(2): p. 296-304.

16. Rosowski, F., et al., *Ruthenium catalysts for ammonia synthesis at high pressures: preparation, characterization, and power-law kinetics.* Applied Catalysis A: General, 1997. **151**(2): p. 443-460.

17. Bossi, A., et al., *Support effects on the catalytic activity and selectivity of ruthenium in CO and N 2 activation.* Journal of the Chemical Society, Faraday Transactions 1: Physical Chemistry in Condensed Phases, 1982. **78**(4): p. 1029-1038.

18. Fastrup, B., *On the interaction of N 2 and H 2 with Ru catalyst surfaces.* Catalysis letters, 1997. **48**(1-2): p. 111-119.

19. Szmigiel, D., et al., *The kinetics of ammonia synthesis over ruthenium-based catalysts: The role of barium and cesium.* Journal of Catalysis, 2002. **205**(1): p. 205-212.

20. Brown, D.E., et al., *The genesis and development of the commercial BP doubly promoted catalyst for ammonia synthesis.* Catalysis letters, 2014. **144**(4): p. 545-552.

21. Jacobsen, C.J., *Boron nitride: a novel support for ruthenium-based ammonia synthesis catalysts.* Journal of Catalysis, 2001. **200**(1): p. 1-3.

22. Yang, X.-L., et al., *Low temperature ruthenium catalyst for ammonia synthesis supported on BaCeO3 nanocrystals.* Catalysis Communications, 2010. **11**(10): p. 867-870.

23. Saito, M., et al., *Synergistic effect of MgO and CeO 2 as a support for ruthenium catalysts in ammonia synthesis.* Catalysis letters, 2006. **106**(3-4): p. 107-110.

24. Niwa, Y. and K.-i. Aika, *The effect of lanthanide oxides as a support for ruthenium catalysts in ammonia synthesis.* Journal of Catalysis, 1996. **162**(1).

25. Liang, C., et al., *Graphitic nanofilaments as novel support of Ru–Ba catalysts for ammonia synthesis.* Journal of Catalysis, 2002. **211**(1): p. 278-282.

26. Hara, M., M. Kitano, and H. Hosono, *Ru-loaded C12A7: e–electride as a catalyst for ammonia synthesis.* ACS Catalysis, 2017. **7**(4): p. 2313-2324.

27. Guo, C., et al., *Rational design of electrocatalysts and photo(electro)catalysts for nitrogen reduction to ammonia (NH3) under ambient conditions.* Energy & Environmental Science, 2018. **11**(1): p. 45-56.

28. Skúlason, E., et al., *A theoretical evaluation of possible transition metal electro-catalysts for N2 reduction.* Physical Chemistry Chemical Physics, 2012. **14**(3): p. 1235-1245.

29. Montoya, J.H., et al., *The Challenge of Electrochemical Ammonia Synthesis: A New Perspective on the Role of Nitrogen Scaling Relations.* ChemSusChem, 2015. **8**(13): p. 2180-2186.

30. Wang, D., et al., *Energy-Efficient Nitrogen Reduction to Ammonia at Low Overpotential in Aqueous Electrolyte under Ambient Conditions.* ChemSusChem, 2018. **11**(19): p. 3416-3422.

31. Kordali, V., G. Kyriacou, and C. Lambrou, *Electrochemical synthesis of ammonia at atmospheric pressure and low temperature in a solid polymer electrolyte cell.* Chemical Communications, 2000(17): p. 1673-1674.

32. Ogawa, T., et al., *High Electron Density on Ru in Intermetallic YRu2: The Application to Catalyst for Ammonia Synthesis.* The Journal of Physical Chemistry C, 2018. **122**(19): p. 10468-10475.

33. Imamura, K. and J. Kubota, *Ammonia synthesis from nitrogen and water at intermediate temperatures and elevated pressures by using an electrochemical hydrogen-membrane reactor with supported Ru catalysts and phosphate electrolytes.* Sustainable Energy & Fuels, 2019.

34. Manjunatha, R. and A. Schechter, *Electrochemical synthesis of ammonia using ruthenium–platinum alloy at ambient pressure and low temperature.* Electrochemistry Communications, 2018. **90**: p. 96-100.

35. Zhou, F., et al., *Electro-synthesis of ammonia from nitrogen at ambient temperature and pressure in ionic liquids.* Energy & Environmental Science, 2017. **10**(12): p. 2516-2520.

36. Kugler, K., et al., *Galvanic deposition of Rh and Ru on randomly structured Ti felts for the electrochemical NH3 synthesis.* Physical Chemistry Chemical Physics, 2015. **17**(5): p. 3768-3782.

37. Bao, D., et al., *Electrochemical Reduction of N2 under Ambient Conditions for Artificial N2 Fixation and Renewable Energy Storage Using N2/NH3 Cycle.* Advanced Materials, 2017. **29**(3): p. 1604799.

38. Lan, R., J.T. Irvine, and S. Tao, *Synthesis of ammonia directly from air and water at ambient temperature and pressure.* Scientific reports, 2013. **3**.

39. Liu, S., et al., *Photocatalytic Fixation of Nitrogen to Ammonia by Single Ru Atom Decorated TiO2 Nanosheets.* ACS Sustainable Chemistry & Engineering, 2019. **7**(7): p. 6813-6820.

40. Chen, J.-Y., et al., *Electroless deposition of Ru films on Si substrates with surface pretreatments.* Thin Solid Films, 2013. **529**: p. 426-429.

41. McCulloch, I., et al., *Liquid-crystalline semiconducting polymers with high charge-carrier mobility.* Nature Materials, 2006. **5**(4): p. 328-333.

42. Chen, J.-Y., L.-Y. Wang, and P.-W. Wu, *Preparation and characterization of ruthenium films via an electroless deposition route.* Thin Solid Films, 2010. **518**(24): p. 7245-7248.

43. Medford, A.J., et al., *From the Sabatier principle to a predictive theory of transition-metal heterogeneous catalysis.* Journal of catalysis, 2015. **328**: p. 36-42.

44. Allen, A. and C. Senoff, *Nitrogenopentammineruthenium (II) complexes.* Chemical Communications (London), 1965(24): p. 621-622.

45. Allen, A.D., et al., *Ruthenium complexes containing molecular nitrogen.* Journal of the American Chemical Society, 1967. **89**(22): p. 5595-5599.

46. Allen, A.D. and F. Bottomley, *Inorganic nitrogen fixation. Nitrogen compounds of the transition metals.* Accounts of Chemical Research, 1968. **1**(12): p. 360-365.

47. Allen, A. and F. Bottomley, *Fixation of atmospheric nitrogen by ruthenium compounds.* Canadian Journal of Chemistry, 1968. **46**(3): p. 469-469.

Chapter Six

conclusions and future work

6.1 Conclusions

This study has been designed to tackle a significant contributor to global warming, which is one of the main issues facing humanity in the 21 century. Ammonia production consumes a considerable part of the world's energy and emits a substantial amount of carbon dioxide into the environment. However, ammonia production is an indispensable process because of its role in food production.

The objectives of this thesis involved developing the silicon wafer to absorb light efficiently and improving it to be able to reduce molecular nitrogen and later optimising the working prototype in order to generate relatively higher efficiencies. These objectives have been achieved with further development of the concept by introducing a catalyst, which significantly increases the prototype overall efficiency.

Light absorption efficiency was achieved by dry-etching Si to form b-Si, and this was further developed by decorating the b-Si surface with GNP, which add the plasmonic effect to the cell. The boosted light absorption efficiency abilities were tested by designing a dye degradation experiment, in which the b-Si was shown to be better than flat Si, and the bSi+GNP offered a further improvement in the overall degradation process.

In chapter three, the prototype was further developed by introducing Cr(III) plated on its back; the cell now works as a two-electrode device. The results in this part of the work were remarkable; 320 mg m^{-2} yield was achieved in 24h experiments, and these were rather stable and has not affected with product build up. Light intensity was studied to find the limiting yield which found to be 2 Sun. Nitrogen diffusion rates effect were also tested in a

specially designed equipment to allow an increase in N_2 pressure; the results show a linear increase in cell production rate up to 6 bar. Quantum efficiency of ammonia synthesis on a GNP/bSi/Cr photoelectrochemical cell as a function of wavelength has been calculated, showing a notable increase around 500nm, indicating the effect of the plasmonic resonance.

To optimise further the working prototype a 75 L incubator was constructed, in order to minimise external environmental influences. A Variety of Si wafers with different thicknesses and conductivities were tested, showing a wafer with 500µm thickness and 1-10 ohm cm^{-1} resistivity to give comparably the highest yields. Optimal gold coating thickness was found to be 180s, while pH testing in both buffers modified electrolyte or simple HCl/NaOH electrolyte resulted in better efficiencies in neutral/ slightly acidic media. Temperature variations show better efficiencies toward lower temperatures and more ammonia loss due to evaporation at higher temperature ranges.

Boosting the yield toward new levels requires the use of an appropriate catalyst, two catalysts have been introduced; Fe (III) and Ru(III). Three methods were used to attach Ru (III) to the semiconductor surface; drop-casting, electroless deposition and in solution dispersion. The results showed a considerable ability of Ru in catalysing the NRR. This ability of Ru was further investigated and proven to be the ability of this metal to form complexes with the generated ammonia, which absorbs it from the catalytic sites on the semiconductor surface.

6.2 future work

Suggested future work would include:

1. Replicate the work with different types of semiconductors such as CdSe, CdTe and CdS.
2. Electrochemically add energy (voltage) to the working prototype to further boost the production rate. This process will depend on the sunlight to provide energy, but at the same time can use an extra source of energy.
3. Further optimisation using different sorts of wafers (that were not available to us while conducting this work), in addition to experimenting with n-type silicon.
4. Experminting with more catalysts for the NRR, such as Re, Rh, Mo, Ir, Pt, Cu, and Ag, and consequently experimenting with new metal deposition methods.
5. Introduce Ag instead of Au to enable plasmonic effect.